

UNIVERSITEIT VAN AMSTERDAM



VRIJE UNIVERSITEIT AMSTERDAM

Towards a moving optical lattice for trapping ultracold strontium atoms inside a ring cavity

L.M. Michels

July 17, 2026

MSc Physics & Astronomy (joint degree)
Advanced Matter and Energy Physics

Master Thesis

Student number: 13269011

Institute of Physics, Van der Waals-Zeeman Institute

Daily supervisor: Benedikt Heizenreder

Supervisor: prof. dr. F.E. Schreck

Second examiner: dr. R. Gerritsma

Contents

Abstract **3**

Nederlandse samenvatting **4**

1 Introduction **5**
1.1 Optical atomic clocks . . . 5
1.1.1 The superradiant optical clock experiment . . . 6
1.2 Thesis overview . . . 8

2 Theoretical background **10**
2.1 Strontium . . . 11
2.1.1 Energy-level structure . . . 11
2.1.2 Atomic polarizability & Optical dipole traps . . . 12
2.2 Optical resonators . . . 14
2.2.1 Fabry-Pérot cavity . . . 15
2.2.2 TEM-modes . . . 17
2.2.3 Bowtie cavity . . . 18
2.3 Pound-Drever-Hall technique . . . 21

3 Laser systems **25**
3.1 The 689 nm laser system . . . 26
3.1.1 689 nm shifting setup . . . 26
3.2 The 813 nm laser system . . . 26
3.2.1 813 nm shifting setup . . . 27

4 Injection lock 813 nm laser **31**
4.1 Building 813 nm injection lock . . . 32
4.2 Beat note . . . 34
4.3 Long term frequency stability . . . 35

5 Building the mock system **37**
5.1 Bowtie cavity construction . . . 38
5.1.1 Piezoelectric actuators . . . 39
5.2 Vacuum chamber . . . 40
5.3 Optical setup . . . 42
5.4 Pound-Drever-Hall lock . . . 44
5.5 Mock cavity characterization . . . 48

6 The mHz-machine **52**
6.1 Science chamber cavity lock . . . 53
6.1.1 Short-term stability . . . 53
6.1.2 Long-term stability . . . 54
6.2 Science chamber cavity characterization . . . 56
6.2.1 Ring-down measurement . . . 56
6.2.2 Non-degenerate polarization eigenmodes . . . 57
6.3 Predictive calculations . . . 57
6.3.1 Optical lattice . . . 59
6.3.2 Rabi oscillations $^1S_0 \rightarrow {}^3P_1$ transition . . . 61

7 Conclusion & Outlook **64**

Acknowledgments **66**

References **67**

Abstract

In recent years, optical atomic clocks have emerged as state-of-the-art timekeeping devices, promising future improvements in metrology and offering a possible replacement for microwave standards in redefining the SI second. The $^1S_0 \rightarrow {}^3P_0$ transition in strontium is commonly used as a stable frequency reference for optical lattice clocks, due to its ultra-narrow mHz linewidth. This thesis reports on the development of a moving optical lattice for continuous readout of this clock frequency. The optical lattice consists of two counter propagating 813 nm 'magic'-wavelength laser beams, inside a bowtie ring cavity. An induced frequency shift between the two beams, allows the pumping and emission zones inside the cavity to be continuously replenished with new, ultracold strontium atoms.

To increase the available optical power of the lattice light, an injection lock was built that boosts the power of the 813 nm parent laser from roughly 1 mW to a few tens of mW. This increase in power enables a deeper trap depth to be achieved for atoms inside the optical lattice.

An optical setup consisting of two lattice beams and a probe beam, initially targeting the 689 nm $^1S_0 \rightarrow {}^3P_1$ transition, is built on a compact breadboard mounted above the vertically oriented bowtie cavity. The beams were first aligned on a separate 'mock' system, which provided more working space than on the main experiment. A second bowtie cavity was assembled and tested for this purpose. The breadboard was then transferred to the experiment's science chamber, where the beams were realigned to the experiment's bowtie cavity. To establish an optical lattice between the cavity mirrors, a Pound-Drever-Hall (PDH) lock was implemented, locking the bowtie cavity to the 813 nm light. This lock stabilized the cavity length to a frequency stability of 70 kHz. Additionally, a frequency shifting setup was implemented to bring the cavity into simultaneous resonance with the 813 nm and 689 nm light. This was achieved by shifting the frequency of the lattice light, and consequently the length of the locked cavity, so that the longitudinal modes of both wavelengths could be made to overlap.

Ring-down measurements were performed to characterize the bowtie cavity, resulting in a measured finesse of 5870 for the 689 nm light and 3120 for the 813 nm light. The measured cavity linewidth was found to be 250 kHz for the 689 nm light, indicating that the achieved lock stability falls within the upper limit required for superradiant lasing in the bad-cavity regime.

Based on the measured cavity parameters, predictive calculations were performed to estimate the achievable trap depth of the optical lattice for different lattice velocities. The probe power and pulse lengths required to induce Rabi oscillations in the atoms were also calculated.

Nederlandse samenvatting

In de afgelopen jaren hebben optische atoomklokken zich bewezen als 'state-of-the-art' tijdmeetapparaten, die toekomstige verbeteringen in de metrologie beloven en een mogelijke vervanging bieden voor microgolfstandaarden bij het herdefiniëren van de SI-seconde. De $^1S_0 \rightarrow {}^3P_0$ overgang in strontium wordt, vanwege zijn ultrasmalle mHz-lijnbreedte, veelvuldig gebruikt als een stabiele frequentiereferentie voor optische roosterklokken. Deze scriptie beschrijft de ontwikkeling van een bewegend optisch rooster voor continue uitlezing van deze klokfrequentie. Het optische rooster bestaat uit twee tegengesteld propagerende 813 nm 'magische'-golflengte laserbundels in een 'bowtie'-ringresonator. Een geïnduceerde frequentieverschuiving tussen de twee bundels, zorgt ervoor dat de pomp en emissie zones in de optische resonator continu wordt aangevuld met nieuwe, ultrakoude strontiumatomen.

Om het beschikbare optische vermogen van het roosterlicht te vergroten, is een injectielock gebouwd die het vermogen van de 813 nm laser verhoogt van ongeveer 1 mW naar enkele tientallen mW. Deze vermogenstoename maakt het mogelijk om een grotere valdiepte voor atomen in het optische rooster te bereiken.

Een opstelling bestaande uit twee roosterbundels en een probebundel, aanvankelijk gericht op de 689 nm $^1S_0 \rightarrow {}^3P_1$ overgang, is opgebouwd op een compact breadboard dat boven de verticaal georiënteerde bowtie-resonator is gemonteerd. De bundels werden eerst uitgelijnd op een apart 'mock'-systeem, dat meer werkruimte bood dan het hoofdexperiment. Voor dit doel werd een tweede bowtie-resonator gebouwd en getest. Daarna werd het breadboard overgebracht naar de vacuumkamer van het experiment, waar de bundels opnieuw werden uitgelijnd op de bowtie-resonator aldaar. Om een optisch rooster tussen de resonatorspiegels tot stand te brengen, werd een Pound-Drever-Hall (PDH) lock geïmplementeerd, die de bowtie-resonator vergrendelde op de frequentie van het 813 nm licht. Deze lock stabiliseerde de lengte van de resonator tot een frequentiestabiliteit van 70 kHz. Daarnaast werd een frequentieverschuivingsopstelling geïmplementeerd om de resonator gelijktijdig in resonantie te brengen met het 813 nm en 689 nm licht. Dit werd bereikt door de frequentie van het roosterlicht, en daarmee de lengte van de vergrendelde resonator, zodanig te verschuiven dat de longitudinale modi van beide golflengtes konden worden overlapt.

'Ring-down' metingen werden uitgevoerd om de bowtie-resonator te karakteriseren, wat resulteerde in een gemeten 'finesse' van 5870 voor het 689 nm licht en 3120 voor het 813 nm licht. De gemeten lijnbreedte van de resonator bleek 250 kHz te zijn voor het 689 nm licht, wat aantoont dat de behaalde lockstabiliteit binnen de bovengrens valt die vereist is voor 'superradiant lasing' in het 'bad-cavity' regime.

Op basis van de gemeten parameters van de resonator, zijn voorspellende berekeningen uitgevoerd om de haalbare valdiepte van het optische rooster te benaderen voor verschillende roostersnelheden. Ook zijn het benodigde probevermogen en de pulslengtes berekend die nodig zijn om Rabi-oscillaties in de atomen te induceren.

Chapter 1

Introduction

1.1 Optical atomic clocks

In recent years, ultracold atoms have emerged as a powerful platform for the development of quantum technologies [1]. Following the realization of the first Bose-Einstein condensates (BEC) in alkali atoms in 1995, condensation of alkaline-earth atoms was achieved shortly after [2, 3]. Their two valence electrons give alkaline-earth atoms a useful energy level structure, combining broad transitions that are well-suited for efficient laser cooling, together with narrow intercombination lines that enable cooling to sub-microkelvin temperatures. Furthermore, the presence of singlet and triplet manifolds gives rise to strongly spin-forbidden transitions, that can be used for the development of most precise optical clocks [4].

These clocks exploit ultra-narrow optical transitions as high-precision frequency references. In contrast to conventional atomic clocks, which are based on microwave transitions ($\sim$GHz), the much higher frequency (hundreds of THz) and narrower linewidth of these optical transitions, result in clocks with a higher quality factor $Q = \frac{\nu_0}{\Delta\nu}$. Moreover, for a given interrogation time, optical clocks require less averaging time to reach uncertainties comparable to those of established microwave clocks [5]. State-of-the-art optical clocks have shown to reach fractional frequency uncertainties as low as $10^{-18} - 10^{-19}$ [6]. This level of accuracy opens the door to applications such as improved GPS navigation, high-speed network synchronization and quantum sensing, for instance in relativistic gravitational measurements [7].

Most optical clocks operate by referencing a laser to a narrow atomic transition, which provides excellent long-term frequency stability. To achieve good short-term stability as well, the laser is typically pre-stabilized to an optical cavity. In this cavity, resonant light builds up between two (or more) highly reflective mirrors. The higher the reflectivity of these mirrors, the larger the cavity's finesse, resulting in a narrower resonance linewidth and greater short-term frequency stability. Locking a laser to this cavity therefore narrows its linewidth, effectively transferring the cavity's short-term stability onto the laser. The stability of today's best cavities is limited by Brownian noise in the mirror coatings, but this field is still under exploration. For most cavities, the length, and thus its resonance frequency, slowly drifts over time (due to material aging and temperature fluctuations) this drift is compensated by periodically interrogating an ultracold atomic ensemble that is trapped using an optical lattice. This slowly steers the laser's center frequency, to remain resonant with the probed atomic transition. Because the transition frequency lies in the optical domain, it is practically impossible to directly measure the laser's frequency fluctuations electronically, since no photodetector or RF electronics can follow oscillations at hundreds of THz. For this reason, a frequency comb is used. This is a mode-locked pulsed laser, where the repetition frequency of the pulses sets the spacing between the comb's teeth, resulting in a comb structure that acts as an optical ruler. By generating a beat note between the locked, stabilized laser and the nearest comb tooth, an electronically detectable RF signal is created. With this RF signal, it becomes possible to resolve the laser's frequency fluctuations with Hz-level resolution, using standard RF electronics. The schematic overview of a typical optical lattice clock experiment is presented in Fig. 1.1.

There are two main factors that limit the stability and accuracy of these experiments. The first one is the so called 'dead time' between atom interrogations. After exciting the atoms on the clock transition, the ground- (or excited-) state population is read out via a separate transition. This readout process destroys the atomic ensemble, since the atoms are lost or heated out of the trap, meaning a new ensemble must be cooled down and prepared before the next measurement can begin. During this preparation time, no clock frequency can be recorded. This limits the fraction of the total experimental cycle spent on probing the atomic clock transition. Because of this periodic sampling of the clock signal, high frequency noise in the laser is aliased to low frequency noise in the measured clock signal, also known as the Dick effect [8]. Dead time therefore imposes a fundamental limit on the maximum achievable frequency stability of standard optical clocks. The second limiting factor relates to the optical cavity used for short-term stabilization of the laser. Any disturbance in the cavity length, caused

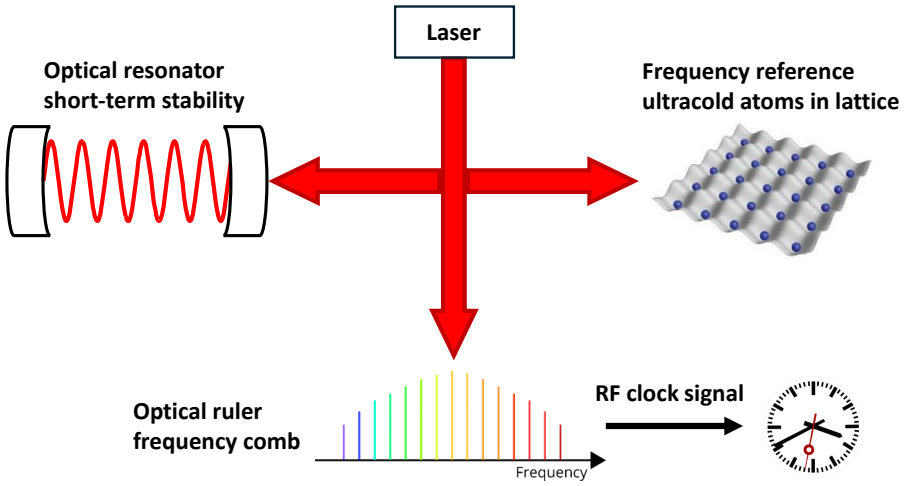


Figure 1.1: Simplified schematic overview of a typical optical lattice clock experiment. The clock laser is pre-stabilized to an optical cavity that provides short-term stability and narrows the linewidth of the laser. An ultracold atomic ensemble is used as an absolute frequency reference to keep the laser's center frequency on resonance with the clock transition. The locked and stabilized laser frequency is compared to a mode of a frequency comb, which acts as an optical ruler. This transfers the frequency stability to an RF signal, which can be used to transmit the clock signal over large distances.

by temperature fluctuations or vibrations, is directly imprinted onto the laser frequency and thus onto the clock signal. This effect can be mitigated by using an ultra-low-expansion (ULE) cavity that is thermally and mechanically isolated from its environment.

The dead time problem can be solved either by continuously cooling and repumping the atoms, or by actively transporting atoms through the system. In continuous operation, the frequency uncertainty of zero-dead-time optical clocks would scale with the averaging time as $1/\tau$, compared to the $1/\sqrt{\tau}$ scaling for clocks with dead time [9]. For the latter approach, atoms are cooled down, prepared and probed at different positions inside the experiment. In the superradiant optical clock experiment, where this master's project was carried out, such an 'active' optical clock is being developed. As will become clear in the next section, the technique used in this experiment also removes the need for an ultra-stable cavity to stabilize the clock laser's frequency.

1.1.1 The superradiant optical clock experiment

The optical clock that is being developed in this experiment, uses ultracold strontium atoms as the platform for a new type of optical clock. It utilizes the ${}^1S_0 \rightarrow {}^3P_0$ transition in strontium, which has an ultra-narrow linewidth of $\Gamma = 2\pi \times 1.35\,\mathrm{mHz}$, in the ${}^{87}\mathrm{Sr}$ isotope [10]. Throughout the rest of this thesis, the experiment is therefore also referred to as the 'mHz-experiment' or 'mHz-machine.'

To accurately measure the frequency of the mHz-wide transition, the strontium atoms must first be cooled down to μK temperatures. This suppresses Doppler broadening of the transition and makes it possible to trap the atoms efficiently in an optical lattice, placing them in the Lamb-Dicke regime [11]. Cooling takes place in several stages: the atoms are first decelerated via Zeeman slowing and captured in a 2D blue magneto-optical trap (MOT), reaching temperatures on the order of a few mK. From there, the atoms fall down into a 3D red MOT operating on the narrow intercombination line, which further cools down the ensemble to sub-μK temperatures [12].

In order to eliminate the need for an ultra-stable cavity to stabilize the laser frequency, we instead use the radiation emitted by the atoms themselves directly as an ultra-stable frequency

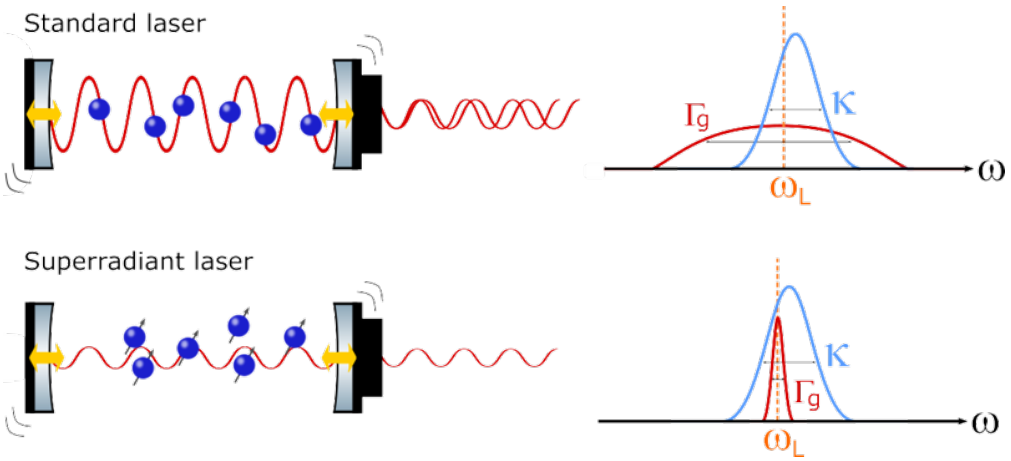


Figure 1.2: Comparison between a standard laser in the 'good-cavity' regime and a superradiant laser in the 'bad-cavity' regime. For a standard laser the linewidth of the gain medium Γ_g is much broader than the cavity linewidth κ, in contrast to a superradiant laser were $\kappa >> \Gamma_g$. In a superradiant laser, the output frequency is mainly determined by the atomic ensemble, from [14].

source. Placing the atomic ensemble inside a cavity, allows the atoms to act as a laser gain medium with an ultra-narrow linewidth. The presence of the cavity also enhances the collective emission of light by the atoms, as the cavity field mutually synchronizes the radiating dipoles. As a result, the phase coherence of the lasing light is stored in the atoms rather than in the cavity field, producing a laser with both enhanced emission power and high phase coherence. Lasers of this type are known as *superradiant* lasers [13]. Their gain linewidth is significantly narrower than the cavity linewidth, placing them deep in the so-called 'bad-cavity' regime. This is in contrast to conventional lasers, which operate in the 'good-cavity' regime, where the gain linewidth is much broader than the cavity linewidth (see Fig. 1.2).

In a conventional laser, the frequency stability of the output is set by the stability of the cavity length. Fluctuations in cavity length, caused by thermal fluctuations or vibrations, are directly imprinted onto the laser's output frequency. In a superradiant laser, by contrast, the frequency stability is instead set by the atomic transition. As a result, frequency fluctuations arising from changes in cavity length are strongly suppressed, yielding a stable output frequency suitable for use as an optical clock. The residual sensitivity to cavity length fluctuations is quantified by the so-called cavity pulling factor [15]

$$P = \frac{\Gamma}{\Gamma + \kappa}, \tag{1.1}$$

where Γ is the linewidth of the gain medium and κ is the linewidth of the cavity. This pulling factor quantifies the degree to which the laser's output frequency is shifted toward the cavity resonance, when the cavity is detuned from the atomic resonance.

As mentioned in the previous section, the atoms will be actively transported through the system, with the goal of obtaining a continuous clock signal. This is achieved by continuously outcoupling ultracold atoms from the red MOT into a dipole guide, while maintaining μK temperatures. The dipole guide transports the atoms from the MOT chamber to the science chamber, which houses a ring cavity in a 'bowtie' configuration. Inside this bowtie cavity, an optical lattice is formed using two counter-propagating laser beams that are red-detuned from the clock transition in strontium. Atoms are trapped at the anti-nodes of this lattice, which acts as a one-dimensional dipole trap. By inducing a relative frequency shift between the two lattice beams, the lattice can be made to move along the cavity axis, acting as a 'conveyor belt' that transports the atoms through the cavity [16]. The main focus of this thesis is the development of this moving optical lattice inside the bowtie cavity. A schematic overview of the mHz-experiment is given in Fig. 1.3.

For this experiment, the linewidth of the gain medium is the $\Gamma = 2\pi \times 1.35\,\text{mHz}$ wide clock transition in strontium and the expected bowtie cavity linewidth is $\kappa \approx 2\pi \times 200\,\text{kHz}$, based on

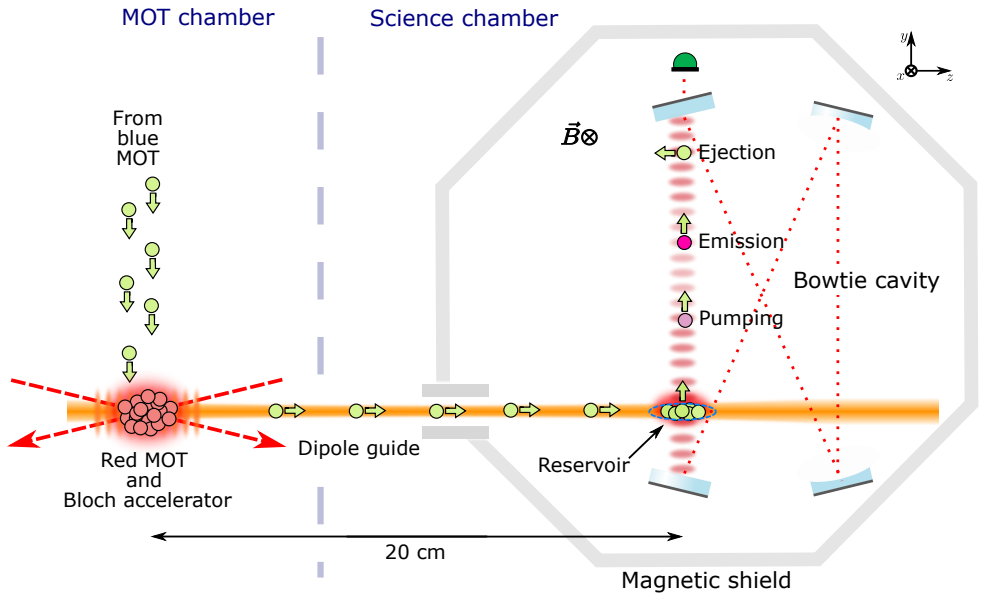


Figure 1.3: Schematic overview of the mHz-machine in the superradiant optical clock experiment. A continuous output of the clock signal is realized by continuous cooling, loading and trapping of ultracold strontium atoms. The atoms are interrogated on the clock transition while trapped inside a moving optical lattice, from [16].

measurements reported in [17]. For these values, the pulling factor is $P \approx 6.75 \times 10^{-9} << 1$, indicating a strongly suppressed cavity pulling effect. This means that the cavity length does not need to be stabilized to a frequency stability of 1.35 mHz. Instead, the upper limit on the required stability is set by

$$\Delta f_{lock} < \frac{\Gamma}{P} \approx \kappa. \tag{1.2}$$

In other words, the cavity length needs to be locked to a frequency stability Δf_{lock} that is smaller than the cavity's own linewidth κ. Where the goal would be to reach a stability that is ideally an order of magnitude smaller. In Sec. 6.1.1 of this thesis, it is described how such a cavity lock is realized and what lock stability is achieved for the bowtie cavity.

1.2 Thesis overview

This thesis describes in detail the design and construction of the moving optical lattice inside the bowtie cavity. In the early stage of the experiment, the primary goal is to measure atom–cavity coupling and to initially probe atoms on the $^1S_0 \rightarrow {}^3P_1$ transition. Its broader linewidth of 7.4 kHz, compared to the ultra-narrow mHz-wide clock transition, makes this transition easier to probe. Accordingly, the implementation of a probe beam targeting this transition is also described here.

Initially, a theoretical background is presented that covers the relevant atomic properties of strontium, the working principles of (ring) cavities and the theory behind 'Pound-Drever-Hall' locking. This is followed by an overview of the laser systems used for the optical lattice and probe beam. Since the available optical power for the lattice light proved insufficient for reaching the required trap depths, an injection lock setup was built to increase the lattice light power while maintaining the frequency stability of the parent laser.

The limited space around the experiment's science chamber made it difficult to build and align the optical setup, used to couple the lattice and probe beams into the bowtie cavity. To solve this problem, a 'mock' system was built that mimics the dimensions of the science chamber

using a copy of the bowtie cavity. This allows the optical setup for the cavity beams to be built and aligned on a separate table with more working space. This thesis describes the construction of this mock system, including a vacuum chamber and the assembly of the second bowtie cavity.

An overview is given of the optical setup, consisting of two lattice beams and a probe beam. All cavity transmissions are also monitored in this optical setup. Additionally, locking of the bowtie cavity to the lattice light, using the Pound-Drever-Hall method, is described.

Finally, the optical setup was moved from the mock system and placed on the science chamber of the mHz-machine, where the experiment's bowtie cavity was again locked to the lattice light. Two different locking schemes were used to obtain a short-term and a long-term stable lock, where the limiting factors of both are reported. Using the short-term stable lock, the experiment's bowtie cavity was characterized with a ring-down measurement and its measured linewidth and finesse are reported. Based on these measured characteristics, the performance of the cavity is quantified through predictive calculations of the obtainable optical lattice trap depth and probe beam requirements for inducing Rabi oscillations in the atoms.

Chapter 2

Theoretical background

As described in Sec. 1.1.1, different stages of the experiment require different lasers for cooling and interrogation of the atoms. In this chapter, I will start with an overview of the energy level structure of strontium, pointing out the most important transitions needed for this experiment. After that I will explain how lasers can also be used to trap and transport strontium atoms once they are cooled down.

In this work, the trapping and transportation of atoms happens inside an optical ring resonator. The second section will therefore give a theoretical explanation on the working principles of optical resonators. A simple linear cavity is used as an example to derive some of the important equations describing optical cavities and the spatial profile of electromagnetic fields inside cavities is shortly mentioned. After that, the main differences between linear and ring cavities is described using the specific example of a 'bowtie' cavity, which is used in this experiment.

In order to stabilize the cavity length to the frequency of the incoming light, we make use of the 'Pound-Drever-Hall' (PDH) technique. This is a common mechanism for locking an optical cavity to a laser (or vice versa). In the last section, an overview of the PDH-technique is presented where I derive an expression for the 'error signal' used to lock the cavity to a laser frequency.

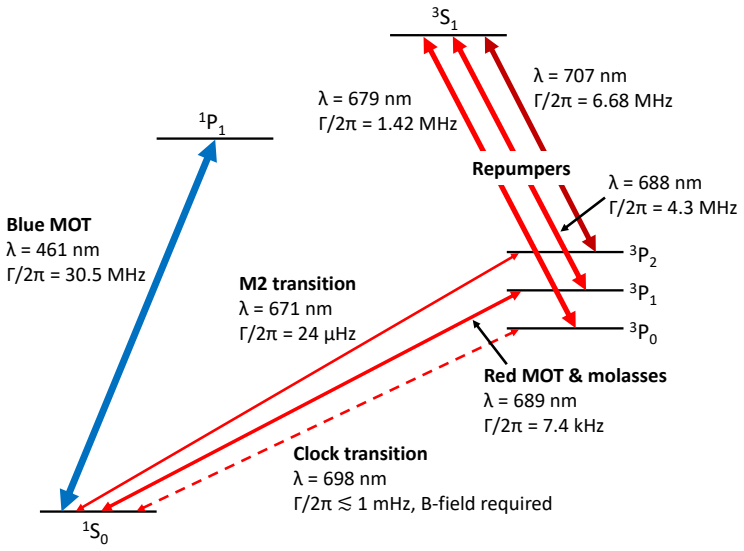


Figure 2.1: Energy level structure of ^{88}Sr relevant for cooling, magneto-optical trapping and optical clock operation. Here, $\Gamma/2\pi = \gamma$ is the natural linewidth of the transition [19–21].

2.1 Strontium

Neutral strontium is a widely used element in the field of optical clocks and quantum computing [5, 18]. The electronic energy levels in strontium are easily accessible with optical wavelength lasers and its two valance electrons create two separate energy manifolds, the singlet and triplet states. The singlet-to-singlet transitions do not require the spin of one valence electron to flip, resulting in a broad dipole allowed transition according to the selection rules of quantum mechanics. The singlet-to-triplet transitions however, do require the spin of one valence electron to flip. These transitions are therefore spin forbidden ($\Delta S \neq 0$), which makes them only weakly allowed via spin-orbit coupling, resulting in a narrower linewidth. This combination of broad and narrow transitions can be used for laser cooling and trapping with blue and red magneto-optical traps (MOT) and the existence of an ultra-narrow, doubly forbidden, optical transition is commonly used as a clock transition or an optical qubit [19].

In this section I will give an overview of the energy level structure of ^{88}Sr, pointing out the relevant electronic transitions and their properties used for cooling and interrogation. After that, I will give a short but comprehensive explanation about the principles of optical dipole traps based on the picture of atomic polarizability. In addition I will show the existence of *magic* wavelengths which are relevant for creating stable optical lattices.

2.1.1 Energy-level structure

The electronic energy level structure of ^{88}Sr is shown in Fig. 2.1. This level scheme shows the most relevant transitions in the context of laser cooling, optical clock operation and trapping with magneto-optical traps (MOT). This is a common technique for cooling and trapping atoms using a combination of laser beams and magnetic fields. In contrast to optical molasses cooling, which uses scattering of red detuned light to exert a damping force ($F_{mol} = -kv$) onto an atomic cloud to slow down the atoms (without trapping them), a MOT exerts a restoring force ($F_{MOT} = -kx$) onto an atomic cloud, allowing for cooling and trapping of the atoms. It works by utilizing the Zeeman-effect which splits the magnetic sub-levels of an atomic energy state in response to a magnetic field. By applying a quadrupole magnetic field, the energy level splitting of the atoms is made position dependent. This results, combined with red detuned light, in a position dependent restoring force towards the center of the trap where the magnetic field goes to zero [11].

The blue dipole allowed (E1) ${}^1S_0 \rightarrow {}^1P_1$ transition has a wavelength of 461 nm and a broad natural linewidth of 30.5 MHz. This transition is used for initial laser cooling/Zeeman slowing and can be used to create a blue MOT [19]. By exploiting this transition, the atoms can be cooled down to a Doppler limited temperature of $T_D = \frac{\hbar\Gamma}{2k_B} = 0.73\,\text{mK}$ (disregarding sub-Doppler cooling techniques), where $\Gamma = 2\pi \times \gamma$ with γ the natural linewidth of the transition and Γ the decay rate of the excited state ($= 1/\tau$).

To further cool down the atoms, the red spin-forbidden ($\Delta S \neq 0$), ${}^1S_0 \rightarrow {}^3P_1$ transition is commonly used in an optical molasses configuration. This transition is weakly allowed due to mixing with the dipole allowed singlet ${}^1P_1$ state and has a wavelength of 689 nm and a narrow natural linewidth of 7.4 kHz. This enables cooling of atoms to a theoretical Doppler limit of $T_D = 0.18\,\mu\text{K}$. Additionally, this transition is used to trap atoms in a red MOT. However, since the linewidth of this transition is so narrow, the temperature to which the atoms can be cooled down using this transition is actually determined by the recoil limit: $T_{rec} = \frac{\hbar^2 k^2}{2mk_B}$. This limit dictates the finite non-zero energy an atom of mass m gains, due to the recoil kick of emitting one photon with momentum k. For the intercombination line in strontium at 689 nm, this theoretical limit is $0.23\,\mu\text{K}$ [19].

Other transitions involving the ${}^3P$-manifold are the magnetic quadrupole (M2) ${}^1S_0 \rightarrow {}^3P_2$ transition with a wavelength of 671 nm and an ultra-narrow linewidth of 24 μHz, used for state preparation [20]. The doubly forbidden ${}^1S_0 \rightarrow {}^3P_0$ transition with a wavelength of 698 nm is used as the clock transition of ^{88}Sr. In bosonic strontium, this transition is only weakly allowed in the presence of an externally applied magnetic field, which creates a small admixture with the ${}^3P_1$ state. The induced linewidth of this transition is proportional to the square of this magnetic field and remains well below 1 mHz, even for strong fields $B \approx 1000\,\text{G}$, making it suitable for optical clock applications. For fermionic strontium, the admixture is attributed to the non-zero nuclear spin which creates a small magnetic moment, removing the need for an external magnetic field [19].

Additionally, three dipole-allowed (1.4 to 6.7 MHz wide) transitions at 679 nm, 688 nm and 707 nm are used for repumping atomic population between levels within the ${}^3P$-manifold. This is done by either exciting atoms from ${}^3P_1$ and ${}^3P_2$ to the ${}^3S_1$ state to maintain population of the metastable ${}^3P_0$ clock state or by exciting atoms from ${}^3P_0$ and ${}^3P_2$ to ${}^3S_1$ to pump population back into the ${}^1S_0 \rightarrow {}^3P_1$ cooling cycle [19].

2.1.2 Atomic polarizability & Optical dipole traps

Apart from trapping neutral atoms using a MOT [22], it is also possible to trap them in conservative traps using purely magnetic [23] or optical fields [24], provided the atoms are sufficiently cooled down with sub-Doppler cooling mechanisms such as polarization gradient cooling or Sisyphus cooling [11]. This work describes the creation of an optical lattice for trapping strontium atoms, so I will focus here only on the optical dipole force where I approximate the atoms to be two-level systems. A detailed overview on the principles of optical dipole traps for neutral atoms is given in [24], but a nice derivation is also found in [19].

When an atom is placed in a laser beam, the (classically described) electric field $\mathbf{E}$ induces an atomic dipole moment $\mathbf{p}$. This dipole moment oscillates at the driving frequency ω of the electric field and points along the same axis as the electric field's polarization. The amplitude of the dipole moment can be related to the driving field by [24]

$$p = \alpha E \tag{2.1}$$

where $\alpha = \alpha(\omega)$ is the complex dynamic *polarizability* of the atom. This is a measure of how easily an atom's electron cloud is distorted by a time-varying electric field and it depends on the driving frequency ω. The interaction potential between the induced atomic dipole moment and the driving field is given by [24]

$$U_{dip} = -\frac{1}{2}\langle \mathbf{pE} \rangle, \tag{2.2}$$

where the brackets denote the time average over oscillations of the field. Using Eq. 2.1, taking into account an additional factor of $\frac{1}{2}$ resulting from time averaging of an electro-magnetic wave and using that the real part of $\alpha(\omega)$ gives the energy shift of the induced dipole moment [19], we

arrive at

$$U_{dip} = -\frac{1}{4}\Re\{\alpha\}|\mathbf{E}|^2 = -\frac{1}{2\epsilon_0 c}\Re\{\alpha\}I. \tag{2.3}$$

Here, I used that the field intensity $I = \frac{1}{2}\epsilon_0 c|\mathbf{E}|^2$, where ϵ_0 is the vacuum permittivity and c the speed of light [25]. Defining the (real) total dynamic polarizability as $\alpha^i_{tot} = \Re\{\alpha(\omega)\}$ (where i represents the state of the atom), the optical dipole potential experienced by an atom in state i in a light field can be written as

$$U_{dip}(\mathbf{r}) = -\frac{\alpha^i_{tot}(\omega)}{2\epsilon_0 c}I(\mathbf{r}). \tag{2.4}$$

This equation shows that a *positive* polarizability creates an *attractive* potential. If we model the atom as a simple two-level system, equations (58-60) in [19] all depend on the factor $\frac{1}{\omega_0^2-\omega^2}$. This shows that the dynamic polarizability is positive for cases where $\omega < \omega_0$, with ω_0 the transition frequency between the ground and excited state and ω the frequency of the light field. We can therefore conclude that optical dipole traps can be formed at intensity maxima when the laser light is red-detuned from atomic resonance (the opposite is also true for blue-detuning).

Since the energy level structure of an atom is generally more complex, as seen in Fig. 2.1, our two-level approximation for the atoms will in practice not be valid. To fully understand the picture of atomic polarizability, we also need to take the transitions to other states into account. The full expression for the dynamic polarizability of a state i is then summed over all the states k it can be excited to and is given by [19]

$$\alpha^i_{\text{tot}}(\omega) = \underbrace{\alpha^i_s(\omega)}_{\text{scalar}} + \underbrace{\alpha^i_v(\omega)\sin(2\gamma)\frac{m_{J_i}}{2J_i}}_{\text{vector}} + \underbrace{\alpha^i_t(\omega)\frac{3m^2_{J_i} - J_i(J_i+1)}{2J_i(2J_i-1)}\left(3\cos^2\beta - 1\right)}_{\text{tensor}}, \tag{2.5}$$

where γ is the ellipticity angle of the light's polarization and β the angle between the electric field $\mathbf{E}$ and the quantization axis (commonly defined by the direction of the external magnetic field). Each term in Eq. 2.5 contains the sum over excited states k and are expressed by

$$\alpha^i_s(\omega) = \frac{2}{\hbar}\cdot\frac{1}{3(2J_i+1)}\sum_k \frac{|\langle k\|\mathbf{d}\|i\rangle|^2\,\omega_{ki}}{\omega^2_{ki}-\omega^2} \tag{2.6}$$

$$\alpha^i_v(\omega) = -\frac{2}{\hbar}\sqrt{\frac{6J_i}{(J_i+1)(2J_i+1)}}\sum_k(-1)^{J_i+J_k}\begin{Bmatrix}1 & 1 & 1\\ J_i & J_k & J_i\end{Bmatrix}\frac{|\langle k\|\mathbf{d}\|i\rangle|^2\,\omega}{\omega^2_{ki}-\omega^2} \tag{2.7}$$

$$\alpha^i_t(\omega) = \frac{2}{\hbar}\sqrt{\frac{10J_i(2J_i-1)}{3(J_i+1)(2J_i+1)(2J_i+3)}}\sum_k(-1)^{J_i+J_k}\begin{Bmatrix}1 & 2 & 1\\ J_i & J_k & J_i\end{Bmatrix}\frac{|\langle k\|\mathbf{d}\|i\rangle|^2\,\omega_{ki}}{\omega^2_{ki}-\omega^2}. \tag{2.8}$$

Where $\langle k\|\mathbf{d}\|i\rangle$ is the reduced electric dipole matrix element, $\omega_{ki} - \omega$ represents the energy difference between the excited state $|k\rangle$ and initial state $|i\rangle$ and the curly brackets are the Wigner 6-j symbols.

Using this full expression, the polarizabilities of two states can be equal for specific wavelengths, which cancels the differential Stark shift. The polarizabilities of a ground and excited state are equal for specific 'magic' wavelengths λ_m

$$\alpha^g_{tot}(\omega_m) = \alpha^e_{tot}(\omega_m), \tag{2.9}$$

which are called *magic* because both ground and excited state atoms experience identical potentials U_{dip} at these wavelengths according to Eq. 2.4. For strontium, using $^1S_0$ and $^3P_0$ as the ground and excited states respectively, the polarizability as a function of wavelength is plotted in Fig. 2.2. The blue trace shows the polarizability of $^1S_0$ and the red trace the polarizability of the $^3P_0$ clock state. At places where both curves cross, Eq. 2.9 is satisfied and that wavelength can be called magic. The only crossing point with a wavelength that is relatively far red-detuned from the 698 nm clock transition, or any other atomic transition (see Sec. 2.1.1) has a wavelength of $\lambda_m = 814.339 \pm 8.518$ nm. The off-resonant scattering of photons will therefore be minimal at this wavelength, resulting in minimal heating of the atoms. Additionally, this λ_m

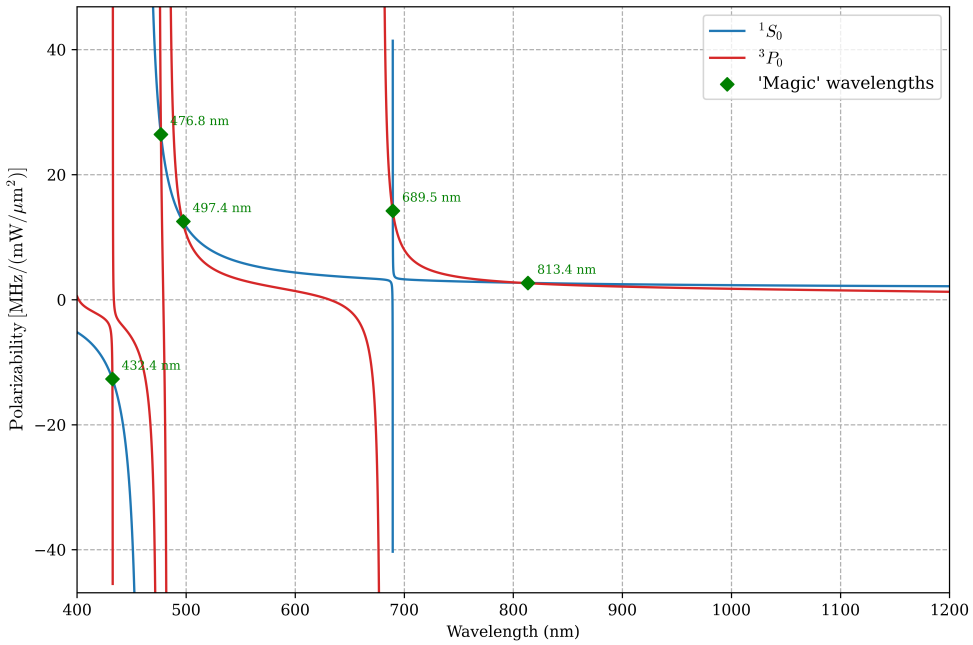


Figure 2.2: Dynamic polarizability ^{88}Sr for a range of wavelengths. The blue and red traces show the polarizabilities of $^1S_0$ and $^3P_0$ respectively, adapted from [26].

is also beneficial due to the shallow angle at which both traces cross. This means that fulfilling the magic condition here is less sensitive to frequency noise in the laser light. This results in a dipole potential that is relatively robust to frequency fluctuations, inducing only a minimal differential Stark shift when the trapping laser deviates slightly from the magic wavelength. The smaller this differential Stark shift, the less the atomic ensemble will dephase while trapped in the optical lattice.

In this experiment it is therefore chosen to use an 813 nm laser to create two oppositely propagating beams that interfere with each other. This interference will form an optical lattice used for trapping strontium atoms at the intensity maxima of the lattice. For this magic wavelength, the polarizability is found to be 286 a.u. $= 4.72 \times 10^{-39}\,\mathrm{C^2m^2J^{-1}}$ (SI) [26]. Dividing this SI value by $h\epsilon_0 c$, where h is Planck's constant, we can write it in terms of the frequency shift of the atomic energy level per unit of laser intensity (i.e. the AC Stark shift). This gives for the polarizability $\alpha'_{tot}(\omega_m) = 2.68\,\mathrm{MHz}/(\mathrm{mW}/\mu\mathrm{m}^2)$, from which the lattice depth can be calculated.

2.2 Optical resonators

Optical resonators (or cavities) are widely used devices in quantum optics and laser physics [27]. Their main purpose is to stabilize laser frequencies because they can act as precise 'flywheels' that allow laser light to resonate between two (or more) highly reflective mirrors. Due to the stable length between the cavity mirrors, it is possible to lock the frequency of a laser to this stable length, which narrows down the laser linewidth. Additionally, the light bouncing back and forth between the cavity mirrors creates a standing wave pattern. These standing waves can be used for trapping atoms in the high intensity regions of the light field, as explained in Sec. 2.1.2.

In this work, a four-mirror ring cavity is used to create an optical lattice for trapping strontium atoms. I will first focus on the working principles of (linear) Fabry-Pérot cavities and the occurrence of transverse electromagnetic modes in all types of resonators. After that I will elaborate on the differences between linear and bowtie cavities, which is a specific type of ring cavity.

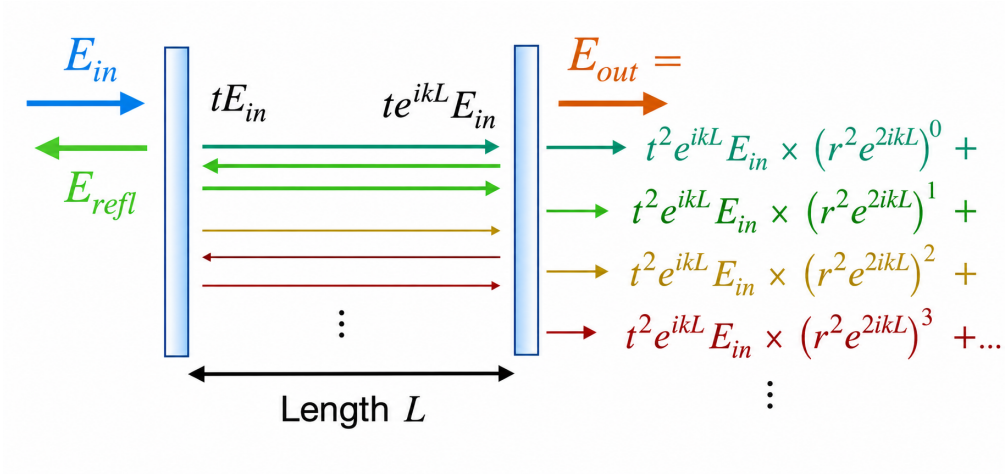


Figure 2.3: Etalon effect in a Fabry-Pérot cavity. The cavity transmission is an infinite sum of electric field amplitudes, each with an additional acquired phase of $2kL$. Adapted from [28].

2.2.1 Fabry-Pérot cavity

The simplest form of an optical cavity is a linear Fabry-Pérot (FP) cavity, which is nicely described in [29]. For this section, I will consider the cavity to be a 1D system. It consists of two highly reflective, but partially transparent mirrors placed with the reflective sides facing each other. When a laser beam with field amplitude E_{in} is incident on one of the cavity mirrors, part of it gets reflected (rE_{in}) and part of it gets transmitted (tE_{in}), where r and t are the individual mirror's amplitude reflection and transmission coefficients respectively. After the transmitted part has propagated through the cavity over a length L, it has acquired an optical phase e^{ikL} where L is the length of the cavity (neglecting the time dependence of the wave). Once arrived at the other mirror, the beam again gets partially reflected and transmitted with a ratio determined by r and t, assuming identical cavity mirrors. The transmitted part leaves the cavity and can be written as

$$E_{out,1} = t^2 E_{in} e^{ikL}. \tag{2.10}$$

Since $r \gg t$ for most cavities, most of the light stays inside the cavity and travels back toward the first mirror. After one full round-trip through the cavity, this light again partially transmits through the second mirror, leaving the cavity. Where it can now be written as

$$E_{out,2} = r^2 t^2 E_{in} e^{3ikL}. \tag{2.11}$$

Assuming a lossless cavity that is on-resonance with the incoming light, such that the optical path length of the cavity equals an integer number m of half-wavelengths:

$$nL = m\frac{\lambda}{2}, \tag{2.12}$$

where n is the intra cavity refractive index, L the length of the cavity and λ the wavelength of the laser light. If the condition in Eq. 2.12 is fulfilled, standing waves form between the cavity mirrors and the intensity of the light field inside the cavity is enhanced. In this situation, an infinite number of electric field amplitudes can transmit through the cavity, which is schematically visualized in Fig. 2.3. The electric field after the cavity can be written as an infinite sum

$$E_{out} = t^2 E_{in} e^{ikL}(1 + r^2 e^{2ikL} + r^4 e^{4ikL} + r^6 e^{6ikL} + ...). \tag{2.13}$$

Which can be rewritten as

$$E_{out} = T E_{in} e^{ikL} \sum_{n=0}^{\infty} \left(Re^{2ikL}\right)^n, \tag{2.14}$$

where $t^2 = T = 1 - R$ and $r^2 = R$ are the individual mirror's intensity transmission and reflection coefficients. We now write the expression in terms of these coefficients since the intensity (or

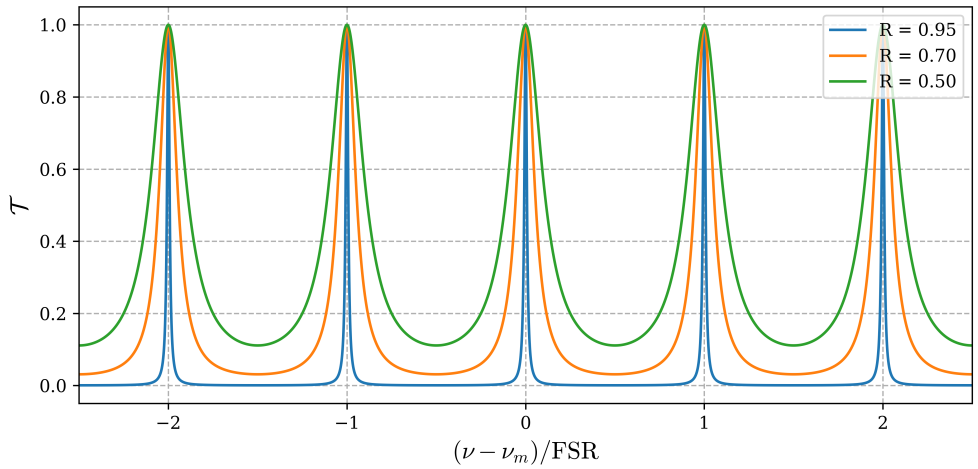


Figure 2.4: Airy distribution for different mirror reflectivities R. The cavity transmission shows a peak at every *free spectral range*, which means the cavity length is on resonance with the light being coupled in. Close to a resonance, each longitudinal mode can be approximated as a Lorentzian linewidth.

power) of the light is what we actually measure, not the electric field itself. Using the geometric sum $\sum_n^\infty x^n = \frac{1}{1-x}$, Eq. 2.14 can be written as

$$E_{out} = (1-R)E_{in}e^{ikL}\frac{1}{1-Re^{2ikL}}. \tag{2.15}$$

The cavity transmission $\mathcal{T}$ is the ratio of the light's intensity coming out of the cavity to the incoming intensity:

$$\mathcal{T} = \frac{I_{out}}{I_{in}} = \frac{|E_{out}|^2}{|E_{in}|^2} = \frac{(1-R)^2}{|1-Re^{2ikL}|^2}. \tag{2.16}$$

Using the trigonometric identity $\cos 2x = 1 - 2\sin^2 x$ and writing $kL = \frac{2\pi\nu nL}{c}$, where ν is the light's optical frequency and c the speed of light, the cavity transmission can be written as

$$\mathcal{T} = \frac{1}{1 + \frac{4R}{(1-R)^2}\sin^2(2\pi\nu nL/c)}. \tag{2.17}$$

This is known as the Airy distribution which is plotted in Fig. 2.4. Eq. 2.17 shows that the cavity transmission (for a fixed length L) is a periodic function of the laser light's frequency ν, where the light's transmission through the cavity reaches a maximum whenever $\nu = m\frac{c}{2L}$, using a refractive index of $n = 1$ in vacuum. The quantity $\frac{c}{2L}$ is commonly defined as the *free spectral range*, $FSR := \frac{c}{2L}$, such that a cavity maximally transmits light whenever the frequency ν equals an integer multiple FSR's of the cavity. Equivalently for a fixed frequency ν, the transmission is a periodic function of the cavity length L (provided the change in length is small compared to the total cavity length, such that the FSR can be assumed to stay the same). The cavity transmission as a function of ν (or L) will therefore look like Fig. 2.4, where the transmission spectrum is centered on the m^{th} longitudinal mode of the cavity and each other mode is separated by one FSR. To find the width of a transmission peak, we look at the full width at half maximum (FWHM). At half maximum, the denominator in Eq. 2.17 equals 2, or equivalently

$$\frac{4R}{(1-R)^2}\sin^2(2\pi\nu nL/c) = 1. \tag{2.18}$$

Near a resonance peak, Eq. 2.17 can be approximated as a sharp Lorentzian by using the small angle approximation ($\sin x \approx x$). Defining $\phi/2 \equiv 2\pi\nu nL/c = \frac{\pi\nu}{FSR}$ gives us

$$\frac{4R}{(1-R)^2}\left(\frac{\phi}{2}\right)^2 \approx 1 \Rightarrow \phi \approx \pm\frac{1-R}{\sqrt{R}}. \tag{2.19}$$

Since $\phi = \frac{2\pi\nu}{FSR}$, taking the derivative gives

$$\Delta\nu_{cav} = \frac{\Delta\phi}{2\pi} FSR \tag{2.20}$$

and for the FWHM $\Delta\phi = 2\frac{1-R}{\sqrt{R}}$. Therefore,

$$\Delta\nu_{cav} = \frac{1-R}{\pi\sqrt{R}} FSR \tag{2.21}$$

where $\Delta\nu_{cav}$ is the FWHM of the Lorentzian approximation, also called the cavity linewidth. By definition, the ratio of the FSR (peak separation) to $\Delta\nu_{cav}$ (peak width) is called the cavity *finesse*

$$\mathcal{F} := \frac{FSR}{\Delta\nu_{cav}} = \frac{\pi\sqrt{R}}{1-R}, \tag{2.22}$$

where R is the intensity reflection coefficient of a cavity mirror. Alternatively, the cavity linewidth can be expressed in terms of the photon lifetime τ inside the cavity by

$$\Delta\nu_{cav} = \frac{1}{2\pi\tau}. \tag{2.23}$$

Fig. 2.4 also shows that the cavity linewidth decreases for increasing mirror reflectivity R, meaning that higher finesse cavities have a narrower linewidth.

2.2.2 TEM-modes

In addition to the longitudinal modes described in Sec. 2.2.1, we can now move away from the simple 1D picture of a cavity and show that there also exist cavity eigenmodes that represent the spatial profile of the electromagnetic field inside the cavity [31]. Because the light inside a cavity propagates along the cavity axis, the electric and magnetic fields are transverse to the cavity axis. Therefore, these eigenmodes are called *transverse electromagnetic modes* (TEM) and they not only exist in linear cavities but in all types of cavities.

An optical resonator is said to be stable when the electromagnetic field distributions between the mirrors reproduce themselves after a full cavity round trip, including the shape of the wavefront. This is the case when the g-parameter stability condition is satisfied, which is given by [32]

$$0 \leq g_1 g_2 \leq 1, \tag{2.24}$$

where I assumed the cavity to consist of two concave mirrors with radii of curvature R_1 and R_2. The g-parameter is given by

$$g_i = 1 - \frac{L}{R_i}, \tag{2.25}$$

where L is the length of the cavity and R_i are the radii of curvature of the cavity mirrors. Fulfilling Eq. 2.24 therefore means that for both mirrors $L \leq R_i$ or for both mirrors that $R_i \leq L \leq 2R_i$, in order to form a stable resonator. In the simplest case of a linear cavity this can be achieved by having, at least, one concave shaped mirror surface. The complex electric field distributions are then described by the Hermite-Gaussian polynomials [30, 33]

$$\begin{aligned} E_{nm}(x,y,z) = E_0 \frac{w_0}{w(z)} H_n\left(\sqrt{2}\,\frac{x}{w(z)}\right) \exp\left(-\frac{x^2}{w^2(z)}\right) H_m\left(\sqrt{2}\,\frac{y}{w(z)}\right) \exp\left(-\frac{y^2}{w^2(z)}\right) \\ \times \exp\left[i\left(kz - (1+n+m)\arctan\left(\frac{z}{z_R}\right) + \frac{k(x^2+y^2)}{2R(z)}\right)\right], \end{aligned} \tag{2.26}$$

which is the product of a Gaussian envelope and Hermite polynomials $H_{n,m}(x)$, multiplied by a pure phase factor. For Gaussian beams, this phase factor describes the Gouy phase shift which occurs in propagation of a focused laser beam [30]. The positive integers n and m denote the order of the Hermite polynomials, the shape of the mode profile in the x- and y-direction is therefore determined by the order of n and m respectively. The intensity profiles of the lowest order Hermite-Gaussian modes, also called TEM_{nm} modes, are shown in Fig. 2.5. Each mode

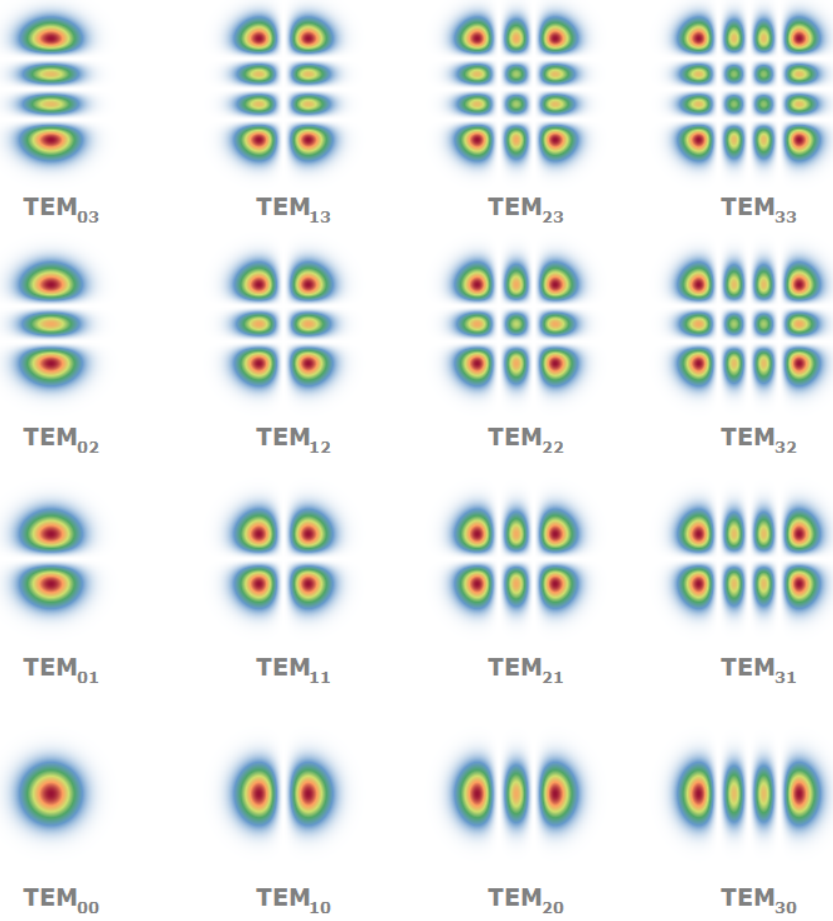


Figure 2.5: Intensity profiles of TEM_{nm} modes up to the 3^{rd} order [30].

has $n+1$ lobes in the x-direction and $m+1$ lobes in the y-direction. For a cavity with a given free spectral range FSR, the frequency of a $\mathrm{TEM}_{\mathrm{nmq}}$ mode is given by [31]

$$\nu_{nmq} = \nu_0 + qFSR + (n+m)\delta\nu_{\mathrm{TEM}}. \tag{2.27}$$

Where ν_0 is some offset frequency, q is the axial mode number as visualized in Fig. 2.4 and $\delta\nu_{\mathrm{TEM}}$ is frequency spacing of the transverse modes. This transverse mode spacing is given by

$$\delta\nu_{\mathrm{TEM}} = -FSR\frac{\varphi_G}{2\pi}, \tag{2.28}$$

where φ_G is the Gouy phase shift per cavity round trip. This shows that the transverse mode spacing is directly proportional to the order of the mode and the cavity's free spectral range.

The goal of this work is to create an optical lattice along a cavity axis. For that purpose it is desirable to work with the fundamental TEM_{00} mode, which has a uniform Gaussian intensity distribution that is centrosymmetric around the cavity axis. As described in Sec. 2.1.2, the atoms are attracted to the high intensity region of the light field. This means that for the symmetric and uniformly distributed Gaussian mode, all atoms will be trapped around the same transverse position along the cavity axis.

2.2.3 Bowtie cavity

Instead of using two mirrors to make a linear cavity, it is also possible to make a cavity with 3 or more mirrors. These types of cavities are usually called ring-resonators (or ring cavities).

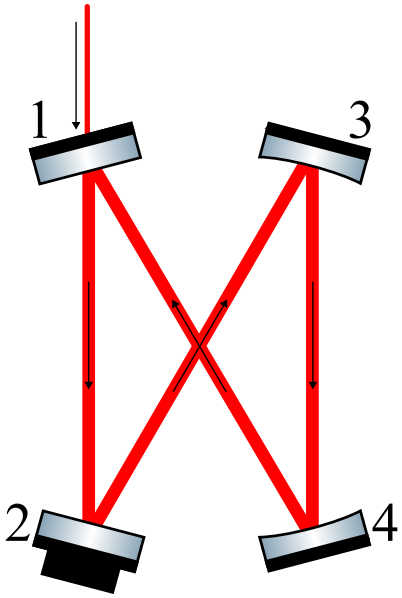


Figure 2.6: Propagation of a single beam inside the experiment's bowtie cavity. Mirrors 1 and 2 are flat, mirrors 3 and 4 are concave with a radius of curvature of 500 mm. The optical path length of this cavity can be adjusted with the piezoelectric actuator on mirror 2.

The main difference with linear cavities is that light inside a ring-resonator does not reflect back onto itself [34]. Therefore, there is no interference of light inside a ring cavity, which would be necessary to create standing waves between the mirrors. A single laser beam being coupled into a ring-cavity will therefore not create an optical lattice but it will propagate as a traveling wave in a single direction. In contrast to Eq. 2.12, the resonance condition for a ring cavity is

$$nL_{RT} = m\lambda. \tag{2.29}$$

Where L_{RT} is now the length of one *round trip* through the cavity, which must be an integer number m of the laser light wavelength.

In the mHz-machine of the superradiant clock experiment, as explained in Sec. 1.1.1, the atoms will be trapped and interrogated inside a specific ring-cavity called a 'bowtie' cavity [17]. This kind of cavity consists of four angled mirrors placed in a bowtie-like configuration, see Fig. 2.6. By coupling two separate laser beams (with the same optical frequency) into the bowtie cavity, interference between the two beams can create an optical lattice when both beams travel in opposite direction through the cavity. By shifting the frequency of one beam relative to the other, the interference pattern of the light field will become time-dependent and the optical lattice will start to move according to

$$v_{lattice} = \frac{\lambda}{2}\Delta\nu = \frac{\Delta\omega}{2k}. \tag{2.30}$$

Where $v_{lattice}$ is the speed of the moving lattice, λ is the wavelength of the light creating the lattice, k is the wave vector and $\Delta\nu = \nu_1 - \nu_2$ is the optical frequency difference between the two lattice beams (with $\Delta\omega = 2\pi \times \Delta\nu$). Since atoms can be trapped inside the optical lattice as described in Sec. 2.1.2, making the lattice have a non-zero velocity allows us to move around the atoms inside the cavity like a conveyor belt.

As shown in Fig. 2.6, two mirrors of the bowtie cavity have a spherically curved surface. Because the light of the cavity mode hits these mirrors at non-zero degree angles of incidence, astigmatism will cause the cavity mode radius to differ between the S (sagittal)- and T (tangential)-plane of the cavity [35]. Here, the T-plane is parallel to the plane of incidence and the S-plane is perpendicular to the T-plane, see Fig. 2.7. The bowtie cavity used in this experiment has curved mirrors with a radius of curvature of $R = 500\,\text{mm}$ [17]. A simulation of the cavity mode

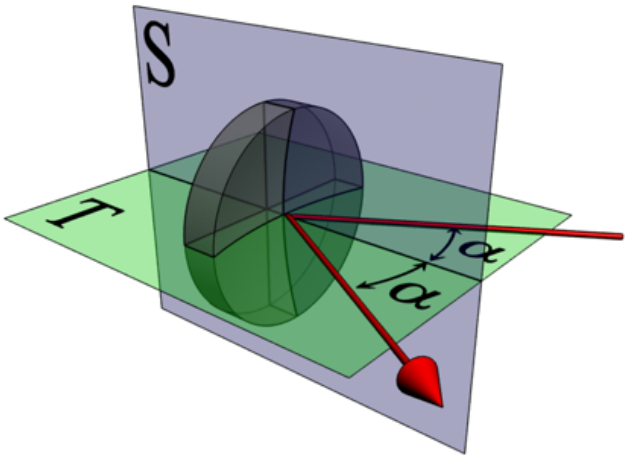


Figure 2.7: Sagittal (S) and Tangential (T) plane of a cavity (mirror), from [36].

beam radius for 813 nm and 689 nm light is given in Fig. 2.8, where the dashed black lines denote the cavity mirror positions 1 to 4 in the optical path, in the sequential order of Fig. 2.6. Both wavelengths experience a difference in mode radius between the polarization components. This difference is not the same throughout the cavity and maximizes, for both wavelengths, at the mode waist position of 25 mm between the two flat mirrors. For 813 nm, the difference in mode waist between the S- and T-plane is 1.41 μm, for 689 nm this is 1.30 μm. This effect is not present in linear Fabry-Pérot cavities because the light inside these cavities hits the curved mirrors at 0° angle of incidence, creating identical foci in both planes. Because the waist of the cavity mode is realized between the two flat mirrors, the intensity of the light field is also the highest there. Since the depth of the optical lattice is the deepest where the light's intensity is the highest, see Eq. 2.4 in Sec. 2.1.2, it explains why we want to trap the atoms between these two flat cavity mirrors.

Another important distinction between linear and ring cavities, is the occurrence of polarization mode dependent cavity resonances. Ring cavities are intrinsically birefringent due to the non-zero angle between the cavity mode beam and mirror surface normal [35]. This means that S- and P-polarized light (relative to the plane of incidence of the cavity mirrors) experience different effective refractive indices when propagating through the cavity. The difference in refractive index lifts the degeneracy of the cavity resonance frequencies between both polarization components [37]. The birefringence originates from the cavity mirror's HR-coating, which is made from a dielectric material. When a laser beam hits this dielectric coating at a non-zero degree angle, the light will experience a phase shift and this shift is different for S- and P-polarized light. Since light entering a bowtie cavity will only transmit through it when the resonance condition in Eq. 2.29 is met, a difference in phase shift will result in two distinct cavity resonance frequencies for the two orthogonal polarization components. The amount of frequency shift is then given by [38]

$$\delta\nu = \nu_s - \nu_p = \frac{\Delta\phi_s - \Delta\phi_p}{2\pi} FSR, \tag{2.31}$$

where s and p denote the polarization components and $\Delta\phi$ is the phase shift experienced in one cavity round trip. Since frequency and length play the same role in the cavity transmission function, as shown in Eq. 2.17, this effect can be made visible by scanning the cavity length while monitoring the transmitted light. This is particularly visible in high finesse ring cavities due to their narrow linewidth, which makes it easier to observe a shift in the resonance frequency. In linear Fabry-Pérot cavities, the 0° angle at which the light reflects from the mirrors makes it impossible to distinguish between S- and P-polarization components. However, the dielectric coating still results in a difference in mirror reflectivity, depending on the light's polarization. This makes the finesse of a linear cavity polarization dependent. The 0° angle of incidence is what makes linear cavities inherently non-birefringent, resulting in no shift of the resonance frequency when the polarization angle of the light being sent into the cavity is changed. In this

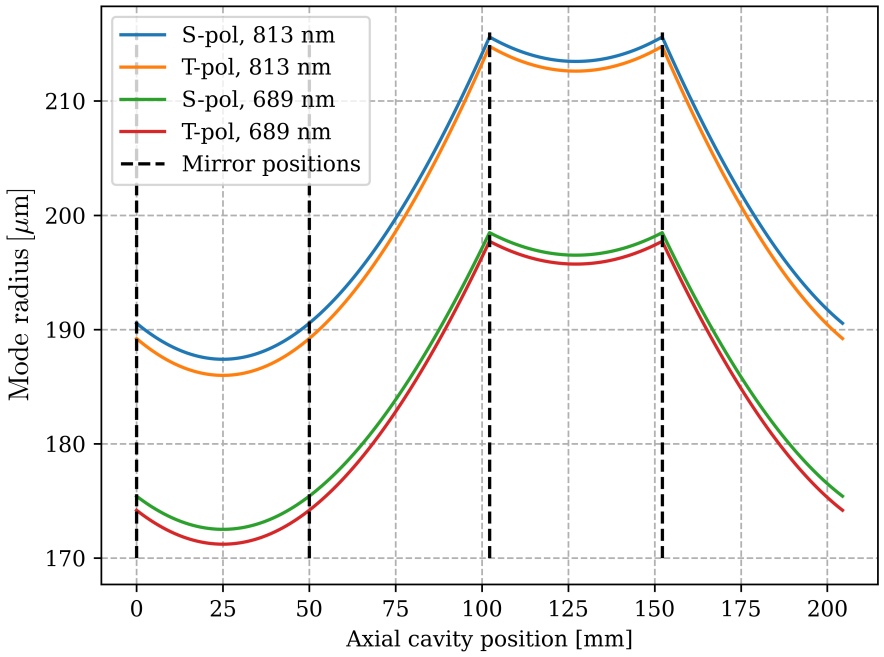


Figure 2.8: Difference in cavity mode radius between the S- and T-plane of the bowtie cavity. The dashed black lines denote the cavity mirror positions along the optical path. From left to right, the ordering of the mirrors is 1-2-3-4, following the numbering in Fig. 2.6.

work, the polarization mode dependent shift of the bowtie cavity resonance frequency has been measured and characterized in Sec. 6.2.2.

2.3 Pound-Drever-Hall technique

To create an optical lattice inside the bowtie cavity, the cavity length needs to be stabilized to the frequency of the 813 nm laser. Equivalently, the 813 nm laser could be locked to the bowtie cavity. But since the cavity, in that case, will not have a stable frequency reference anymore, its length will change over time due to temperature fluctuations. The frequency of the laser will therefore follow this drift, moving away from the 'magic' wavelength will influence the depth of the lattice over time and induce a differential light shift onto the atoms trapped in the lattice. As described in Sec. 2.2.1, light can only resonantly oscillate inside a cavity when the optical path length between the cavity mirrors equals an integer number of half-wavelengths. This means that the length of the cavity needs to be stabilized to nm-level precision.

To do this, we make use of the 'Pound-Drever-Hall' (PDH) technique [39]. As shown in Fig. 2.3, when a light beam is incident on a cavity mirror, part of it gets reflected. The magnitude of the reflected electric field is actually a combination of the beam being promptly reflected from the first cavity mirror, plus the field leaking out of the (left-hand) cavity mirror

$$E_{ref} = E_{prompt} + E_{leak}. \tag{2.32}$$

Following the same steps as in Sec. 2.2.1, we can write the geometric sum of the total leakage field as a function of the incident field

$$E_{leak} = t^2 r e^{2ikL} E_{in} \sum_{n=0}^{\infty} \left(r^2 e^{2ikL}\right)^n, \tag{2.33}$$

which can be rewritten as

$$E_{leak} = E_{in} \frac{t^2 r e^{2ikL}}{1 - r^2 e^{2ikL}}. \tag{2.34}$$

The promptly reflected field is simply $E_{prompt} = -rE_{in}$, making the total reflected field

$$E_{ref} = E_{in}\left(-r + \frac{t^2 r e^{2ikL}}{1 - r^2 e^{2ikL}}\right). \tag{2.35}$$

Using $t^2 = 1 - r^2$ and $2kL = \frac{\omega}{FSR}$, Eq. 2.35 can be rewritten and we obtain the ratio between E_{ref} and E_{in} which is the amplitude reflection coefficient of the cavity:

$$F(\omega) = \frac{E_{ref}}{E_{in}} = \frac{r(e^{i\frac{\omega}{FSR}} - 1)}{1 - r^2 e^{i\frac{\omega}{FSR}}}. \tag{2.36}$$

We can now use this *frequency dependent* reflection coefficient to measure whether the cavity is below or above a resonant length for the laser. When the cavity is perfectly on resonance with the laser (assuming a lossless cavity), the total reflected field vanishes because the leakage field and promptly reflected field are exactly π out of phase. When the cavity length is not perfectly on resonance with the laser, but close enough to be within the cavity linewidth, the phase difference between E_{prompt} and E_{leak} will not be exactly π and E_{ref} will not completely vanish. Because the phase of the reflected field flips sign across a resonance, the phase of E_{ref} could tell us if the cavity is below or above resonance. This provides us with more information than only looking at the cavity transmission, which cannot distinguish between the cavity being below or above a resonance. Since there are no electronics that can measure the electric field (and phase) of a light wave, we make use of the PDH-method.

By modulating the phase of the incident laser beam using an electro-optic modulator (EOM), the incoming electric field becomes [39]

$$E_{inc} = E_0 e^{i(\omega t + \beta \sin \Omega t)}, \tag{2.37}$$

where ω is the carrier frequency of the laser, β the depth of the phase modulation and Ω the modulation frequency. This expression can be expanded using Bessel functions into [39]

$$E_{inc} = [J_0(\beta)e^{i\omega t} + J_1(\beta)e^{i(\omega+\Omega)t} - J_1(\beta)e^{i(\omega-\Omega)t}]. \tag{2.38}$$

This equation shows that the incoming beam consists of a carrier at frequency ω and two sidebands at frequencies $\omega \pm \Omega$, with opposite phase. $P_0 \equiv |E_0|^2$ is the total power in the incident beam, the power in the carrier can therefore be written as

$$P_c = J_0^2(\beta)P_0 \tag{2.39}$$

and in each first-order sideband as

$$P_s = J_1^2(\beta)P_0. \tag{2.40}$$

To determine the reflected beam's field, we can treat the carrier and both sidebands as three independent beams and multiply them with their reflection coefficient at the appropriate frequency [39]

$$E_{ref} = E_0[F(\omega)J_0(\beta)e^{i\omega t} + F(\omega+\Omega)J_1(\beta)e^{i(\omega+\Omega)t} - F(\omega-\Omega)J_1(\beta)e^{i(\omega-\Omega)t}]. \tag{2.41}$$

Since we can only measure the power of the reflected beam on a photodiode, $P_{ref} = |E_{ref}|^2$ is what we are interested in

$$\begin{aligned} P_{ref} = |E_0|^2\{&|F(\omega)|^2 J_0^2 + J_1^2(|F(\omega+\Omega)|^2 + |F(\omega-\Omega)|^2) \\ &+J_0 J_1[(F^*(\omega)F(\omega+\Omega) - F(\omega)F^*(\omega-\Omega))e^{i\Omega t} \\ &+(F(\omega)F^*(\omega+\Omega) - F^*(\omega)F(\omega-\Omega))e^{-i\Omega t}] \\ &-J_1^2[F^*(\omega+\Omega)F(\omega-\Omega)e^{-2i\Omega t} + F(\omega+\Omega)F^*(\omega-\Omega)e^{2i\Omega t}]\}. \end{aligned} \tag{2.42}$$

This can be simplified to

$$\begin{aligned} P_{ref} = P_c|F(\omega)|^2 + P_s\{&|F(\omega+\Omega)|^2 + |F(\omega-\Omega)|^2\} \\ &+\sqrt{P_c P_s}\{(F^*(\omega)F(\omega+\Omega) - F(\omega)F^*(\omega-\Omega))e^{i\Omega t} \\ &+(F(\omega)F^*(\omega+\Omega) - F^*(\omega)F(\omega-\Omega))e^{-i\Omega t}\} \\ &+(2\Omega \text{ terms}) \end{aligned} \tag{2.43}$$

and rewritten as

$$\begin{aligned} P_{ref} = P_c|F(\omega)|^2 + P_s\{|F(\omega+\Omega)|^2 + |F(\omega-\Omega)|^2\} \\ +\sqrt{P_cP_s}\{(F^*(\omega)F(\omega+\Omega) - F(\omega)F^*(\omega-\Omega))[\cos\Omega t + i\sin\Omega t] \\ +(F(\omega)F^*(\omega+\Omega) - F^*(\omega)F(\omega-\Omega))[\cos\Omega t - i\sin\Omega t]\} \\ +(2\Omega \text{ terms}). \end{aligned} \tag{2.44}$$

Using the relations

$$c = a + bi,\ \ c^* = a - bi,\ \ c + c^* = 2a = 2\Re\{c\},\ \ c - c^* = 2bi = 2i\Im\{c\} \tag{2.45}$$

Eq. 2.44 can be split up into a real and imaginary part [39]

$$\begin{aligned} P_{ref} = P_c|F(\omega)|^2 + P_s\{|F(\omega+\Omega)|^2 + |F(\omega-\Omega)|^2\} \\ +2\sqrt{P_cP_s}\{\Re[F^*(\omega)F(\omega+\Omega) - F(\omega)F^*(\omega-\Omega)]\cos\Omega t \\ +\Im[F(\omega)F^*(\omega-\Omega) - F^*(\omega)F(\omega+\Omega)]\sin\Omega t\} \\ +(2\Omega \text{ terms}). \end{aligned} \tag{2.46}$$

We are interested in the phase of the reflected carrier, because this tells us whether we are above or below a resonance. We therefore only look at the beat note between the first order sidebands and the carrier, which happens at the modulation frequency Ω. In Eq. 2.46 the cosine and sine terms oscillate at the frequency Ω. For fast modulation frequencies ($\Omega >> FSR/\mathcal{F}$), which is the case in this project, the carrier can be near a cavity resonance while the sidebands are not. In this case $F(\omega \pm \Omega) \approx 1$ and the term

$$F(\omega)F^*(\omega-\Omega) - F^*(\omega)F(\omega+\Omega) \approx 2i\Im\{F(\omega)\} \tag{2.47}$$

becomes purely imaginary, resulting in only the sine term in Eq. 2.46 surviving.

In practice, we measure the reflected power using a photodiode. The output of this detector contains all the terms in Eq. 2.46, we are only interested in the sine term which we isolate using a band pass filter that filters out all terms oscillating at Ω. By using a mixer we can multiply this signal with some local oscillator (LO) signal at Ω', that has a tunable phase. The output of the mixer will be the product of the two and contains the term

$$\sin(\Omega t)\sin(\Omega' t) = \frac{1}{2}\{\cos[(\Omega-\Omega')t] - \cos[(\Omega+\Omega')t]\}. \tag{2.48}$$

By setting the LO frequency equal to the modulation frequency ($\Omega' = \Omega$), the $\cos[(\Omega-\Omega')t]$ term will turn into a dc-signal. We isolate this dc-signal with a low-pass filter on the output of the mixer. Now we are left with our error signal

$$\epsilon = 2\sqrt{P_cP_s}\Im\{F(\omega)F^*(\omega-\Omega) - F^*(\omega)F(\omega+\Omega)\}, \tag{2.49}$$

which is plotted in Fig. 2.9 as a function of ω/FSR.

When the carrier is near a cavity resonance, Eq. 2.49 can be written as

$$\epsilon \approx 4\sqrt{P_cP_s}\Im\{F(\omega)\} \tag{2.50}$$

with the help of Eq. 2.47. In addition, near resonance we can write

$$\frac{\omega}{FSR} \approx 2\pi N + \frac{\delta\omega}{FSR}, \tag{2.51}$$

where N is an integer number of FSR's and $\delta\omega$ is the deviation of the laser frequency from a cavity resonance. Going back to Eq. 2.36, writing Eq. 2.22 as $\mathcal{F} = \frac{\pi r}{1-r^2}$ and using Eq. 2.21, the reflection coefficient becomes

$$F(\omega) \approx \frac{r\left(i\frac{\delta\omega}{\delta\nu_{cav}}\frac{1-r^2}{\pi r}\right)}{1-r^2\left(1+i\frac{\delta\omega}{\delta\nu_{cav}}\frac{1-r^2}{\pi r}\right)} \tag{2.52}$$

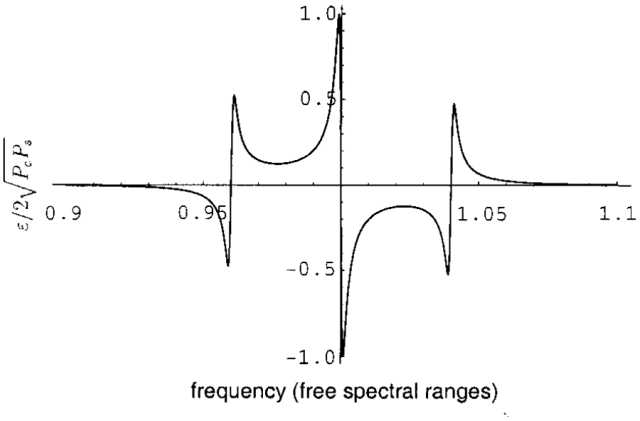


Figure 2.9: Pound-Drever-Hall error signal, $\epsilon/2\sqrt{P_c P_s}$ vs ω/FSR for high modulation frequencies. Fig. 7 from [39].

where $\delta\nu_{cav}$ is the cavity linewidth and I made use of the first-order Taylor expansion $e^x \approx 1+x$. The near-resonance approximation holds when $\delta\omega << \delta\nu_{cav}$, which can be used to further approximate the reflection coefficient to

$$F(\omega) \approx \frac{i}{\pi}\frac{\delta\omega}{\delta\nu_{cav}}. \tag{2.53}$$

The error-signal therefore becomes

$$\epsilon \approx \frac{4}{\pi}\sqrt{P_c P_s}\frac{\delta\omega}{\delta\nu_{cav}}, \tag{2.54}$$

which shows that, near a cavity resonance, the error signal becomes linearly dependent on the laser's frequency deviation (or equivalently, linearly dependent on the cavity's length deviation). This linear slope allows standard tools of control theory, such as PID loops, to be used to stabilize laser frequencies or cavity optical path lengths [39]. Additionally, Eq. 2.54 allows us to calculate the linear response of the error signal, that quantifies the sensitivity of the lock. This is done in Sec. 5.4 with the measured value of the cavity linewidth.

Chapter 3

Laser systems

The theory described above now allows us to understand the working principles of cavities and explains how we can make a (moving) optical lattice inside a ring cavity. The next step is to look at the lasers that will be used to do this.

As mentioned before, in this project an 813 nm laser will be used to create the optical lattice. Once atoms are loaded inside the cavity and trapped inside this optical lattice, we need to be able to probe them to an excited state. Initially this will be the $^3P_1$ state, where it must be possible to switch to the $^3P_0$ clock state later on. To study the first atom-cavity interactions, the $^1S_0 \rightarrow {}^3P_1$ transition is more suitable than the $^1S_0 \rightarrow {}^3P_0$ clock transition, due to its broader linewidth. In this chapter, I will therefore focus only on the 689 nm laser that will be used to initially probe the $^1S_0 \rightarrow {}^3P_1$ transition. In the future this will be changed to the 698 nm laser, used to probe the $^1S_0 \rightarrow {}^3P_0$ clock transition.

This chapter provides an overview of both 813 nm and 689 nm laser systems, starting with the latter one. After that, the frequency shifting setup for the 689 nm light is shortly mentioned. This setup needed to be built in order to find the right probe frequency for the $^1S_0 \rightarrow {}^3P_1$ transition in strontium. It also enables us to scan the frequency of the 689 nm probe beam to study atom-cavity interactions, such as the detection of normal mode splitting.

Next, the planned locking system for the 813 nm laser is shown schematically, its implementation is ongoing and will be completed in future work. Additionally, the frequency of the (locked) 813 nm lattice light also needs to be shifted. This is necessary in order to simultaneously bring the bowtie cavity on resonance with the probe and lattice light. For this, I built a frequency shifting setup using a single- and double-pass AOM configuration.

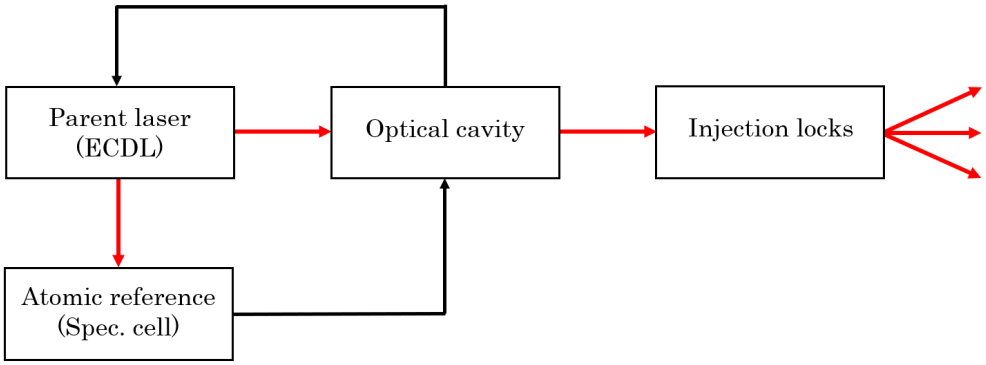


Figure 3.1: 689 nm laser system used in the lab. Red lines show the path of light, black lines are an electronic feedback signal.

3.1 The 689 nm laser system

Initially, atoms inside the cavity will be probed on the 7.4 kHz wide $^1S_0 \rightarrow {}^3P_1$ transition to show atom-cavity coupling and other cavity QED effects. This transition is broader and therefore better accessible than the ultra narrow $^1S_0 \rightarrow {}^3P_0$ clock transition. To probe this transition, the 689 nm laser system is needed as described in [40] and [41].

A schematic overview of the red laser system is given in Fig. 3.1. The system starts with a *DL Pro* external cavity diode laser (ECDL) from *Toptica*. This parent laser is locked to a tunable optical cavity providing short-term stability. For the long-term stability the cavity itself is locked to an atomic reference by using a spectroscopy cell containing a hot gas of strontium atoms. After the frequency stabilization system, the linewidth of the parent laser is narrow enough to target the 7.4 kHz transition in strontium. The light from this narrow linewidth laser is amplified and distributed over multiple labs by a series of injection locks, transferring the stability of the parent laser. In Sec. 4.1 I will give a more detailed explanation about the working principle of injection locks.

3.1.1 689 nm shifting setup

In order to probe atoms inside the cavity, we need to be able to tune the frequency of the 689 nm light to find the corresponding transition. In addition, having a tunable frequency will allow us to detect normal mode splitting on the $^1S_0 \rightarrow {}^3P_1$ transition, once atoms are trapped inside the cavity. This frequency splitting will give us an indication of the atom-cavity coupling strength.

Before the light from one of the injection locks is coupled into the cavity, it is sent through the frequency shifting setup shown in Fig. 3.2. The setup uses an 80 MHz 'acousto-optic modulator' (AOM) from *Gooch & Housego*, in double-pass configuration. The 20 MHz RF bandwidth of this AOM allows us to scan the frequency of the light while probing the atoms. This way, the exact resonance frequency of the transition can be found. Because the -1st diffraction order is used for the double pass AOM, the frequency of the light is shifted by -160 MHz. This shift compensates the +80 MHz shift coming from the 689 nm injection lock setup and an additional +80 MHz shift from the AOM on the bowtie cavity setup later on, as shown in Fig. 5.5. This way, the double-pass AOM can scan the frequency around zero detuning from the theoretical atomic transition to find the probe frequency of the atoms.

3.2 The 813 nm laser system

To create the (moving) optical lattice at the magic wavelength for the clock transition in strontium, an 813 nm laser is used. Because the locking system for this laser was not finished yet during this project, I have used it as a free running laser or locked it to a free running optical cavity using the PDH-method. I will anyway give an overview of how the 813 nm laser system will look like once it is finished, which will justify why an 813 nm frequency shifting setup is needed.

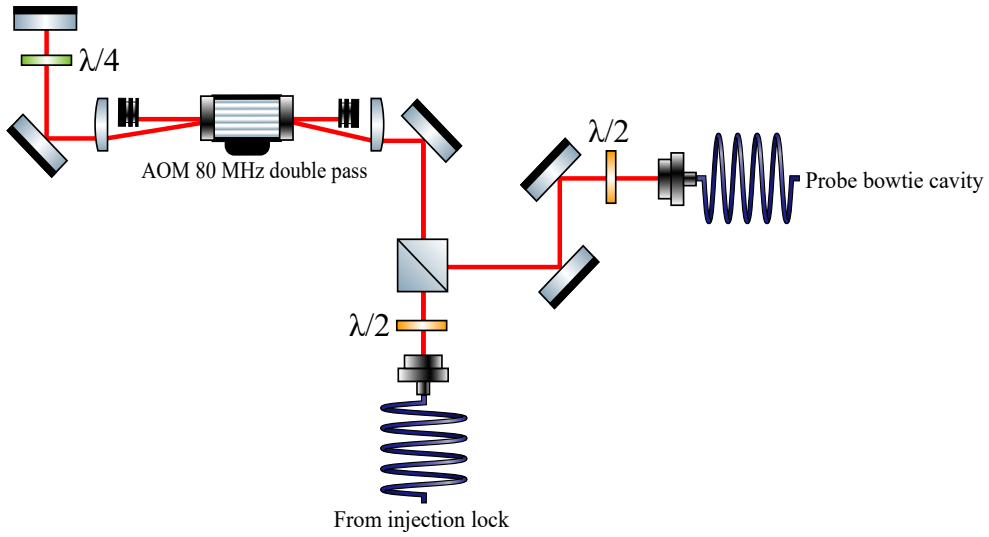


Figure 3.2: Frequency shifting setup for the 689 nm light, used to scan the probe frequency.

A schematic overview of the 813 nm laser system is given in Fig. 3.3. It starts with a *Toptica DL Pro* grating stabilized tunable single-mode diode laser, which is locked to a tunable optical cavity, using the PDH-method, providing short term stability. This cavity will then be locked to an ultra-stable 698 nm clock laser, which itself is locked to an ultra low expansion (ULE) cavity providing short term stability to the frequency of the clock laser. For the long term stability the 698 nm laser will be locked to an atomic reference using a zero-deadtime optical clock. The frequency stability of the zero-deadtime clock will thus be transferred to the 813 nm laser via a transfer cavity.

3.2.1 813 nm shifting setup

Because we want to trap and probe the atoms at the same time, the bowtie cavity needs to be simultaneously resonant with the 813 nm and 689 nm light. We lock the bowtie cavity to the 813 nm light, as I will explain later on in Sec. 5.4, but this does not necessarily mean that the frequency of the 689 nm probe light overlaps with an integer number of FSR's of the cavity. Since the 689 nm laser will be used to probe the atomic transition, the frequency shift it acquires by its shifting setup will only be very small. Therefore, the 813 nm light needs to be shifted. The lock of the cavity to this light will follow the frequency shift, where we need to find a frequency where both the 813 nm and 689 nm light are resonant with a FSR for the same cavity length. In the worst case, the non-shifted and locked 813 nm light could have a frequency exactly between two FSR's of the 689 nm light. We therefore need to be able to shift the frequency of the 813 nm light upward and downward by at least half a FSR. The FSR of the bowtie cavity is roughly 1.47 GHz, see Sec. 5.1, requiring a shift of +735 MHz (or -735 MHz). This could be done using the frequency shifting setup shown in Fig. 3.4. It uses two AOM's from *Gooch & Housego*, one with a center frequency of 200 MHz and one at 350 MHz. For the first AOM the $+1^{\text{st}}$ order is used, shifting the light's frequency up by a fixed 200 MHz. We use the second AOM in a double-pass configuration, also utilizing the $+1^{\text{st}}$ order. At the center frequency of 350 MHz this gives an additional shift of +700 MHz. The RF bandwidth of the second AOM is 150 MHz, resulting in a frequency tunability of 300 MHz in double-pass configuration. This allows us to create frequency shifts from +750 MHz up to +1.05 GHz. Once the 813 nm laser is not free running anymore but locked at a fixed frequency, we can test whether this shifting

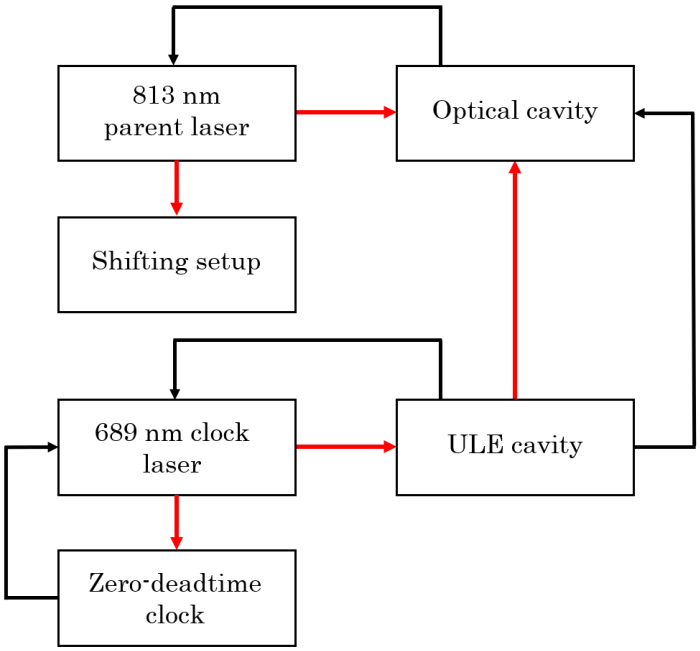


Figure 3.3: Planned 813 nm laser system. Red lines show the path of light, black lines are an electronic feedback signal.

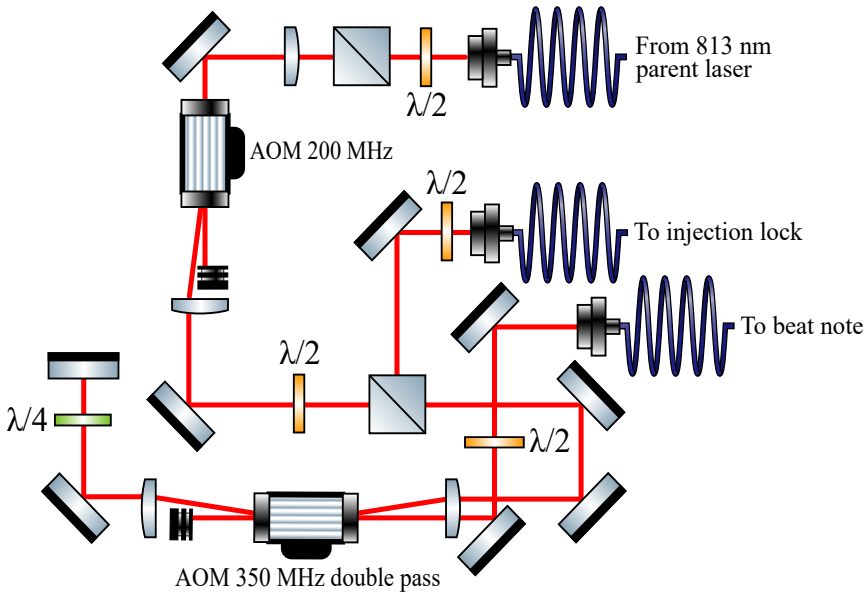


Figure 3.4: Frequency shifting setup for the 813 nm light, used to shift the cavity to a mode resonant with the 689 nm light. Part of the light is picked up and used to make a beat note with the child laser.

AOM usage	Abs. shift	Tunability
Single-pass 200 MHz, $\pm1^{st}$ order Double-pass 350 MHz, $\pm1^{st}$ order	$\pm$750 MHz to $\pm$1.05 GHz	300 MHz
Double-pass 200 MHz, $\pm1^{st}$ order Double-pass 350 MHz, $\pm1^{st}$ order	$\pm$900 MHz to $\pm$1.3 GHz	400 MHz
Single-pass 200 MHz, $\pm1^{st}$ order Double-pass 350 MHz, $\mp1^{st}$ order	$\mp$350 MHz to $\mp$650 MHz	300 MHz

Table 1: Overview of induced frequency shifts and tunabilities for the 813 nm shifting setup. The absolute shift is the total amount by which the incoming light's frequency gets shifted, the tunability shows by how much you can change this shift, using the full bandwidth of one or two double-pass AOMs.

bandwidth is enough to bring the cavity on resonance with both wavelengths. If this is not the case, it is possible to change for example to using the -1^{st} order for the first and/or second AOM to create the right combination of frequency shifts, which should be easy to implement. If more tunability is required, the 200 MHz AOM could also be used in double-pass configuration. This AOM has an RF bandwidth of 50 MHz, which would increase the frequency tunability range by 100 MHz. An overview of the frequency shifts and tunabilities for different combinations of diffraction orders is given in Tab. 1.

It is important to mention that shifting the frequency of the 813 nm light will result in the lattice beams not fulfilling the exact 'magic' wavelength condition anymore, as mentioned in Sec. 2.1.2. This will result in a differential light shift between the ground and excited state, causing them to experience different potential depths from the optical lattice. During interrogation, the atomic superposition will accumulate an additional phase due to this shift. In principle this will only lead to a systematic offset in the measured clock frequency, but since the atoms are trapped in a spatially varying light field (i.e. an optical lattice), the differential light shift will also be

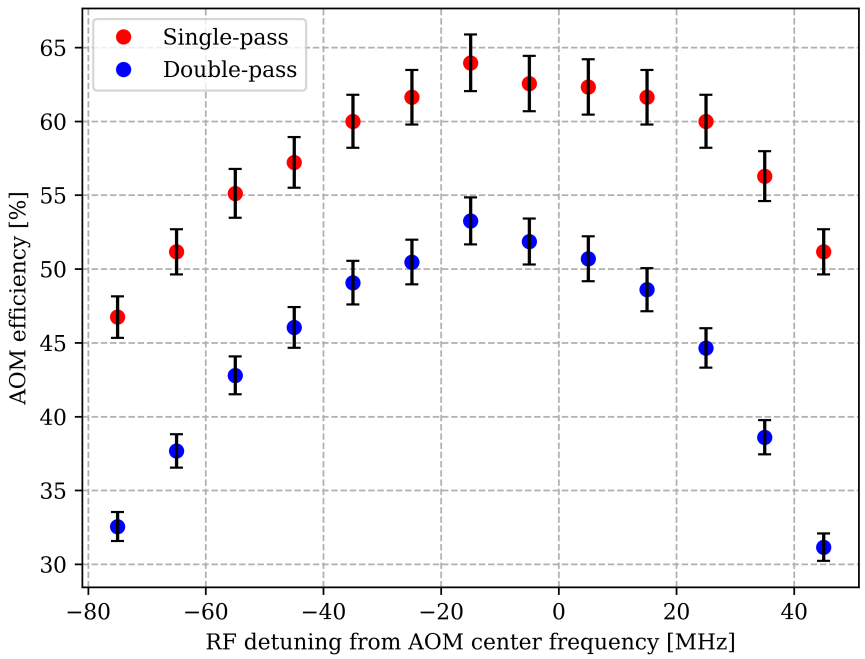


Figure 3.5: Efficiency of the +1^{st} order of the 350 MHz AOM vs RF detuning from AOM center frequency. Red data denotes single-pass and blue data double-pass diffraction, error bars originate from the measurement uncertainty of the power meter.

spatially varying. This will cause each atom in the lattice to accumulate a (slightly) different extra phase over time. This dephasing will lead to decoherence of the atomic ensemble. Fortunately, as shown in Fig. 2.2 the crossing of ground and excited state polarizability curves is very shallow, which means that slightly deviating from the exact magic wavelength will not immediately result in a large differential light shift. To quantify this, we can compare the collective atom-cavity coupling rate [42]

$$\Gamma_{col} = 2g\sqrt{N}, \tag{3.1}$$

where g is the single atom-cavity coupling parameter and N is the number of atoms inside the cavity, with the differential light shift

$$\Delta_{diff} = \delta_e - \delta_g. \tag{3.2}$$

Where $\delta_{e,g}$ are the shifts of the excited and ground state energy levels. If $\Gamma_{col} >> \Delta_{diff}$, then the collective coupling to the cavity mode can 'resynchronize' the phase of the atoms faster than the varying light field can decohere them. Since it is not known yet how many atoms we can load into the cavity, I will leave the exact calculation for future work.

Note that changing the operating frequency of an AOM will change its efficiency as shown in Fig. 3.5. Where the diffraction efficiency of the $+1^{\text{st}}$ order is measured while scanning the RF sent to the 350 MHz AOM, for both the single- and double-pass configuration. The efficiency of the double-pass configuration falls down quicker than for the single-pass, because the AOM's efficiency is squared for a double-pass configuration. This means that changing the RF of the double-pass AOM can result in a loss of available optical power.

Chapter 4

Injection lock 813 nm laser

In the previous chapter I explained that the light used to create the optical lattice, is coming from a Toptica DL Pro ECDL laser. Because the light from this laser is used by multiple people in multiple labs, the available optical power is limited to 5-10 mW. This light also passes through a 20 m long fiber and the frequency shifting setup, which further reduces the power to around 2 mW. Since this light needs to be brought to the cavity via another setup (see Fig. 5.5 in Sec. 5.3), where it is split up into two lattice beams, at most 0.5 mW in each beam could be sent into the cavity. Using the expression for the optical dipole potential experienced by an atom in a light field, given by Eq. 2.4, we can calculate the estimated trap depth of the optical lattice that is reachable with this optical power. Based on a best-case estimated cavity finesse of 7000 reported in [17] and using a cavity coupling efficiency of $\sim$40 %, the obtainable optical power at an antinode of the lattice is 1.78 W. This translates to an intensity of 1.6×10^{-2} mW/μm^2. Multiplying this by the polarizability at the magic 813 nm wavelength, results in an estimated maximum obtainable trap depth of 1.05 μK. Based on simulations from [16], the average energy of the atoms trapped in the reservoir inside the bowtie cavity is 12 μK. This means that we need at least a ten times higher intensity at the anti-nodes of the optical lattice. To achieve this, we need to be able to amplify the power of the light to at most 10 mW in each lattice beam before the cavity. In this project, this is done with an *injection lock* where light from the DL Pro laser is *seeded* into a Fabry-Pérot diode laser. This amplifies the available optical power at the seed frequency, while maintaining the linewidth of the seed laser. Injection locking is beneficial compared to using a (tapered) amplifier because it does not generate broadband amplification of spontaneous emission, which is present in such amplifiers.

This chapter provides an overview of the injection lock built for the 813 nm laser. First, the working principle of injection locking is shortly described where I primarily focus on this specific injection lock. The hardware used for this lock is mentioned together with the step by step process of locking the child laser to the seed laser and a schematic overview of the setup is given. Second, the quality of the injection lock is characterized by measuring a beat note between the seed light and child laser output. This indicates a fixed, phase-locked, frequency offset between the two lasers. Third, the long-term stability of the injection lock is monitored using a wavemeter. Where we see that the child laser perfectly follows the frequency drift of the free-running parent laser.

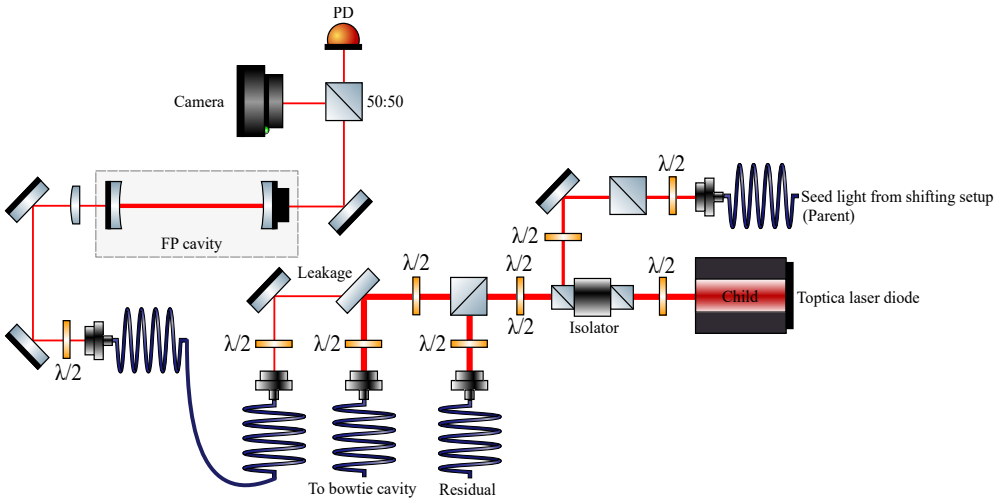


Figure 4.1: Injection lock setup for the 813 nm laser. The lock is monitored with the transmission of a scanning FP cavity.

4.1 Building 813 nm injection lock

The principle of injection locking works by injecting the light coming from a stable *parent* laser, into another free running *child* laser [43]. A high power child (or slave) laser will be forced to operate at the same frequency as the light coming from a low power parent (or seed) laser that is being injected into it, provided that the frequencies of the seed laser and free running child laser are sufficiently close. This way, a high power laser output with low intensity noise and low phase noise can be created.

In this work, the frequency shifted light coming from the (yet free running) 813 nm ECDL is used as seed light for an independently free running child diode laser. This child laser is composed of a *Toptica Eagleyard* single mode laser diode with a tunable center wavelength from 796 nm to 816 nm and a typical free running spectral width of 1 nm [44]. The tunability of the lasing wavelength is realized by changing the temperature of and current through the diode. This is done using a Thorlabs LM14S2 butterfly laser diode mount, which is controlled with a Thorlabs LDC210C laser diode controller and Thorlabs TED200C temperature controller with PID control feedback to keep the diode's temperature stable.

A diode laser consists of a semiconductor material where the back side has an HR-coating, creating a Fabry-Pérot like cavity between this coating and the diode-air interface. This results in an emitted spectrum with a 'comb-like' structure under a broad Gaussian envelope. The semiconductor material has an energy bandgap that determines the wavelength of the photons it emits. By changing the temperature of the diode, the energy bandgap changes, resulting in a variable emission wavelength. Additionally, varying the temperature can also expand or contract the semiconductor material, affecting the distance between the reflective surfaces which will shift the longitudinal modes of the cavity. The specific laser diode used here has a (positive) temperature coefficient of 0.28 nm/K. The emitted power of the laser diode is controlled by changing the current through the semiconductor material. This changes the density of charge carriers in the active layer, where more electron-hole recombinations will lead to more emitted photons and thus a higher output power. The charge carrier density also influences the refractive index of the semiconductor material, again changing the optical path length of the diode's cavity and therefore shifting the resonant cavity modes. Additionally, the amount of current has thermal effects on the semiconductor junction, heating up the material for higher currents, resulting in

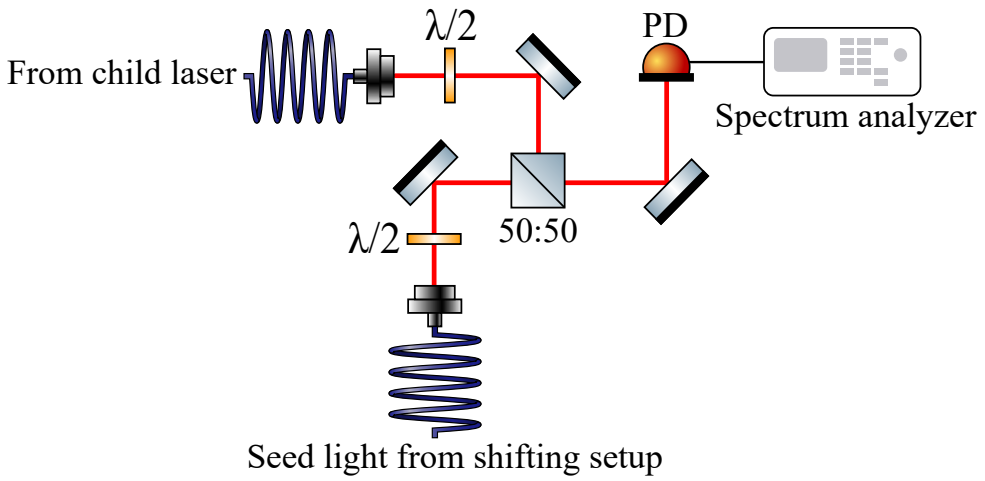


Figure 4.2: Setup used to make a beat note between the seed light and child laser output.

a similar change of the energy bandgap [45]. This effect should however be minimal because the diode is temperature stabilized.

The injection lock setup is visualized in Fig. 4.1. The seed light is first passed through an isolator before injection into the child laser. This separates the seed light path from the child laser output, but more importantly it ensures that any high power light coming from the child laser is not coupled back into the seed fiber, which could damage the DL Pro parent laser. In order to force lasing on the injected frequency, proper mode matching of the seed light with the FP diode is needed. This is done with the collimator lens of the seed light fiber, where the focus of the beam must be placed inside the FP diode. For this specific injection lock this was relatively simple since the butterfly package, used to mount the diode, has a pre-installed collimation lens. This lens ensures that the output of the injection locked light is nicely collimated.

The typical attenuation obtained with the isolator was 30 dB, this makes it difficult to completely isolate the child laser's output from the seed light path. Therefore, a small portion of the child laser's output is reflected on the second PBS of the isolator, where it overlaps with the seed light path. This non-isolated light is called the 'back coupling' and it can be used to our advantage when aligning the seed light with the FP diode. By beam walking this light back into the fiber that brings the seed light into the setup (up to a fiber coupling efficiency of ∼50 %), the seed light and back coupled light can be made to overlap. The back coupling of the child laser into this fiber allows us to monitor how well the seed light is coupled into the FP diode. Improving the coupling efficiency, generally allows for a lower power seed light to make the injection lock work. In this project, seed light powers between 1 mW and 2 mW are found to be sufficient to make a stable lock.

After optimizing the back coupling, I use the temperature and current controllers to bring the free running FP diode close to the seed frequency. I first set the diode current to a value where the child laser output power is somewhere between 100 mW and 150 mW. This is easily enough power for the lattice beams and the rest of the light is distributed over other labs, which is another reason why building an injection lock was convenient. To proceed with the initial lock, I monitor the seed *laser* and free running child laser frequencies on the wavemeter and tune the diode temperature until the child laser frequency is 900 MHz higher than the seed laser frequency. The seed light is namely shifted by +900 MHz by the shifting setup described in Sec. 3.2.1, with the AOMs set at their center frequencies. As shown in Fig. 4.1, a small leakage beam

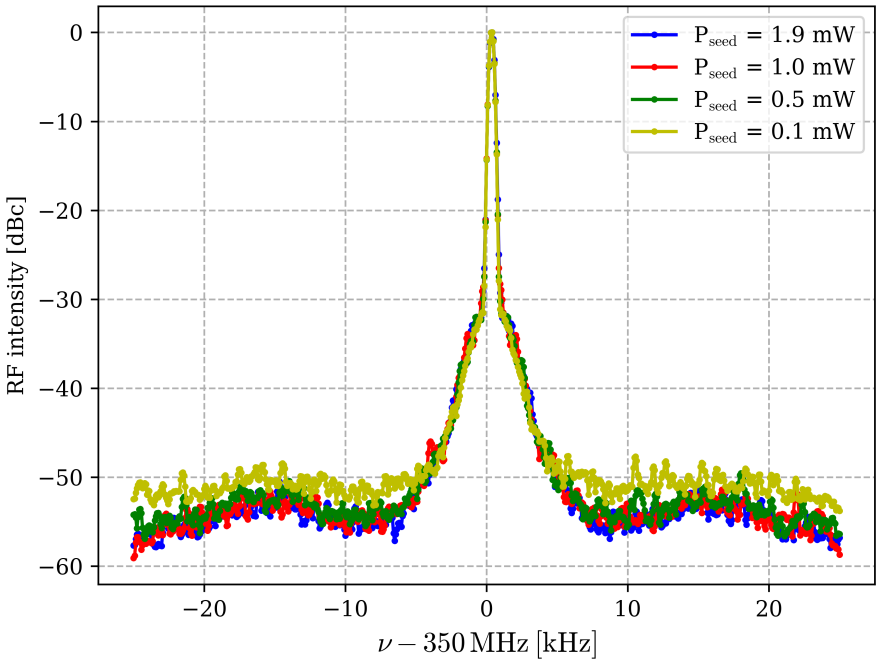


Figure 4.3: Beat note spectrum for different powers of the seed light. The carrier is centered at 350 MHz because the 0^{th} diffraction order of the second pass through the 350 MHz AOM is used for the beat note.

from one of the mirrors is coupled into a Fabry-Pérot cavity. By scanning the length of the FP cavity with a piezo, while measuring the transmission on a photodiode (PD), we can monitor the injection lock. If the cavity transmission shows a single sharp peak, that does not drift in time during the scan, it means that the frequency of the child laser output has a fixed and stable frequency, indicating that it is locked to the seed laser. If the child laser would be running in multi-mode, multiple transmission peaks would appear, indicating that the current of the diode is not yet set right. After setting the FP diode's frequency to the right value on the wavemeter with the temperature controller, I fine tune the lock with the current controller while monitoring the FP cavity transmission. Tuning the current until the child laser is truly lasing on a single mode and maximizing the FP cavity transmission peak. To double check the quality of the lock, I monitor both the 'short'- and long-term stability, which is described in the following sections.

4.2 Beat note

Monitoring the injection lock on a scanning FP cavity only tells us something about the frequency stability of the injection locked light, up to a resolution that is limited by the FP cavity linewidth (∼MHz). It cannot distinguish whether there exists a fixed phase relationship between the seed and the injection locked light. To verify that the child laser is phase-locked to the seed laser, I beat the residual child laser output with the seed light. Specifically, the 0^{th} diffraction order of the second pass through the 350 MHz AOM in the frequency shifting setup is used, see Fig. 3.4. Since the $+1^{\text{st}}$ diffraction order is used as seed light for the injection lock, a beat note should appear at 350 MHz.

Fig. 4.2 shows the setup that overlaps both beams to create a beat note detected by a PDA015A2 photodiode from Thorlabs with a bandwidth of 380 MHz. The photodiode is connected to a *Rohde & Schwarz* FSH8 spectrum analyzer to monitor the beat note spectrum with Hz to kHz resolution. In Fig. 4.3 the beat note spectrum is plotted for different seed light powers. We measured a stable beat note indicating that the child laser is nicely locked to the seed laser. The RF power of the beat note is expressed in dBc (decibel relative to carrier) which compares

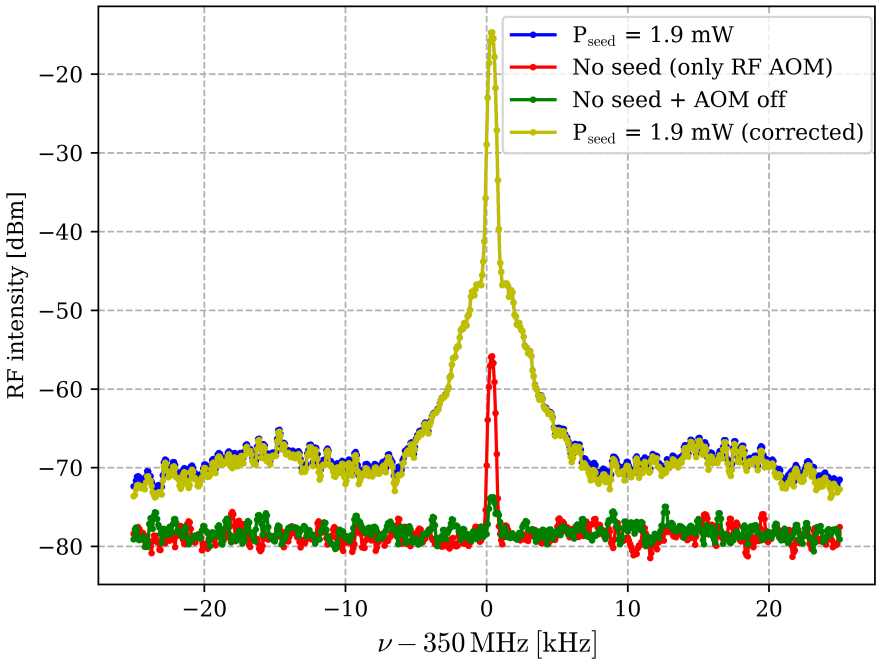


Figure 4.4: Beat note spectrum corrected for acoustic RF noise coming from 350 MHz AOM.

the measured signal to the power of the carrier and allows for better comparison between the four different beat notes. Reducing the seed power down from 2 mW to a few hundred μW did not seem to change or decrease the carrier power of the beat note, indicating a good coupling efficiency of the seed light with the laser diode. Only after reducing the seed light to 0.1 mW or lower, the power of the beat note started to decrease. This is indicated in Fig. 4.3 by a slight increase in the noise floor relative to the carrier.

To confirm that the RF spectrum measured was actually coming from the beat note between the parent and child laser, I also recorded the spectrum while completely blocking the seed light. It can be seen in Fig. 4.4 that an RF tone still appeared at 350 MHz, where the RF power is now plotted in dBm to show the difference in magnitude of the different tones. After also switching off the RF amplifier for the 350 MHz AOM, this peak almost completely disappeared. Indicating that the spectrum analyzer was picking up RF noise coming directly from the AOM, which was likely caused by one of the coax cables that acted as an antenna. When the RF amplifier is turned off, a small amount of RF power still arrives at the AOM. This likely causes the small peak in the green trace of Fig. 4.4 to appear. The yellow trace shows the beat note at 1.9 mW of seed light, corrected for the noise floor and acoustic RF signal from the AOM (blue trace - red trace). The minimal difference with the non-corrected (blue) signal shows that the noise floor and AOM RF noise have negligible influence on the strength of the measured beat note between the child laser and seed laser.

4.3 Long term frequency stability

To check the stability of the injection lock over a longer period, I monitored the seed laser and child laser frequencies on a WS8-30 wavemeter from *HighFinesse* [46]. The wavemeter is referenced to the ECDL of the red (689 nm) laser system, described in Sec. 3.1 and has a frequency resolution of 10 MHz. This means that the long-term stability of the wavemeter is limited by the stability of the red laser.

Note that the seed light used for the long term measurement is directly coming from the parent laser, without any frequency shift in between. The child laser is locked to the seed laser as described in Sec. 4.1. The seed light is first blocked from injecting into the child laser, without

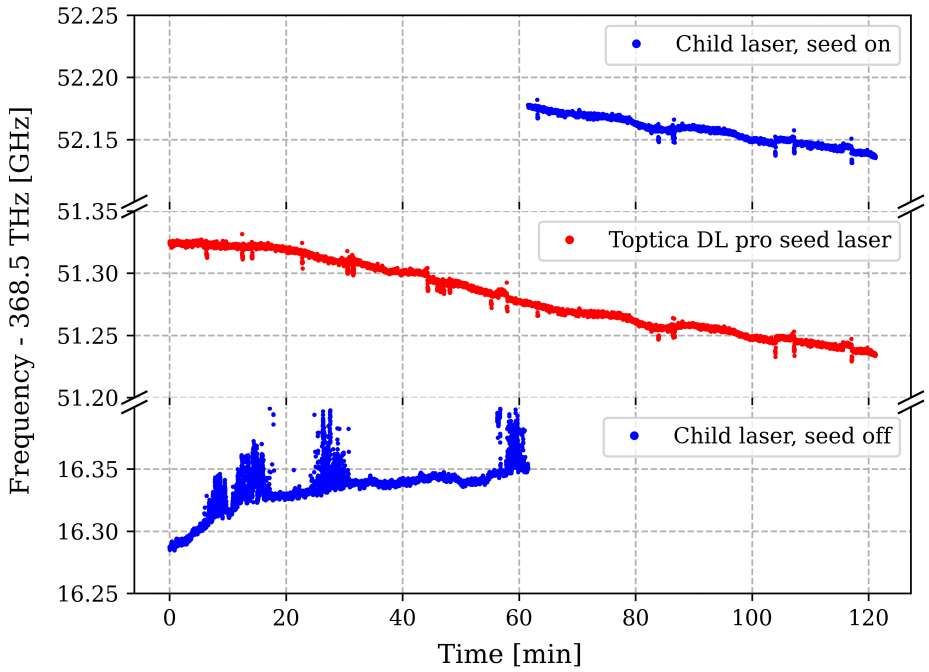


Figure 4.5: Long-term frequency stability measurement of the 813 nm injection lock. The seed light is blocked for the first hour, making the child laser free running. After that the seed light is unblocked and the child laser follows the frequency drift of the free running seed laser. The 900 MHz frequency difference comes from the frequency shifting setup.

changing the diode's temperature or current. This makes the child laser essentially free running, independently from the free-running parent laser. Then the measurement is started and plotted in Fig. 4.5. After an hour I unblock the seed light and the child laser immediately locks to the seed laser, with a 900 MHz frequency difference due to the shifting setup. It can be seen that for the next hour, the child laser nicely follows the ∼50 MHz/h frequency drift of the free-running parent laser, maintaining the relative frequency difference and even following small jumps in the parent laser's frequency.

In practice we found the injection lock to be stable for multiple days, where the limiting factor was coming from instabilities in the parent laser system. Also note that at 60 min in Fig. 4.5, the free-running child laser frequency is only within a few tens of GHz of the seed frequency, which turned out to be enough to make the injection lock work.

Chapter 5

Building the mock system

With control over the power and frequency of the 813 nm lattice and 689 nm probe light, as established in the previous chapter, the next step is to couple two lattice beams and a probe beam into the bowtie cavity.

Because the bowtie cavity in the mHz-experiment's science chamber is positioned at the center of the optical table, working space around it is very limited, making it difficult to build and align the cavity beam optics. The cavity is also mounted vertically (see Fig. 1.3) so the beams must be sent into it vertically as well, which adds an additional layer of difficulty to the alignment.

For this reason, it is useful to copy the dimensions of the science chamber and orientation of the bowtie cavity. This allows us to duplicate the system on a different table, where it is easier to build the optical setup for the cavity beams. For this purpose, I constructed a separate 'mock' system that consists of a small vacuum chamber into which a copy of the bowtie cavity is placed. Because the beams need to be coupled vertically into the cavity, the breadboard containing the optics will be mounted above the science chamber (and therefore also above the mock system's vacuum chamber). A slit in the breadboard and a window in the upper flange of the chamber allow for optical access into the cavity. To accurately replicate the science chamber, the breadboard in the mock system should be positioned at the same height relative to the cavity. The breadboard is therefore supported by four poles that are cut to the right length to match the science chamber's breadboard-cavity distance. To completely match the orientation of the science chamber, the breadboard-cavity alignment is fixed by an adapter plate and two poles with mm-level precision. Once the optical setup is built and aligned to the mock cavity, the breadboard is moved to the science chamber where the beams are realigned to the cavity there.

The mock system uses a copy of the bowtie cavity used in the science chamber, which needed to be constructed by placing the curved mirrors onto the cavity spacer. The process of aligning these mirrors and the initial appearance of transverse modes, is described in the first part of this chapter.

In the second part, an overview is given of the assembly of the vacuum chamber into which the mock cavity is placed.

After that, a description is given of the optical setup that is placed onto the breadboard. The setup contains optics to align two 813 nm beams into the cavity that will form an optical lattice, a 689 nm beam to probe the atoms and a telescope imaging system for fluorescence detection of atoms using 461 nm light. Once atoms arrive into the cavity, this telescope system will allow us to image the position of the atoms inside the dipole guide, onto a camera. The cavity transmissions of the lattice and probe beams are also monitored on this breadboard, by using two Faraday isolators and dichroic mirrors.

Next, a description is given of the cavity lock to the 813 nm laser, using one of the lattice beams. This is done with the Pound-Drever-Hall method described in Sec. 2.3, using a home-built EOM.

Finally, the mock cavity is characterized by performing a ring-down measurement.

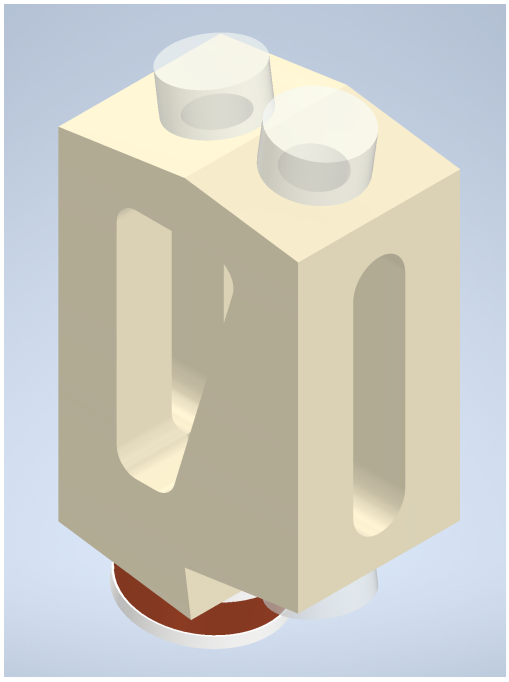


Figure 5.1: 3D drawing of the bowtie cavity used in the experiment. The two mirrors on the left are flat and the mirrors on the right are concave, with a radius of curvature of 500 mm. The piezoelectric actuator stack is composed of two concentrically arranged tubes with different radii, connected via a ceramic ring. The bottom left mirror is glued to the small piezo tube and the large piezo tube is glued to the spacer, all other mirrors are directly glued to the spacer.

5.1 Bowtie cavity construction

This section describes the design and assembly of the bowtie cavity used in the mock system, which mimics the bowtie cavity in the experiment's science chamber.

The bowtie cavity used in this experiment (in both the science chamber and mock system) consists of four mirrors from *Laseroptik* and a Zerodur spacer, see Fig. 5.1. The mirrors are angled at 8.35° from the horizontal plane, where the reflective surfaces of the left hand mirrors are flat and the right hand mirrors are concave, with a radius of curvature of R = 500 mm. All four mirrors are AR coated on the outside and HR coated on the inside, both for 698 nm and 813 nm. The length of the cavity can be changed with a piezoelectric actuator, glued to the bottom left flat mirror. A more in depth explanation about piezoelectric actuators is given in Sec. 5.1.1.

In order to form a cavity out of the four mirrors, light needs to be able to resonantly travel between these mirrors. This means that the phase accumulation of a light wave must be an integer multiple of 2π after each round-trip.

The starting point was a spacer with only the two flat mirrors and piezo stack glued to it. Both concave mirrors still needed to be added in order to form a cavity. To do this, a laser beam was centered on both flat mirror surfaces and the position of the concave mirrors transverse to the cavity axis was scanned with μm precision, using two translation stages. The concave mirrors were pressed to the spacer and held in place by pogo pins on the translation stage's arm, see Fig. 5.2. With the rotation knobs on the translation stages, the position of both mirrors was adjusted to μm-level precision until higher order TEM modes started to appear on the camera that monitored the cavity's transmission. By making slight adjustments to the mirror positions and incoupling of the beam, I was able to observe some of the transverse modes presented in Fig. 5.3. A final beam walking to optimize the incoupling made it possible to make the Gaussian TEM_{00} mode most dominantly coupled into the cavity. This mode results in a uniform field distribution with the highest intensity, making it suitable for creating an optical lattice. By scanning the cavity length across the (Gaussian) resonance and monitoring the transmission and reflection from the incoupling cavity mirror, the cavity coupling efficiency was further optimized.

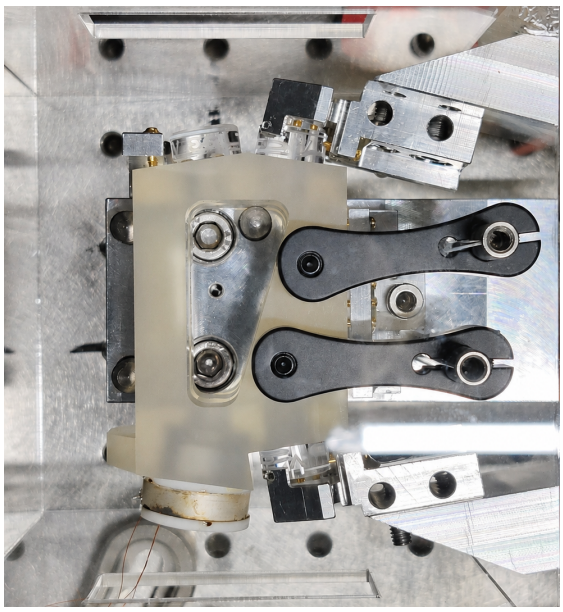


Figure 5.2: Assembly of the mock bowtie cavity. The two curved mirrors are pressed against the spacer by two translation stages, resting on pogo pins to align their angle with the spacer surface. μm-screws on the translation stages allow for precise positioning of each mirror along the two axes perpendicular to the cavity axis, until a cavity is formed.

I then glued both mirrors to the spacer using Torr Seal TS10 vacuum epoxy, while trying to maintain a constant cavity coupling efficiency. After 72 hours of curing the glue, the translation stages could be removed and the cavity was ready to be placed inside the vacuum chamber.

5.1.1 Piezoelectric actuators

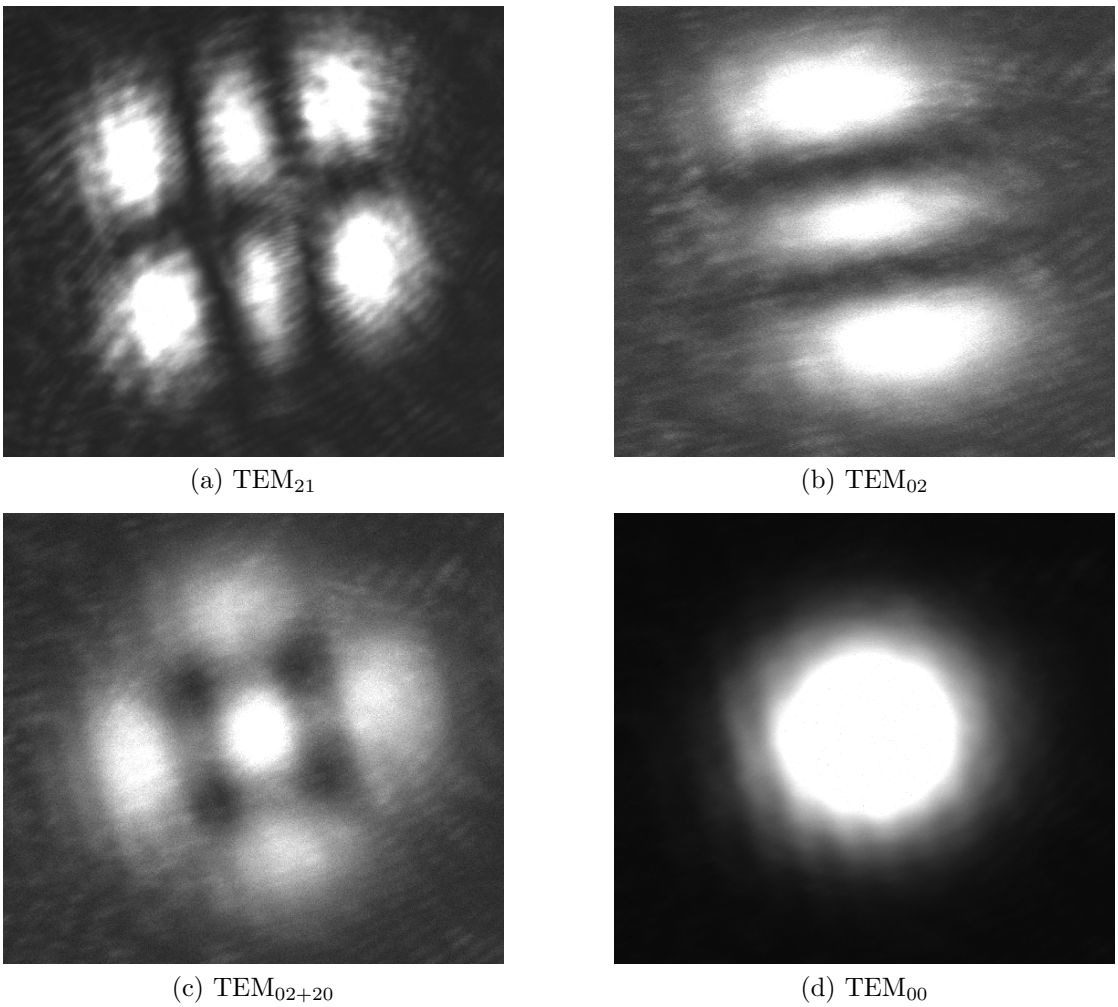
As mentioned above, the length of the cavity can be changed with a piezoelectric actuator (piezo). This is a ring-shaped tube made from a material that exhibits the piezoelectric effect. By applying electric voltages to this kind of material, they can physically deform. Conversely, they also generate an electric charge in response to applied mechanical stress. The axial contraction ΔL_{axial} of a piezoelectric tube as a function of the applied voltage U is estimated by [47]

$$\Delta L_{axial} \approx d_{31} L \frac{U}{d}. \tag{5.1}$$

Where d_{31} is the strain coefficient of the material, L is the unperturbed length of the tube and d is the thickness of the tube.

For this cavity, two different PT130 piezo tubes from *Physik Instrumente* are used, a small one with a diameter of 10 mm and a bigger one with a diameter of 20 mm. They are both concentrically glued to a ceramic ring, the smaller one on the inside and the bigger one on the outside. The bottom left flat mirror is directly glued to the other side of the small piezo tube and the big piezo tube is glued to the spacer with another ceramic ring in between. There are multiple reasons why two piezo tubes are used. The most important reason is redundancy. Because the cavity will be placed in a vacuum chamber, it becomes difficult to repair if something breaks since that would require breaking vacuum. Second, because of the way the piezo tubes are glued to the ceramic rings and flat mirror, both piezos will move the mirror in opposite directions when their axial length changes. If the larger piezo contracts, the optical path length of the cavity becomes smaller, while contraction of the small piezo causes an increase in the optical path length of the cavity. This means that thermal fluctuations, which affect the length of both piezos, nearly cancel out.

The original piezo tubes had a length of 30 mm and were cut in six pieces so they could be used on other cavities as well. But this also decreased the maximum axial contraction of the piezos by a factor of six, which is clear from Eq. 5.1. The theoretical maximum axial contraction,



(a) TEM_{21} (b) TEM_{02}

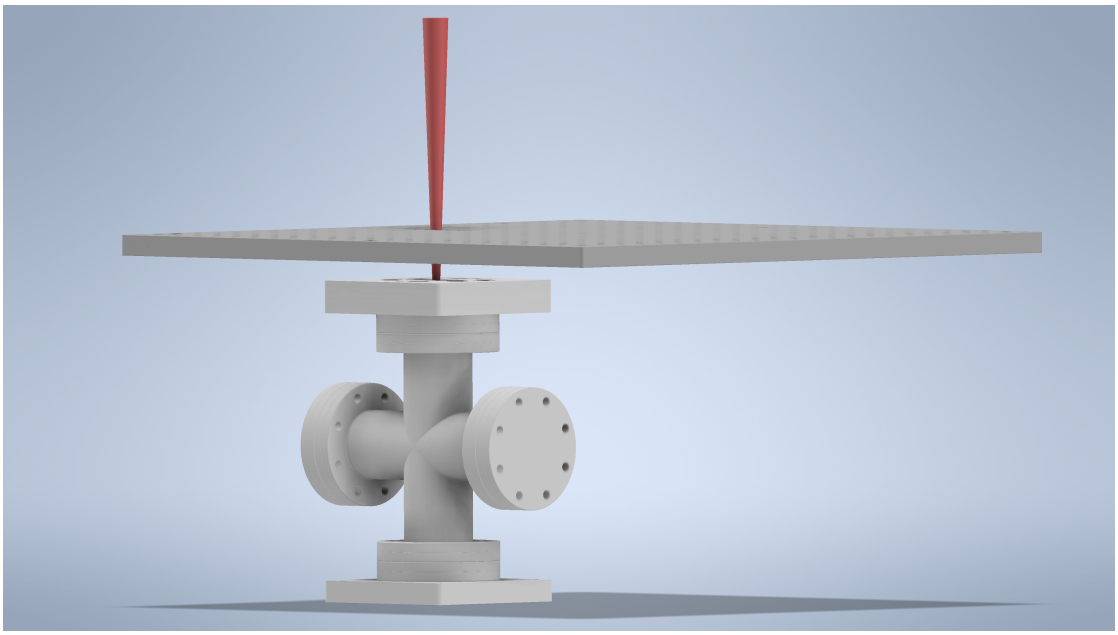
(c) TEM_{02+20} (d) TEM_{00}

Figure 5.3: Transverse electromagnetic modes observed during the alignment of the bowtie cavity. The incoupling is maximized for the Gaussian TEM_{00} mode.

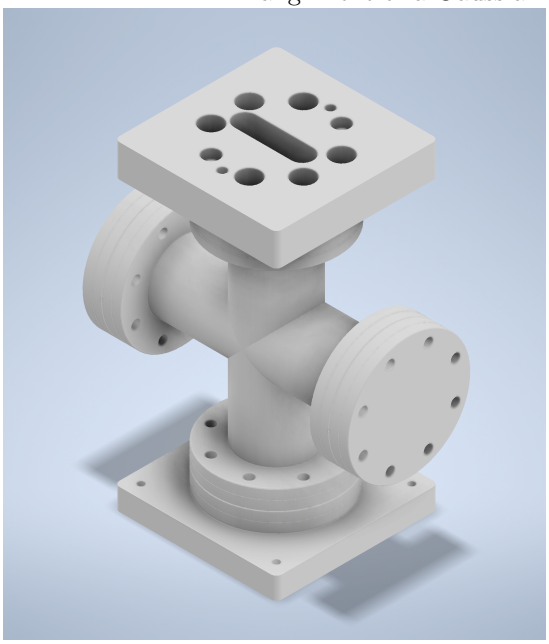
determined from the datasheet, for the small and big piezos is therefore 1.5 μm at 500 V and 1000 V respectively. This difference in required voltage is due to the bigger piezo also being twice as thick as the small piezo. To amplify the voltages sent to the piezos, we use a TD250 PiezoDrive that has a 50 V/V gain and a maximum output of 500 V. The maximum contraction reachable with the big piezo is therefore 750 nm. This is not enough to scan one full FSR with the 813 nm light, so the small piezo was primarily used for that. As will be shown later on in Sec. 5.4, I also used the redundancy of having two differently behaving piezos to make the cavity lock to the 813 nm lattice light.

5.2 Vacuum chamber

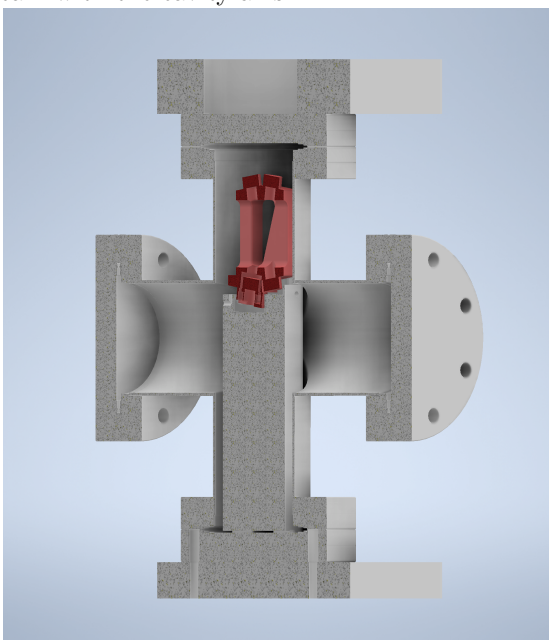
After finishing building the mock bowtie cavity, changes in airflow and thermal fluctuations can still create disturbances in the optical path length of the light inside the cavity. It is therefore important to place the cavity inside a vacuum chamber, to create a sufficiently stable environment for the alignment and characterization of the cavity. A small vacuum chamber made by the Technology Center is used for this. The chamber consists of a holder for the cavity, an AR coated window in the upper flange for optical access into the cavity, a flange with four feed-through connections to apply voltages to the piezos and a valve. The dimensions of this vacuum chamber are made to mimic or 'mock' the dimensions of the science chamber on the experiment. Specifically, the position of the cavity relative to the breadboard containing the optics must be the same on this mock system as on the experiment itself. Because this will allow us to move the breadboard with the optical setup, from the mock system to the science chamber later on,



(a) Mock system with breadboard placement above the vacuum chamber and vertical alignment of a Gaussian beam with the cavity axis.



(b) Top view of vacuum chamber with adapter plate screwed onto the top flange. The slit allows for optical axis into the chamber and cavity, the two small holes are used for placing the poles to align the breadboard.



(c) Cut-through image of bowtie cavity placement inside the vacuum chamber.

Figure 5.4: 3D drawings of the vacuum chamber used in the mock system.

without completely losing the alignment of the beams to the cavity. In order to achieve this, the breadboard-cavity alignment is fixed by two poles and an adapter plate. The adapter plate is screwed onto the top flange of the vacuum chamber and has a slit through which light can be sent into the cavity. The two poles are fixed into the adapter plate and need to align with (and go through) two holes in the breadboard. This way, the alignment of the breadboard relative to the adapter plate is fixed by the two poles with sub-mm precision. The adapter plate then fixes the alignment of the two poles relative to the cavity with a few mm precision, such that the placement of the breadboard relative to the cavity is also fixed with mm-level precision. The 3D drawings of the mock system's vacuum chamber are given in Fig. 5.4, together with the breadboard and vertical orientation of a beam aligned with the cavity axis. Once the breadboard is be moved to the experiment, the two poles are also fixed onto the science chamber, where they have the same position relative to the cavity as on the mock system. By aligning the holes in the breadboard with these poles again, the alignment to the science chamber cavity should not be too far off since the beams have been aligned on the mock system's cavity before.

Inside the vacuum chamber, the cavity spacer rests on three ball bearings that are glued to the holder with Torr Seal TS10 vacuum epoxy. To fix the cavity in place, the spacer is pressed and clamped to one side of the holder by a screw. The in- and outside of both piezo tubes are connected to the feed through flange by Kapton insulated wires that are directly soldered onto the piezo tubes. These types of wires are used because of their strong insulating capabilities and low coupling to external vibrations. Before closing off the chamber, the electrical capacitances of both piezos were measured at 6.8 nF for the small (inner) piezo and 6.6 nF for the large (outer) piezo. These values are within the $\pm 20\,\%$ tolerance quoted by the manufacturer. After that, all flanges were closed off and the chamber was pumped down to an inside pressure of $\sim 8 \times 10^{-3}$ mBar, using an oil pump. Then the valve was closed and we turned off the pump. To find out if the vacuum was properly sealed, the valve was opened again after about 2 hours to check that air was flowing into the chamber. Finally, the chamber was pumped down again to the same inside pressure as before.

Now that we established a low vacuum that provides a stable environment for the mock cavity, the breadboard was placed above the vacuum chamber. This breadboard contains all the optics for both lattice beams and the probe beam.

5.3 Optical setup

The breadboard with all the optics above the vacuum chamber, is placed onto four large 2 inch poles. They are cut to the right length such that the vertical distance from the breadboard to the mock cavity is the same as the vertical distance to the cavity in the science chamber. This is important since we focus the lattice and probe beams into the cavity to optimize mode matching. If now the height of the breadboard relative to the cavity is different on both systems, the beams will not be focused onto the cavity mode waist any more after moving the breadboard to the science chamber, which could decrease the cavity coupling efficiency. Both the 689 nm and 813 nm cavity mode, have a Rayleigh length of $z_R \approx 135$ mm. This means that we have a few cm of margin when setting up the height of the breadboard.

An overview of the optical setup, together with the bowtie cavity, is given in Fig. 5.5. On the top left, 813 nm light from the injection lock setup described in Sec. 4.1 enters the setup. This light is split up into two paths using a $\lambda/2$-plate and PBS. This creates two 'lattice' beams, that interfere inside the cavity to form an optical lattice, one of which I will call 'X' and the other one 'Y'. Both beams pass through an 80 MHz AOM that can be used for power stabilization in the future. Since the $+1^{\text{st}}$ order on both AOMs is used, the frequency of the light of both lattice beams is also shifted by +80 MHz. By offsetting the RF signal sent to the AOM for lattice beam Y from its center frequency, a movable lattice inside the cavity can be created. Alternatively, the RF signal sent to the AOM for lattice beam X can also be shifted from its center frequency. It is however important that the frequency at which AOM X is driven, is always *higher* than the frequency at which AOM Y is driven. This will ensure that the optical lattice is moving vertically upward between the two flat cavity mirrors. The frequency difference $\Delta\nu$ between both AOMs is directly proportional to the velocity of the optical lattice, which is given by Eq. 2.30. Where $\Delta\nu = \nu_x - \nu_y > 0$. A lattice velocity of 1 cm/s will therefore require a relative frequency shift of $\Delta\nu = 24.6$ kHz.

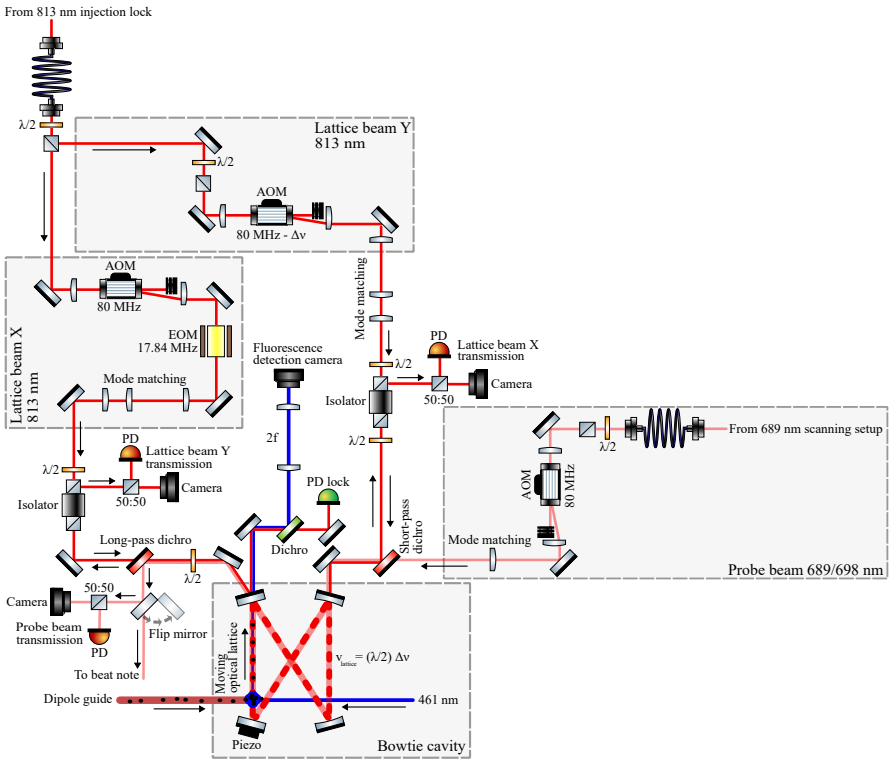


Figure 5.5: Schematic overview of the optical setup placed on the breadboard above the vacuum chamber.

After the AOM, lattice beam X propagates through a free-space 'electro-optic modulator' (EOM) that is modulated at 17.84 MHz. The EOM induces a phase modulation on the incoming light. In the spectral domain, this phase modulation translates to the creation of sidebands that appear at ±17.84 MHz from the carrier frequency. This modulation is necessary in order to lock the cavity to the light from lattice beam X, using the 'PDH-technique' which will be explained in Sec. 5.4.

After the EOM, a 'mode matching' system consisting of three lenses in a cage system is used to focus lattice beam X into the cavity. By overlapping the beam's radius with the cavity mode structure presented in Fig. 2.8, the light's coupling efficiency into the cavity can be optimized. The same kind of mode matching happens for lattice beam Y, after the AOM there.

Lattice beam X is diagonally coupled into the cavity via the top left cavity mirror and lattice beam Y is vertically coupled into the cavity via the top right cavity mirror. As a result, the cavity transmission of lattice beam X exactly overlaps with the incoupling path of lattice beam Y. Similarly, the cavity transmission of lattice beam Y exactly overlaps with the incoupling path of lattice beam X. To filter out the cavity transmissions from the incoupling paths, simply using a PBS and $\lambda/4$-plate would not work, because of the reciprocal behavior of a $\lambda/4$-plate (provided that the resulting circularly polarized light of both beams has the same handedness in the lab frame). This means that the effect of a $\lambda/4$-plate on the light's polarization is undone when the light propagates through it a second time in the opposite direction, turning the circularly polarized cavity transmission of one beam back into linearly polarized light aligned with the incoupling path of the other beam. This prevents the two from being separated. In addition, a $\lambda/4$-plate creates circularly polarized light inside the cavity, resulting in (unwanted) polarization mode dependent cavity resonances, as described in Sec. 2.2.3. Both problems are solved by instead using a Faraday isolator and a $\lambda/2$-plate, which exploit the non-reciprocal behavior of the isolator. A magnetic field rotates the light's linear polarization in the same absolute direction, regardless of its propagation direction. This results in linearly polarized light being sent into the cavity in the forward direction, while the polarization of the reverse propagating cavity transmission of the other beam, is rotated further rather than back. For both beams to interfere

and create an optical lattice, both beams must be linearly polarized in the S- or P-plane of the cavity. This also prevents the polarization mode dependent resonances from appearing. The polarization angle of both beams can be further adjusted using the $\lambda/2$-plates positioned after the isolators. The cavity transmission of both beams reflects from each isolator's PBS and is split up using a 50:50 beam splitter. The mode profiles are monitored using two *Basler Ace 2 Pro* cameras and the transmitted power by two Thorlabs PDA8A2 photodiodes.

On the other side of the breadboard, 689 nm light from the frequency shifting setup described in Sec. 3.1.1 enters the setup. This beam is also sent through an 80 MHz AOM, using the $+1^{\text{st}}$ order. This will allow us to probe the atoms by switching on and off the RF signal power sent to the AOM. Due to space restrictions, only one lens is used for matching the probe beam radius to the cavity mode. The probe beam is coupled into the cavity via the same top right mirror as the lattice beam Y. A dichroic 750 nm short-pass mirror from Edmund Optics is used to overlap the probe beam with lattice beam Y. The cavity transmission of the probe beam overlaps with the incoupling path of lattice beam X. A dichroic 760 nm long-pass mirror from Thorlabs is therefore used to filter out the probe light. This cavity transmission is again split up using a 50:50 beam splitter, where the mode profile is monitored on a third identical Basler camera as the lattice beams. Because very low power probe light will be used to probe the atoms inside the cavity, the transmission of the probe beam will presumably be very faint. Therefore, a Thorlabs APD130A/M avalanche photodiode is used to monitor the transmitted power of the probe beam. Additionally, the flip mirror just before monitoring the probe beam's transmission can be used to redirect light coming from atoms to a different setup. On this setup a beat note could be made between the light coming from the atoms and a stable reference, which will be useful for future projects.

Once atoms can be transferred from the red MOT to the cavity via the dipole guide, it becomes important to align the dipole guide with the cavity mode. To do this, it is proposed to use fluorescence detection of the atoms inside the dipole guide, using the 461 nm blue light (targeting the ${}^1S_0 \rightarrow {}^1P_1$ transition). This blue beam will horizontally traverse the cavity at the height of the reservoir trap. The fluorescence from the atoms is coupled out of the cavity via the top left mirror and will therefore overlap with the reflection of lattice beam X. To filter out the blue light, a dichroic 560 nm long-pass mirror from Thorlabs is used. The blue light reflected from the dichroic mirror will pass through a 2f telescope system to image the dipole guide position onto the same Basler camera used before. This fluorescence detection setup is placed on the same breadboard as the lattice and probe beams.

After coupling all beams into the cavity, the next step is to lock the cavity to the light from lattice beam X which will be described in the next section.

5.4 Pound-Drever-Hall lock

As mentioned before, the cavity (length) is locked to lattice beam X using the 'Pound-Drever-Hall' technique. For this method, the beam's reflection from the top left cavity mirror needs to be used. As shown in Fig. 5.5, the reflection passes through the dichroic mirror that filters out the blue fluorescence light. The reflected light is then monitored on a Thorlabs PDA10A2 photodiode. The theory and working principle of PDH-locking is fully described in Sec. 2.3, so I will primarily focus on the hardware used to realize this specific lock here.

To generate sidebands in the spectral domain of the incoming light, a home-built electro-optic modulator (EOM) is used. Each EOM consists of an LC-circuit and a birefringent crystal, see Fig. 5.6. An LC-circuit consists of an inductor and a capacitor, acting as an electrical resonator, storing energy alternately in the inductor's magnetic field and the capacitor's electric field at the circuit's resonance frequency [48].

The specific EOM used consists of a 14 μH inductor, 122 pF capacitor and a variable capacitor to tune the resonance frequency of the LC-circuit. The copper plate and outer casing of the EOM also act as a capacitor, where the gap between the plates is filled by the crystal. When the LC-circuit is driven at its natural resonant frequency using a function generator, the oscillating electric field through the crystal will create a periodic modulation of the crystal's refractive index. This modulation of the refractive index results in a phase modulation of the incoming light, which translates to the appearance of sidebands next to the carrier in the light's spectral domain. Since the crystal is made from a birefringent material, it is important to align the

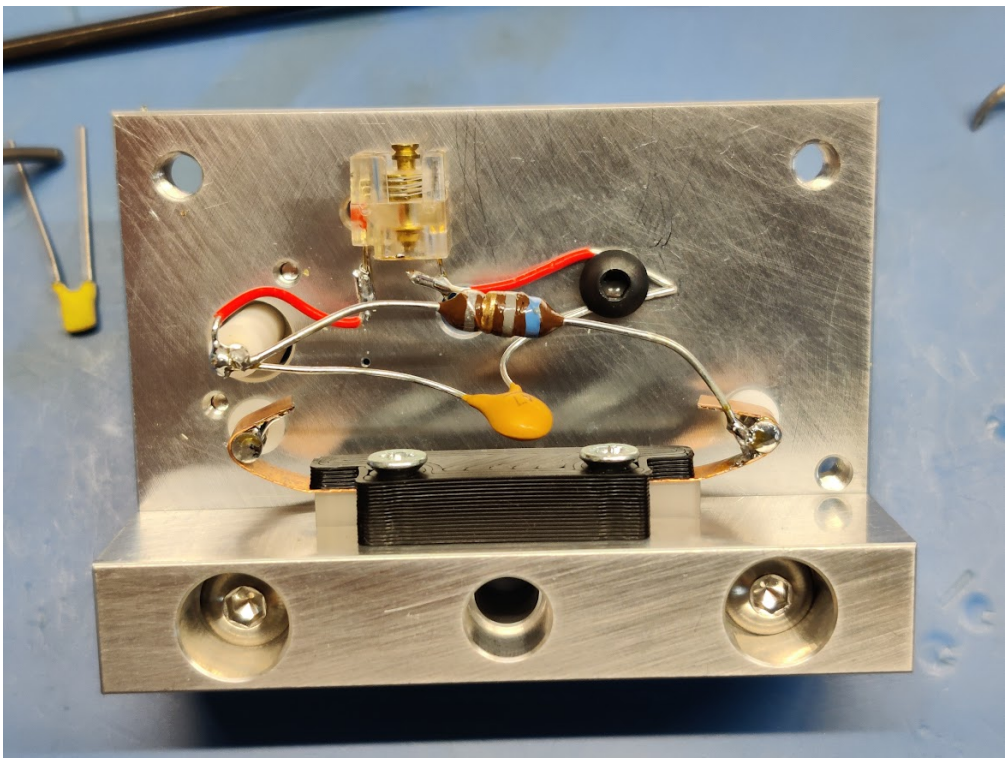


Figure 5.6: LC-circuit inside the home-built free space EOM used for the PDH-lock. The crystal is placed between a copper plate and the outer casing, that act as a capacitor.

polarization of the incoming light with one of the optic axes of the crystal. For the specific crystal used here, I found out that sidebands only appeared when the polarization was aligned with the horizontal optic axis of the crystal. In total I made and characterized three EOMs, the results of the characterizations are presented in Fig. 5.7. The dip in each spectrum denotes how much power is transferred from the carrier into the sidebands by the EOM. For this specific setup, 'EOM 1L' with a resonance frequency of 17.84 MHz is used.

The spectrum of the incoming light from lattice beam X thus consists of three distinct peaks: a large carrier at ω_c and two smaller first-order sidebands at $\omega_c \pm \Omega$, where Ω is the 17.84 MHz modulation frequency of the EOM. This light is captured by the photodiode and sent through a 22 MHz low-pass filter from Mini-Circuits and a 10 MHz high-pass filter from Thorlabs. This creates an effective 10-22 MHz band-pass to filter out higher order frequencies (like the 35.68 MHz beat note between the two sidebands), while maintaining the 17.84 MHz beat note signal between the carrier and each sideband. This isolated signal is then mixed with a local oscillator (LO) that has the same 17.84 MHz frequency, but with a tunable phase. In practice, this is realized by using both channels of a function generator, one channel feeds a signal to the EOM and the other channel is used as a LO. The relative phase difference between these signals is created by tuning the starting phase on one of the two channels. A 1-100 MHz BW phase detector from Mini-Circuits is used to mix both signals, the output of the mixer is passed through a 1.9 MHz low-pass filter from Mini-Circuits to isolate the DC-part of the signal. To monitor how the resulting error signal (used for locking the cavity) looks like, we scan the length of the cavity across a resonance by ramping up and down the voltage sent to the small piezo at a frequency of 20 Hz. Remember from Eq. 2.17 that scanning the length of a cavity is equivalent to scanning the frequency of the incoming light. The obtained error signal, together with the cavity transmission of lattice beam X, is plotted in Fig. 5.8. The data is centered on the carrier frequency ν_0, the error signal is fitted to Eq. 2.49 and the cavity transmission is fitted to a triple Lorentzian. The error signal has a steep linear slope of 1.60×10^{-3} mV/Hz near the cavity resonance ν_0, which translates to a linear frequency response of the cavity of 620 Hz/mV.

Now that we have obtained an error signal, we can use it to lock the cavity to the free-running 813 nm laser. As mentioned before in Sec. 5.1.1, the maximum contraction of the large piezo

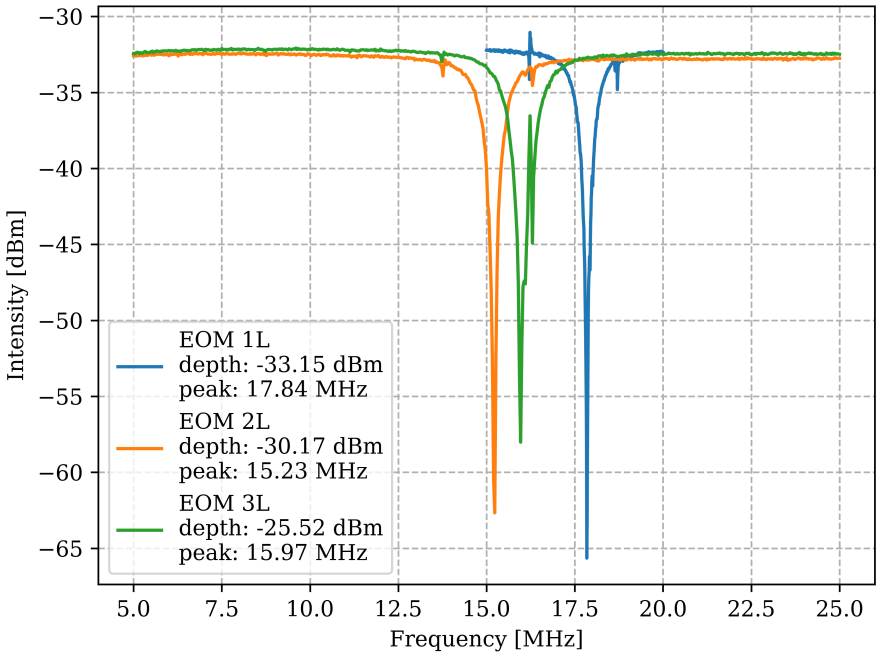


Figure 5.7: Transmission spectra of the LC-circuits used for the three different home-built EOMs.

tube (that is reachable with the available 500 V) is not sufficient to scan a full FSR of the cavity. We therefore apply a DC voltage to the small piezo using a function generator and manually scan the offset until the cavity length is brought close to the resonance frequency of the carrier. Since this places us on the linear part of the error signal, we can use a *Proportional-Integral-Derivative* (PID)-loop to keep the cavity on resonance.

Initially, a RedPitaya was used as a PID controller, which had a limited output range of ±1 V. As mentioned in Sec. 5.1.1, the piezo tubes required voltages on the order of a few hundred volts to operate, so this output range proved insufficient for establishing a stable, long-term lock against the frequency drift of the free-running 813 nm laser. We therefore switched to an analogue PID-controller (AnaPID), modified by the Technology Center. This controller has an output range of ±10 V and a control loop bandwidth of DC-100 kHz [49].

The error signal in Fig. 5.8 is centered around 0 mV which, on the frequency axis, corresponds to the peak of the carrier transmission. We therefore place the setpoint of the control loop around 0 mV, such that the cavity will be locked to the peak of the carrier transmission. Small deviations on the linear slope from this resonance position, caused by fluctuations in the laser's frequency or thermal fluctuations in the cavity, will shift the measured error signal voltage away from the setpoint. The difference between the measured value of the error signal and the setpoint, is called the *error value* e(t). Based on the value of e(t), a control voltage is applied to correct the cavity length for these fluctuations [50]. Since the DC offset was already applied to the small piezo, it was easiest to implement the PID-loop correction voltages on the large piezo. Additionally, since the large piezo's walls are twice as thick as those of the small piezo, its contraction in response to a given voltage is only half that of the small piezo tube. Unfortunately, this did not prevent the lock from ramping up and down across the setpoint, instead of locking to the peak of the cavity resonance.

To minimize the ramping, I tried to reduce the gain of the PID output in response to the measured error e(t). I first did this rigorously, by omitting the high-voltage amplifier (the previously mentioned TD250 PiezoDrive with a 50 V/V gain) between the PID-controller and the large piezo. This however placed us in the opposite operating regime, where the ±10 V output range of the PID controller proved insufficient to drive the piezo tube through the displacement range required to lock the cavity. I therefore kept using the high voltage amplifier but tried

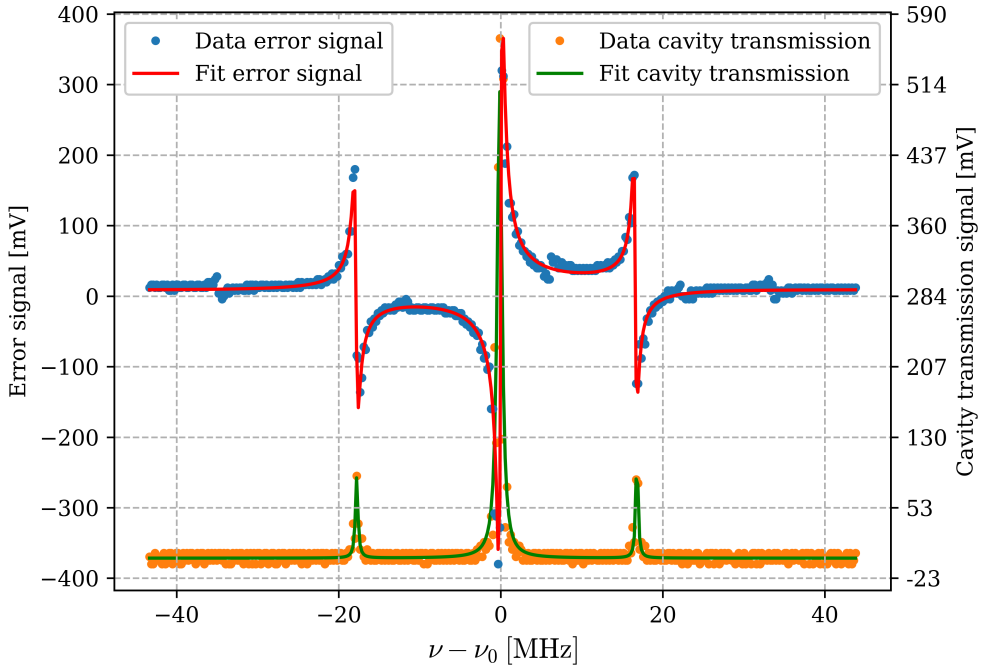


Figure 5.8: Obtained Pound-Drever-Hall error signal and cavity transmission spectrum while scanning the bowtie cavity length. Both graphs are centered around a cavity resonance for the 813 nm light of lattice beam X.

to reduce the steepness of the slope in the linear region of the error signal. A shallower slope reduces the measured error e(t) in response to a given frequency deviation, thereby reducing the corrective voltage applied by the PID controller. The slope is quantified by the frequency discriminant D which can be defined from Eq. 2.54 and is given by [39]

$$D \equiv \frac{8\sqrt{P_c P_s}}{\delta\nu_{cav}}. \tag{5.2}$$

Where I used that $\delta\omega = 2\pi \times \delta f$, for the frequency deviation from a resonance and $\delta\nu_{cav}$ is the cavity linewidth. This expression shows that we could change the steepness of the slope by tuning how much power is transferred from the carrier (P_c) into the sidebands (P_s). The transmission spectrum obtained in Fig. 5.8 was obtained with a maximum modulation depth of the EOM and results in a sideband-to-carrier ratio of $P_s/P_c \approx 16\,\%$. Even reducing this ratio to approximately 1 % did unfortunately not make the slope shallow enough to eliminate the ramping of the cavity across a resonance when the PID loop was active.

In the end, I decided to stick with the maximum modulation depth of the EOM, since this created the largest peak-to-peak error signal. To reduce the slope steepness more drastically, I switched to a 10 kHz low-pass filter from Thorlabs on the output of the mixer (rather than the 1.9 MHz used before). The obtained error signal is given in Fig. 5.9, where the error signal traces in both figures are obtained by linearly scanning the cavity length up and down across a resonance at 20 Hz. Using the 10 kHz low-pass filter therefore initially distorted the shape of the error signal. This was due to the scan going too fast over a resonance for the 10 kHz filter, causing rapid changes in the error signal to be suppressed which flattened down the sharp edges of the trace. To resolve a trace that resembles something closer to the actual shape of the error signal, we reduced the peak-to-peak amplitude of the cavity length scan by a factor of five while maintaining a scan frequency of 20 Hz. This meant the scan had more time to go over a resonance, resulting in less rapid changes in the error signal that are not suppressed by the 10 kHz low-pass filter.

In Fig. 5.9, the peak of the carrier transmission does not perfectly coincide anymore with the

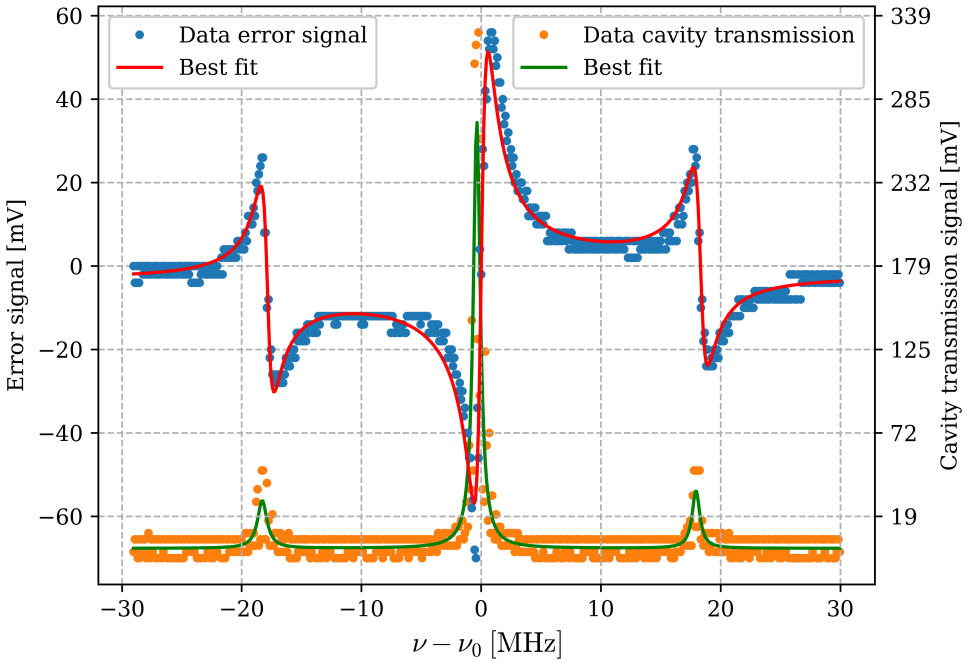


Figure 5.9: Pound–Drever–Hall error signal obtained using a 10 kHz low-pass filter at the mixer output, rather than the standard 1.9 MHz filter. The increased frequency filtering reduces the slope of the linear region, which lowers the gain of the PID controller and yields a more stable lock.

zero crossing of the error signal. Instead, it is centered around the bottom half of the linear slope which has a gradient of 1.02×10^{-4} mV/Hz, which translates to a linear frequency response of the cavity of 9820 Hz/mV. This means that the resonance frequency of the cavity (or frequency of the light) needs to shift by roughly 9.8 kHz in order for the measured error signal to shift by 1 mV, compared to only 620 Hz for the error signal obtained with the 1.9 MHz low-pass filter. The amount of control voltage output from the AnaPID-controller depends on the measured shift of the error signal voltage compared to the setpoint. For an equal frequency shift, the 10 kHz 'shallow slope' error signal will result in a weaker response of the controller output compared to the 1.9 MHz 'steep slope' error signal. This weaker response improved the lock by minimizing the ramp across the resonance as best as possible.

To conclude, a schematic overview of the cavity locking system is given in Fig. 5.10. The DC voltage applied to the small piezo is passed through a 1 kHz low-pass filter to filter out any high frequency noise from the function generator. Since this mock cavity will not be used in the actual experiment, I will give a more detailed overview about the quality of the science chamber cavity lock in Sec. 6.1. The signal-to-noise ratio of the error signal, the theoretically achievable lock stability and measured lock stability are all mentioned there. Additionally, a long term measurement of the experiment's cavity lock will be presented.

5.5 Mock cavity characterization

By using the lock scheme presented in Fig. 5.10, it is possible to create a lock that is stable enough to perform a characterization measurement of the cavity. We would like to know the cavity's linewidth and finesse for both the 813 nm lattice light, as well as for the 689 nm probe light. From the obtained values it is then possible to determine the expected trap depth of the optical lattice and the amount of optical power needed to apply π (or $\pi/2$)-pulses with the probe light.

In practice, this cavity lock can be maintained for several hours. This is enough to perform

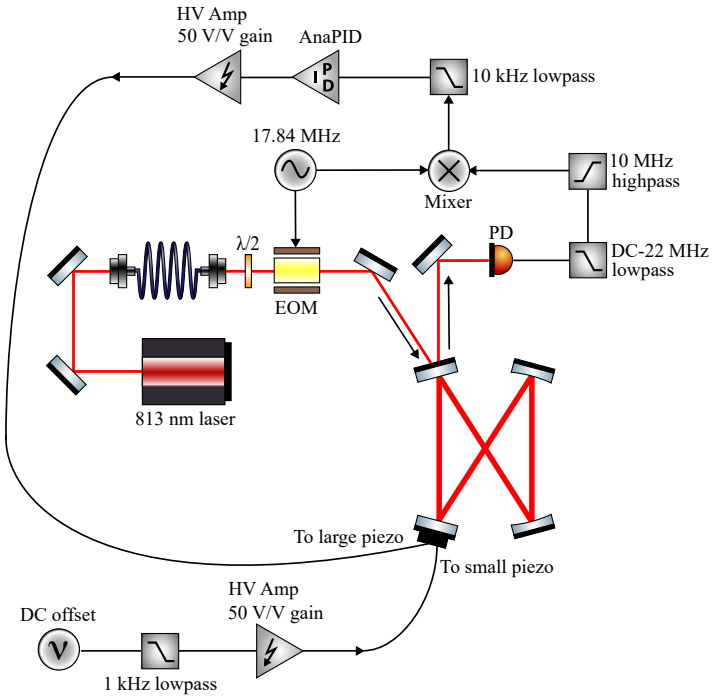


Figure 5.10: Schematic overview of the hardware used to lock the bowtie cavity to the 813 nm laser.

ring-down measurements to characterize the cavity. By rapidly switching off the resonant light coupled into the cavity and measuring the amount of light leaking out of a cavity mirror over time, we can measure the exponential decay of the field inside the cavity. Since the Fourier transform of an exponential decay is a Lorentzian function and the longitudinal cavity mode is approximated by a Lorentzian, we can directly calculate the FWHM of the Lorentzian (i.e. the cavity linewidth) from the measured decay time τ by

$$\Delta\nu_{cav} = \frac{1}{2\pi\tau}. \tag{5.3}$$

Where $\Delta\nu_{cav}$ is the cavity linewidth and τ is the 1/e decay time of the measured *intensity*. Note that the Fourier transform is performed on the exponential decay of the electric field, which decays at half the rate of the intensity.

Rapidly switching on and off the light coupled into the cavity is done with the AOM of lattice beam X and a ZASWA-2-50DR+ switch from Mini-Circuits. Before the 80 MHz signal for the AOM is sent to the RF amplifier, it passes through this switch together with a square wave provided by a function generator. The square wave is converted to a TTL signal where low voltage means 'on' and high voltage means 'off.' This way, the RF signal to the AOM can be turned on and off. Since we use the $+1^{\text{st}}$ diffracted order of this AOM to couple light into the cavity, the power of the light in this order can also be turned on and off. It is important that the frequency of the square wave is significantly lower than the estimated decay rate of the cavity mode, such that we allow the cavity to fully deplete from all captured photons, but also high enough for the PID loop to not notice the error signal disappearing for a short amount of time. Based on a finesse measurement of 7000 for the *science chamber* ring cavity (using 689 nm light), reported in [17], the expected cavity linewidth $\Delta\nu_{cav} = \frac{FSR}{\mathcal{F}} \approx 210\,\text{kHz}$, with $FSR = 1.47\,\text{GHz}$. Using the convention for the decay rate $\kappa = 1/\tau = 2\pi \times \Delta\nu_{cav}$ we expect a cavity decay rate of roughly $1.3 \times 10^6\,\text{rad}\,\text{s}^{-1}$. The square wave frequency must therefore be lower than 1 MHz but also higher than 10 kHz such that the fast switching is filtered out by the 10 kHz low-pass filter, through which the error signal passes. In practice I found a switching frequency between 10 and 100 kHz to be sufficient for performing a ring-down measurement. The decay of the field inside the cavity is measured by monitoring the cavity transmission of a PDA8A2 photodiode from Thorlabs, which has a bandwidth of 50 MHz. To verify that the measured cavity decay

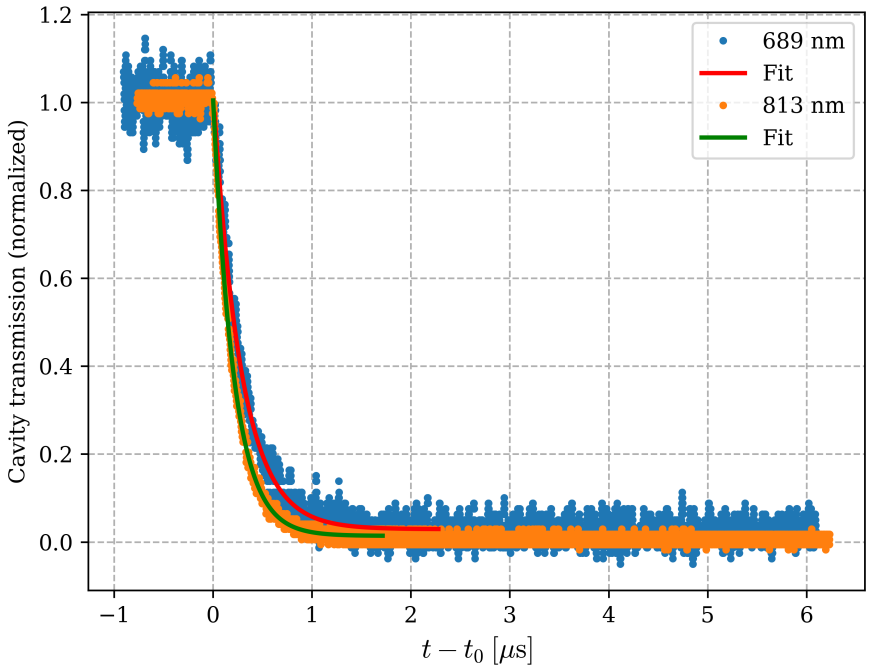


Figure 5.11: Example ring-down measurement of the mock bowtie cavity. The 813 nm light is found to have a shorter decay time τ than the 689 nm light.

rate is not limited by the response time of this photodiode, we compared the decay of the cavity transmission with the decay of the $+1^{\text{st}}$ diffracted order of the AOM before the cavity. We found the photodiode able to distinguish between the two, where the decay directly from the $+1^{\text{st}}$ diffracted order happens 'instantly' compared to the decay of the cavity transmission.

Since we want to characterize the mock cavity for both 689 nm and 813 nm light, we first locked the cavity to the 689 nm laser and performed a ring-down measurement. Due to the cavity mirror's HR and AR coatings not being specifically suited for this wavelength (only 698 + 813), we achieved a cavity coupling efficiency for this wavelength of only 5-10 %. This nevertheless turned out to be enough for locking the cavity. We then switched fibers and re-optimized the cavity alignment for the 813 nm light, where we reached a coupling efficiency of ∼40 % and locked the cavity using the acquired error signal in Fig. 5.9. An example of a ring-down measurement for both wavelengths is given in Fig. 5.11. Each trace is fitted to an exponential decay function

$$I(t) = I_0 \exp\left(-\frac{t - t_0}{\tau}\right) + c \tag{5.4}$$

where t_0 is the time at which the decay starts and τ is the $1/e$ decay time of the intensity. By performing ten ring-down measurements for each wavelength and using the equations 5.3 and

$$\mathcal{F} = \frac{FSR}{\Delta\nu_{cav}} \tag{5.5}$$

we can determine the cavity's linewidth and finesse from the fitting parameter τ and the cavity's $FSR(= 1.47\,\text{GHz})$. The results are presented in Tab. 2. The measured finesse for both wavelengths is significantly lower than expected based on the measurement from [17]. This is likely due to the cavity's spacer and mirrors being exposed to air and temperature fluctuations for a large amount of time. Fortunately, this cavity will not be used for trapping any atoms. To verify the measured characteristics, we plug in the measured linewidth for 813 nm from Tab. 2 into Eq. 5.2 together with the carrier and sideband power from Fig. 5.8. This results in a frequency discriminant $D \approx 2.4 \times 10^{-3}\,\text{mV/Hz}$, which translates to a linear response of 420 Hz/mV. This is

Cavity parameters	689 nm	813 nm
τ	$0.285 \pm 0.007\,\mu$s	$0.211 \pm 0.003\,\mu$s
$\kappa/2\pi = \Delta\nu_{cav}$	558 ± 14 kHz	756 ± 9 kHz
$\mathcal{F}$	2630 ± 70	1940 ± 20

Table 2: Measured characteristics of the mock bowtie cavity. All uncertainties originate from the standard deviation of the fitting parameter τ and the shot-to-shot fluctuations of τ.

a little bit lower than expected based on the measured slope of the error signal, but still roughly the same order of magnitude. The difference is likely due to the way the error signal is visualized on the oscilloscope. Since we scan over a cavity resonance with the piezo, the *apparent* gradient of the linear slope depends on the rate and amplitude at which this scan is performed, while the error signal's actual shape probably does not change that much.

Building and characterizing this mock system provided enough practice to easily transfer the optical setup to the mHz-machine, where I can characterize the experiment's bowtie cavity in the science chamber.

Chapter 6

The mHz-machine

After building the optical setup for the cavity beams and characterizing the mock bowtie cavity, we moved the breadboard with the optical setup from Fig. 5.5 onto the mHz-machine experiment. After placing the breadboard on top of the science chamber and realigning the lattice and probe beams to the experiment's cavity, I was able to lock the cavity to the light of lattice beam X. This lock entailed some problems that did not occur on the mock system, resulting in two different approaches for creating a 'short-' and 'long-term' lock. The first part of this chapter will report on these two locks and the solutions proposed for the problems that arose with them.

Using the short-term lock, we were able to perform similar ring-down measurements as on the mock system. This allowed us to determine the science chamber cavity linewidth and finesse for 813 nm and 689 nm light.

In addition, I also quantified the frequency splitting of the bowtie cavity resonances for orthogonal polarization components, as described in Sec. 2.2.3.

With the obtained cavity parameters for 813 nm light, we were able to perform some calculations to predict the performance of the optical lattice. These calculations resulted in an estimate of the maximum optical lattice trap depth and an estimate of the optical lattice contrast, both of which are visualized for different lattice velocities.

The obtained cavity parameters for 689 nm light, allowed us to calculate the probe powers and pulse lengths required to apply π- or $\pi/2$-pulses to atoms inside the cavity.

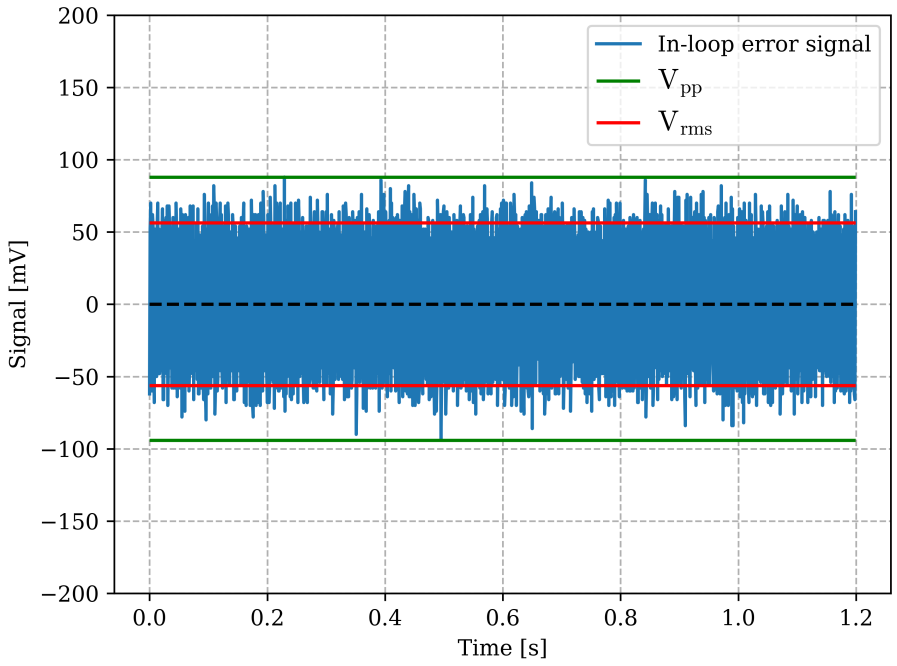


Figure 6.1: In-loop error signal of the short-term lock. The rms variation of the signal, between the two red lines, is used to calculate the stability of the lock.

6.1 Science chamber cavity lock

Once the breadboard with the optics had been placed onto the experiment, we realigned both lattice beams and the probe beam with the science chamber bowtie cavity. This went relatively easily due to the poles fixing the alignment of the breadboard, relative to the science chamber cavity. For the 813 nm light, we obtained a cavity coupling efficiency of ∼40 %, similar to that of the mock cavity. For the 689 nm light, the coupling efficiency improved to ∼20 %, compared to only 5-10 % for the mock cavity. Since this cavity uses exactly the same piezo tubes as the mock cavity, we could scan the length of the cavity over a resonance in a similar way as for the mock cavity. Using the same PDH-method, we were able to lock the experiment's cavity to lattice beam X.

This section provides a comparison between the stability and quality of a 'short-term' and a 'long-term' lock of the experiment's bowtie cavity. I will highlight the problems that occurred during these locks, which were not present for the mock cavity.

6.1.1 Short-term stability

Following the same procedure described in Sec. 5.4 and using the same scheme presented in Fig. 5.10, I obtained an error signal similar to that in Fig. 5.8, with an identical linear frequency response of 620 Hz/mV and a peak-to-peak size of $V_{pp} = 700$ mV. The apparently shallower slope of the error signal in Fig. 5.9 is merely an artifact of how this error signal is visualized, namely by scanning the cavity across a resonance. This figure therefore served mainly to provide a more intuitive, visual explanation of why adding the 10 kHz low-pass filter reduced the bandwidth of the PID loop. In this section, I will therefore use the linear slope of the error signal from Fig. 5.8 to calculate the stability of the lock, even though the 10 kHz low-pass filter on the mixer output is used in the actual lock scheme. By tuning the cavity far from resonance, the root mean square (rms) noise of this error signal was found to be $V_{rms} = 3$ mV, resulting in a signal-to-noise ratio of $S/N = 700/(2 \times 3) \approx 120$, where the factor of 2 arises from the definition of V_{rms} as the magnitude of variation from the mean in one direction. By multiplying the total rms spread of 6 mV with the linear frequency response of 620 Hz/mV, we can calculate

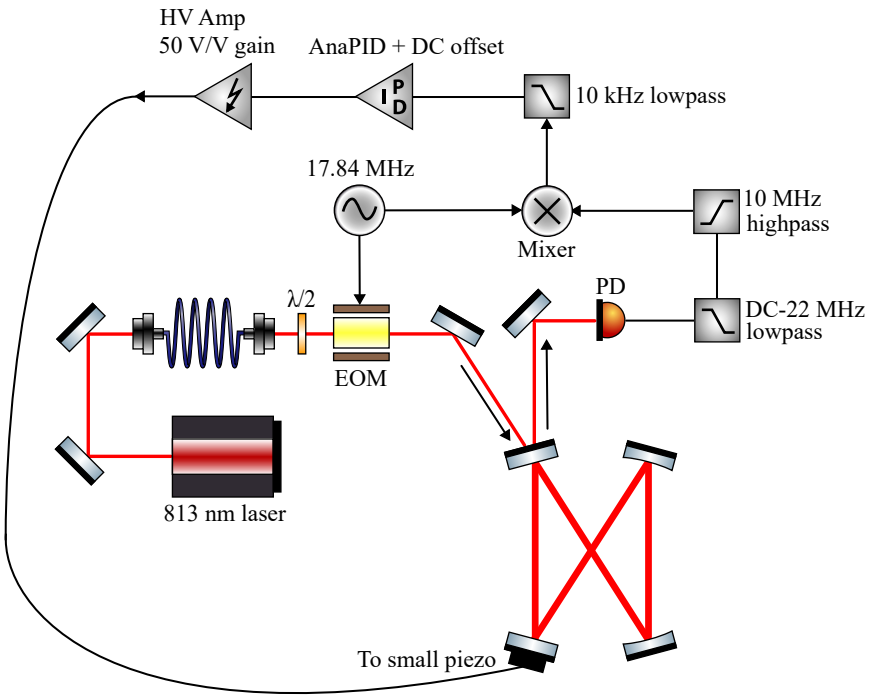


Figure 6.2: Schematic overview of the hardware used to make a long-term lock of the science chamber bowtie cavity, to the 813 nm laser.

the maximum achievable frequency stability of the lock for this error signal. This results in an ideal-case stability of $\Delta f_{lock} \approx 4\,\text{kHz}$, which means that the cavity length could be locked to a stability of 4 kHz.

Using the lock scheme from Fig. 5.10, the science chamber cavity lock behaved similarly to that of the mock cavity, locking cleanly to the peak of a resonance while exhibiting a comparable small oscillation around it. The in-loop error signal of this lock is presented in Fig. 6.1, over a span of approximately 1 second. The distance between the green lines indicates the peak-to-peak spread of the error signal ($V_{pp} = 182\,\text{mV}$), while the distance from the average (dashed black line) to a red line represents the root mean square (rms) variation of the error signal ($V_{rms} = 56\,\text{mV}$). We can determine the actual frequency stability of this lock by multiplying the total rms variation (the distance between the two red lines, $= 112\,\text{mV}$) with the linear frequency response of the error signal. This results in a lock stability of $\Delta f_{lock} = 620\,\text{Hz/mV} \times 112\,\text{mV} \approx 70\,\text{kHz}$, which is an order of magnitude less stable than the theoretically achievable stability of 4 kHz, but still below the expected cavity linewidth of ~200 kHz [17]. This lock therefore fulfills the requirement for the stability in the cavity length, which is set by the cavity pulling factor, mentioned in Eq. 1.1 in Sec. 1.1.1 [15].

In contrast to the lock of the mock cavity, which could be maintained for a few hours, this science chamber cavity lock lasted only 10-15 minutes. This was likely due to the large piezo used for locking, which suffered thermal damage during soldering of the Kapton wires to the piezo stack, causing hysteresis behavior in the large piezo as reported in [17]. In order to create a lock that can be maintained over a longer period of time, I tried to lock the cavity using only the small piezo. This is reported in the following section.

6.1.2 Long-term stability

In order to lock the cavity using only the small piezo, the scheme in Fig. 5.10 needed to be slightly adjusted. The updated version is presented in Fig. 6.2, where the analogue PID is now also used to apply the DC offset that brings the cavity close to a resonance. Although the AnaPID's DC offset was more sensitive to tune than that of the function generator, making it more difficult to set the cavity to a near-resonance length, I managed to lock the cavity in this

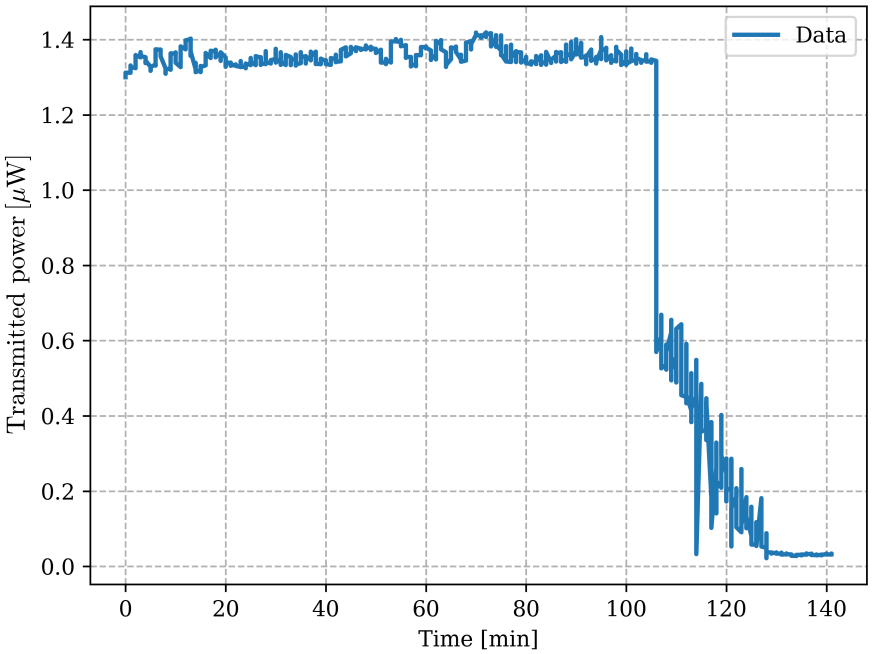


Figure 6.3: Long-term measurement of the science chamber bowtie cavity lock, to the 813 nm laser. The lock is monitored by measuring the cavity transmission of lattice beam X on a power meter.

way. This lock scheme provided a better long-term stability than the one in Fig. 5.10, where the longest measurement I was able to take is presented in Fig. 6.3. The lock is monitored by measuring the cavity transmission of lattice beam X on a power meter. A drop in the transmitted power indicates that the light is no longer resonant with the cavity length, which means that the cavity has unlocked. In this measurement the lock was able to sustain for around 100 minutes, after which the transmission dropped to zero. In practice, the cavity could remain locked for up to a few hours, similar to the lock of the mock cavity.

Despite this lock being more sustainable over the long-term, it unfortunately did not result in a qualitatively 'stable' lock. This meant that the lock was actually ramping the cavity length up and down across the full linear span of the error signal, which could have multiple causes. First, the TD250 PiezoDrive that we use as a high-voltage amplifier (50 V/V gain) could be too powerful for the small piezo. Because the walls of the small piezo tube are two times thinner than for the large tube, the contracting response for a given voltage will be twice as big compared to the large piezo, see Eq. 5.1. Even though the applied voltages remain unchanged, this stronger response could result in an oscillating behavior of the lock around a resonance, that was not present when using the large piezo. To overcome this problem, a high-voltage amplifier with a lower gain could be used. It must however be taken into consideration that the lower gain amplifier must still be able to scan the length of the cavity by at least a full FSR, or equivalently, by at least 813 nm for the lattice light.

The second possible cause relates to the way I connected the high-voltage amplifier to the feedthrough wires of the science chamber. In the mock system, the connection to the vacuum chamber's feedthrough wires was soldered. On the experiment however, soldering was not possible due to space restrictions and possible contamination of nearby optics with soldering flux. I therefore connected the coax cables, coming from the amplifier, to the feedthrough wires using a screw terminal. This initially provided good connectivity, with the measured capacitances of the piezo tubes being similar to those of the mock cavity. However, the high voltages (up to 500 V) that are sent through these connections can result in the formation of oxidation at the connection points of the wires. Because the coax cables and feedthrough wires are not seamlessly connected,

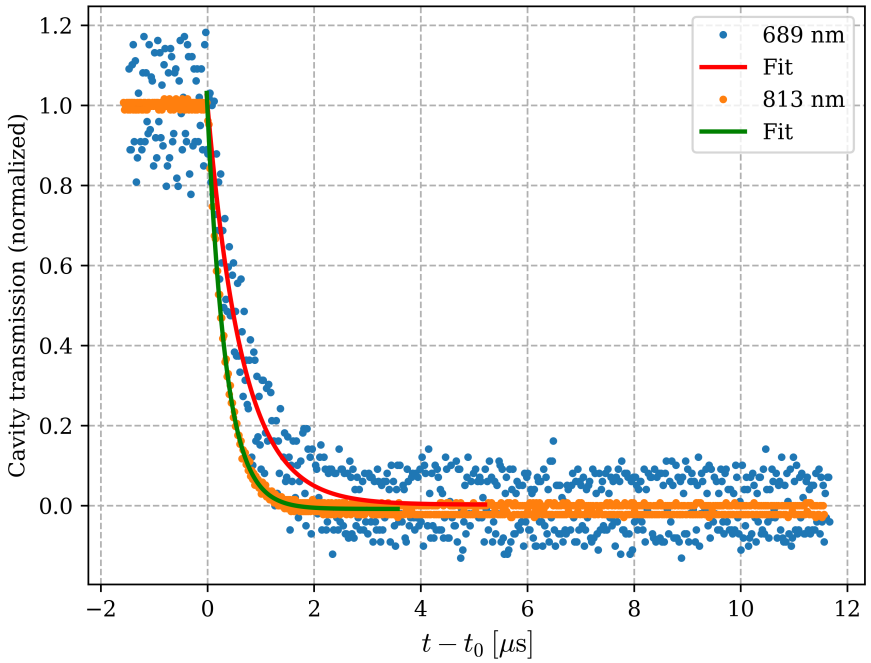


Figure 6.4: Example ring-down measurement of the science chamber bowtie cavity. The 813 nm light is found to have a shorter decay time τ than the 689 nm light. The difference in signal-to-noise ratio between the traces is due to the different photodiodes being used to monitor the cavity transmission.

like they would be when soldered, the oxidation between them will act as a small capacitor. The formation of these extra capacitances can induce mechanical resonances in the piezo. If the piezo's transfer function contains nonlinearities at certain resonance frequencies, the magnitude of the piezo's response at these frequencies will diverge [51]. If the gain and bandwidth of the PID loop are high enough such that these nonlinear responses are picked up by the error signal, it can result in instabilities of the lock. Since soldering the connections instead of using screw terminals is undesirable for the reasons mentioned above, the best solution would be to further reduce the gain and bandwidth of the lock. This could be achieved by using a lower-gain amplifier, as mentioned above, or by further filtering the error signal with additional low-pass filters.

6.2 Science chamber cavity characterization

From the section above we can conclude that locking the cavity with the large piezo results in a qualitatively better lock, than using the small piezo. I therefore used this short-term stable lock described in Sec. 6.1.1 for characterizing the bowtie cavity in the science chamber.

This allowed us to perform a similar ring-down measurement as described in Sec. 5.5, to find out the linewidth and finesse of this cavity that will be used in the experiment. Additionally, the occurrence of polarization mode dependent cavity resonances that are present in ring cavities, as described in Sec. 2.2.3, is quantified for this bowtie cavity.

6.2.1 Ring-down measurement

For the science chamber cavity, ten ring-down measurements for both 813 nm and 689 nm light were performed in exactly the same way as on the mock system. An example ring-down measurement of the science chamber cavity, for both wavelengths, is presented in Fig. 6.4. The measurement with 689 nm light has a lower signal-to-noise ratio than the one in Fig. 5.11.

Cavity parameters	689 nm	813 nm
τ	$0.636 \pm 0.036\,\mu$s	$0.338 \pm 0.007\,\mu$s
$\kappa/2\pi = \Delta\nu_{cav}$	250 ± 14 kHz	471 ± 10 kHz
$\mathcal{F}$	5870 ± 330	3120 ± 70

Table 3: Measured characteristics of the science chamber bowtie cavity. All uncertainties originate from the standard deviation of the fitting parameter τ and the shot-to-shot fluctuations of τ. The high uncertainty in the finesse for 689 nm is likely due to the lower signal-to-noise ratio for these measurements.

This is due to the APD130A/M avalanche photodiode from Thorlabs being used to monitor the transmission of the 689 nm light, instead of the PDA8A2 fixed gain photodiode used on the mock system. This was nevertheless good enough to fit the data to the exponential decay in Eq. 5.4. The results of the measurements are presented in Tab. 3. The cavity's finesse for both wavelengths is roughly twice that of the mock cavity, which was expectable based on the difference with which both cavities were treated. We suspect that the relatively high uncertainty in the finesse for 689 nm is due to the lower signal-to-noise ratio of the cavity transmission measurement.

With the obtained cavity characteristics in Tab. 3, it is possible to calculate the expected properties of the optical lattice. Additionally, these values allow us to determine the amount of optical power needed to probe atoms inside the cavity on the ${}^1S_0 \rightarrow {}^3P_1$ transition. These calculations are presented in Sec. 6.3, together with some rough requirements that need to be met in order to reach the superradiant lasing threshold.

6.2.2 Non-degenerate polarization eigenmodes

As described in Sec. 2.2.3, ring cavities exhibit birefringent properties due to the non-zero angle between the cavity mode beam and mirror surface normal [38]. This results in S- and P-polarized light not having degenerate longitudinal cavity modes. This effect has been observed and quantified for the bowtie cavity used in this experiment. While scanning the cavity length over a resonance with the piezo, I rotated the last $\lambda/2$-plate in the path of lattice beam X until a second transmission peak appeared next to the 'original' one. I fixed the angle of the $\lambda/2$-plate such that both peaks had the same height, indicating that the light's polarization made an angle of 45° with the S- and P-plane of the cavity. The same effect was also observed for lattice beam Y and the probe beam. The cavity transmissions of both polarization components are plotted in Fig. 6.5, together with their sidebands used as a frequency reference. Since the plot is made by scanning the cavity, it shows that there are two cavity lengths resonant with the incoming light. By fitting each transmission to a triple Lorentzian function, we found the frequency shift between both polarization components to be $\delta\nu = 6.69 \pm 0.03$ MHz, for the 813 nm light. By using Eq. 2.31, this translates to a difference in experienced cavity round trip phase shift of $\Delta\Phi = \Delta\phi_s - \Delta\phi_p \approx \frac{\pi}{108}$, between S- and P-polarized light. Because the magnitude of the resonance frequency shift is larger than the cavity's 471 kHz linewidth, it is possible to couple only one of the polarization components into the cavity, while the orthogonal component is reflected from the incoupling mirror. This property is used, for example, to realize a Hänsch–Couillaud lock, as described in [37].

The same effect was also observed for the 689 nm probe light, but the magnitude of the frequency shift has not been measured for this wavelength.

6.3 Predictive calculations

Now that we have measured the science chamber cavity characteristics in Tab. 3, we can use these numbers to calculate the performance of the cavity. I will first look at the power enhancement factor of the cavity.

Following the same steps to get to the cavity's transmitted and reflected fields as described in Sec. 2.2.1 and Sec. 2.3 respectively, we can also write the total electric field *circulating* inside

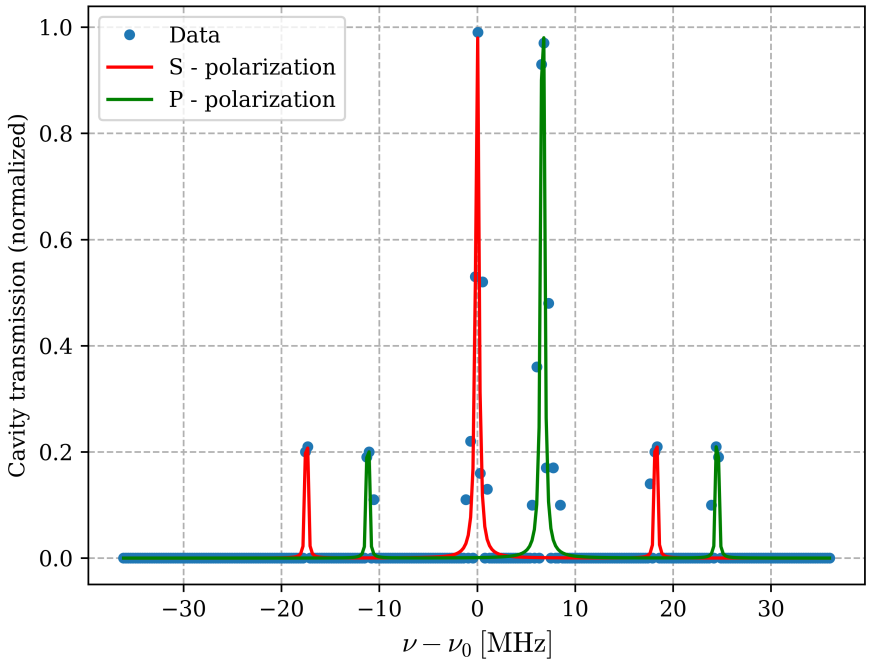


Figure 6.5: Non-degenerate polarization eigen modes of the science chamber bowtie cavity, using 813 nm light. The shift in the resonance frequency is measured to be 6.7 MHz.

the cavity E_{circ} just after the first mirror as a function of the incident electric field E_{in}. The total circulating field consists of the initial transmitted field tE_{in} and the sum of all oscillations inside the cavity

$$E_{circ} = tE_{in} \sum_{n=0}^{\infty} \left(r^2 e^{ikL_{RT}}\right)^n, \tag{6.1}$$

with L_{RT} the round trip cavity length and r and t the individual mirror's amplitude reflection and transmission coefficients respectively. By using the geometric sum $\sum_n^{\infty} x^n = \frac{1}{1-x}$, this can be written as

$$E_{circ} = E_{in} \frac{t}{1 - r^2 e^{ikL_{RT}}}. \tag{6.2}$$

Using that the power is proportional to the square of the field amplitude $P \propto |E|^2$ and assuming that the incoming light is perfectly on resonance with the cavity length, such that the round trip phase shift is an integer multiple of 2π ($kL_{RT} = m2\pi$), making $e^{ikL_{RT}} = 1$, we can write

$$P_{circ} = P_{in} \frac{T}{(1-R)^2}. \tag{6.3}$$

Where $R = r^2$ and $T = t^2$ are the power reflection and transmission coefficients respectively and P_{circ} is the circulating power inside the cavity. The power enhancement factor of a cavity G is defined as the ratio of intra cavity power to incident power

$$G = \frac{P_{circ}}{P_{in}} = \frac{T}{(1-R)^2}. \tag{6.4}$$

Using Eq. 2.22 for the expression of the cavity finesse ($\mathcal{F} = \frac{\pi\sqrt{R}}{1-R}$) the power enhancement factor of a cavity is written as

$$G = \frac{\mathcal{F}}{\pi}. \tag{6.5}$$

Any resonant light coupled in to the cavity is amplified by this factor, which linearly depends on the cavity's finesse. This equation allows us to determine the optical power (and intensity) of the lattice and probe beams inside the cavity.

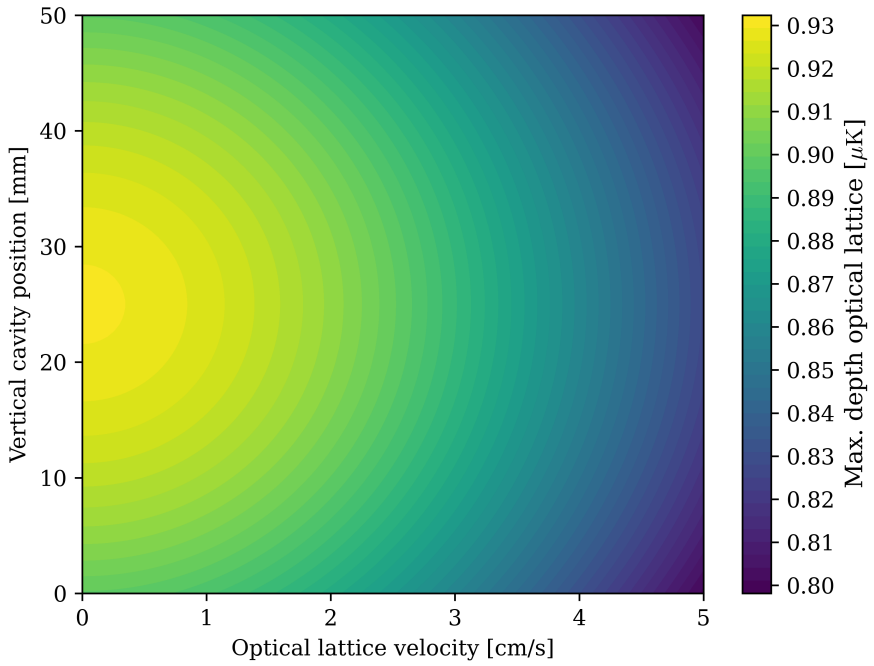


Figure 6.6: Maximum trap depth of the optical lattice, calculated using the cavity linewidth and finesse from Tab. 3, while taking the 40 % coupling efficiency of both lattice beams into account. The deepest trap depth is obtained at the mode waist and degrades for larger lattice velocities, due to the cavity enhancement factor decreasing for the off-resonant light from lattice beam Y. A power of 1 mW in each lattice beam, before the cavity, is used here.

6.3.1 Optical lattice

Our goal is to calculate the trap depth of the optical lattice inside the cavity. This will give an indication of the kinetic energy that the incoming atoms need to have, in order to be trapped by the optical lattice. The dipole trap depth is calculated using Eq. 2.4, so we need to determine the total intensity of the optical lattice inside the cavity.

For lattice beam X this is simply the incoming power multiplied by G, because the cavity is locked to this beam. However, to create a moving optical lattice, the frequency of lattice beam Y is shifted relative to lattice beam X. Whether this is realized by frequency shifting both beams in opposite directions or only shifting lattice beam Y, it will always detune lattice beam Y from cavity resonance because the cavity lock will follow the frequency of lattice beam X. For non-perfect impedance matching, the power enhancement factor takes the form

$$G(\Delta\omega) = \frac{G_0}{1 + \left(\frac{2\Delta\omega}{\kappa}\right)^2} \tag{6.6}$$

where $G_0 = \frac{\mathcal{F}}{\pi}$ is the on-resonance power enhancement factor (Eq. 6.5), $\Delta\omega = \omega_{light} - \omega_{cavity}$ is the detuning from cavity resonance and $\kappa = 2\pi \times \Delta\nu_{cav}$ the cavity linewidth. Because the cavity is locked to lattice beam X, $\Delta\omega$ also resembles the detuning between the lattice beams. Since the optical lattice velocity is directly proportional to this detuning by $v_{lattice} = \frac{\lambda}{2}\Delta\nu$, where $\Delta\nu = \Delta\omega/2\pi$, the power enhancement factor is directly related to the lattice velocity by

$$G(v_{lattice}) = \frac{G_0}{1 + \left(\frac{4v_{lattice}}{\lambda\Delta_{cav}}\right)^2}. \tag{6.7}$$

These equations allow us to calculate the optical power of each lattice beam inside the cavity, where the enhancement factor for lattice beam Y is lower depending on the desired lattice velocity.

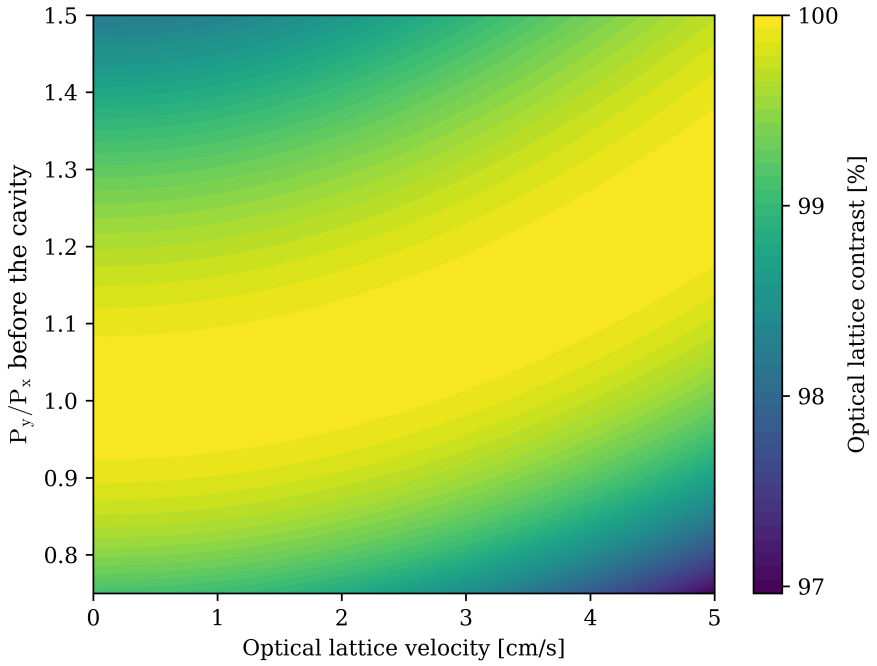


Figure 6.7: Optical lattice contrast for different lattice velocities. A decrease in contrast can be compensated by increasing the power ratio of the lattice beams, P_y/P_x, before the cavity.

The total maximum optical power at each anti-node of the optical lattice equals

$$P_{tot}^{cav} = P_x^{cav} + P_y^{cav} + 2\sqrt{P_x^{cav} P_y^{cav}}, \tag{6.8}$$

where P_x^{cav} and P_y^{cav} are the intra cavity optical powers of lattice beam X and Y respectively.

The total maximum intensity is obtained by dividing P_{tot}^{cav} by the cross section area of the 813 nm cavity mode. As seen in Fig. 2.8, the mode radius (and therefore cross section area) changes along the axial position in the cavity. This means that the intensity and dipole trap depth also change along the axial cavity position. Because the optical lattice spans between the two flat cavity mirrors (=50 mm), see Fig. 1.3, I calculated the maximum trap depth of the optical lattice between these two mirrors, for a range of lattice velocities. The results are visualized in Fig. 6.6, where I used an optical power of 1 mW in each lattice beam before the cavity and took the ∼40 % coupling efficiency for each beam into account. The biggest trap depth is obtained at the waist of the cavity mode. For increasing lattice velocities, the depth of the lattice becomes shallower. This is due to the cavity enhancement factor decreasing for the off-resonant light of lattice beam Y. The obtained lattice depth is significantly lower than expected based on the simulation from [16], which uses a depth of 30 μK at a lattice velocity of 1 cm/s. Because of the 813 nm injection lock (see Chapter 4), we can easily increase the optical power in each beam before the cavity to a few tens of mW. To reach the 30 μK trap depth at a lattice velocity of 1 cm/s, we would require 35 mW of power in each lattice beam before the cavity. More optical power could be used to further increase the depth, but one has to be careful that this could damage the HR coating of the cavity mirrors. Since the finesse measurement was done with a free running 813 nm laser, the cavity lock was not extremely stable which resulted in some fluctuations of the cavity transmission. This could have influenced the ring-down measurement and therefore the obtained value for the cavity finesse. A higher finesse for 813 nm light will result in a larger power enhancement factor and would therefore require less optical power before the cavity, to reach similar lattice depths.

To get a better understanding of the structural shape of the optical lattice, we can look at the lattice contrast m. This is a measure to compare the optical lattice intensity maxima to the

intensity minima. A contrast of 100 % means that the fields of both beams constructively add up at each anti-node and completely cancel out at each node, provided that the polarizations of both beams are parallel. A contrast of 0 % means that there is no interference between the beams and therefore no optical lattice is formed. The contrast is given by

$$m = \frac{P^{cav}_{tot,max} - P^{cav}_{tot,min}}{P^{cav}_{tot,max} + P^{cav}_{tot,min}}, \tag{6.9}$$

where I used the maximum and minimum of the total intra cavity power instead of intensity, since the cross section area of the cavity mode will drop out of the equation anyway. The maximum total intra cavity power is given by Eq. 6.8, for the minimum power the plus-sign before the last term in this equation turns into a minus-sign. To show the effect of the frequency shift between the lattice beams on the contrast of the optical lattice, Eq. 6.9 can be rewritten as

$$m = \frac{2\sqrt{P^{cav}_y / P^{cav}_x}}{1 + (P^{cav}_y / P^{cav}_x)}, \tag{6.10}$$

where P^{cav}_y / P^{cav}_x is the ratio of intra cavity optical power in beam Y to intra cavity optical power in beam X. This intra cavity power ratio relates to the power ratio before the cavity as

$$\frac{P^{cav}_y}{P^{cav}_x} = \frac{G(\Delta\omega)}{G_0}\frac{P_y}{P_x}, \tag{6.11}$$

where P_y/P_x is the power ratio of the lattice beams before the cavity and $G(\Delta\omega)/G_0$ is the ratio of their respective cavity enhancement factors. The contrast of the optical lattice as a function of the power ratio *before* the cavity, is visualized for a range of lattice velocities in Fig. 6.7. This plot shows that for a static optical lattice, the highest contrast is reached for a power ratio of 1. As the lattice velocity increases, the contrast decreases but this can be compensated by increasing the power ratio of the lattice beams. This is done by rotating the $\lambda/2$-plate before the PBS that splits up the 813 nm light into the two lattice beams.

The simulations in [16] are performed with an optical lattice velocity of 1 cm/s, which results in a simulated 91 % atom loading efficiency into the lattice. At this velocity the decrease in lattice contrast is very small, such that a power ratio of ≈ 1 still yields a contrast of $m = 100\,\%$.

6.3.2 Rabi oscillations $^1S_0 \rightarrow {}^3P_1$ transition

When probing atoms, it is typically desired to apply π-pulses to bring the atoms into the excited state, or $\pi/2$-pulses to put the atoms in a superposition of ground and excited state. The length and intensity of the pulse determine what rotation is applied on the Bloch sphere, see Fig. 6.8. To quantify a pulse, we can calculate the pulse area Θ

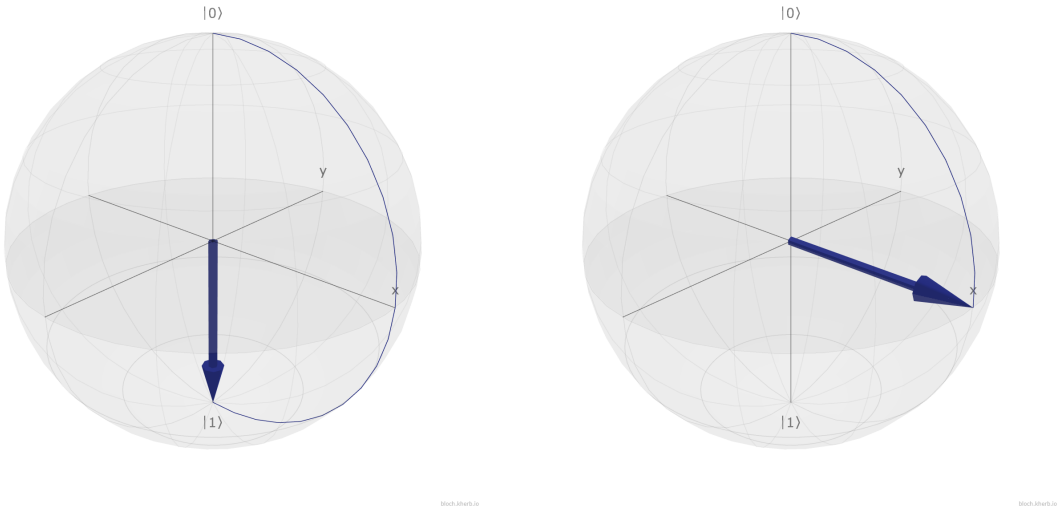
$$\Theta = \int_0^\tau \Omega(t)dt, \tag{6.12}$$

where Ω is the effective Rabi frequency and τ is the length of the pulse in time. The Rabi frequency relates to the electric field amplitude E_0 by

$$\Omega(t) = \frac{\mu E_0(t)}{\hbar}, \tag{6.13}$$

where μ is the dipole moment of the atomic transition that is being probed. Plugging Eq. 6.13 into Eq. 6.12 shows that longer and more powerful pulses need to be applied when probing weaker atomic transitions.

In the early stage of this experiment, the atoms will be probed on the 689 nm $^1S_0 \rightarrow {}^3P_1$ transition. Where $^1S_0$ is the ground state ($|0\rangle$) and $^3P_1$ the excited state ($|1\rangle$). This transition has a saturation intensity of $I_{sat} = 2.95\,\mu\mathrm{W/cm^2}$ [53], which is the optical intensity of 689 nm light at which the rate of absorption/stimulated emission is equal to the rate of spontaneous emission. Considering a two-level atom, for $I >> I_{sat}$ the ground and excited state populations are both equal to 1/2. The Rabi frequency can be written in terms of this saturation intensity, using the definition of the on-resonance ($\Delta = \omega_{laser} - \omega_{atom} = 0$) saturation parameter s_0



(a) (b)

Figure 6.8: (a) Bloch sphere rotation of a π-pulse. (b) Bloch sphere rotation of a $\pi/2$-pulse. From [52].

$$s_0 \equiv \frac{I}{I_{sat}} = \frac{2\Omega^2}{\Gamma^2} \tag{6.14}$$

where $\Gamma = \frac{1}{\tau} = 2\pi \times \gamma$ is the natural linewidth of the transition. Reordering the terms gives

$$\Omega = \Gamma\sqrt{\frac{I}{2I_{sat}}}, \tag{6.15}$$

where I assumed the Rabi frequency (and therefore electric field amplitude) to be constant for the duration of the pulse. Plugging Eq. 6.15 back into Eq. 6.12 the expression for the pulse area becomes

$$\Theta = \Gamma\sqrt{\frac{I}{2I_{sat}}}\tau, \tag{6.16}$$

where τ is again the length of the pulse. If we want to achieve the saturation intensity of the ${}^1S_0 \rightarrow {}^3P_1$ transition at the cavity mode waist, the incoming probe power *before* the cavity must equal

$$P_{in}^{sat} = \frac{I_{sat} \cdot A}{G \cdot \eta}, \tag{6.17}$$

where A is the cross section area of the cavity mode at the waist, $G = \mathcal{F}/\pi$ is the power enhancement factor of the cavity for 689 nm light and $\eta \approx 20\,\%$ is the cavity coupling efficiency of the probe beam. Taking into account that the waist radius is unequal between the S- and T-plane of the cavity ($A = \pi \cdot w_S \cdot w_T$), the saturation probe power before the cavity equals $P_{in}^{sat} = 7.33 \times 10^{-3}$ nW. This number is very low because the incoming power is amplified by a factor of $\mathcal{F}/\pi \approx 1867$ inside the cavity, assuming that the cavity is also resonant with the 689 nm light. When driving the atoms between the ground and excited state, the intensity of the probe light would generally be in the saturated regime where $s_0 >> 1$, $I >> I_{sat}$. In this regime, the relatively high intensity of the probe light induces power broadening of the atomic transition, resulting in an effective linewidth

$$\Gamma_{eff} = \Gamma\sqrt{1 + \frac{I}{I_{sat}}}. \tag{6.18}$$

Where Γ is the original, natural linewidth of the atomic transition. Replacing this expression

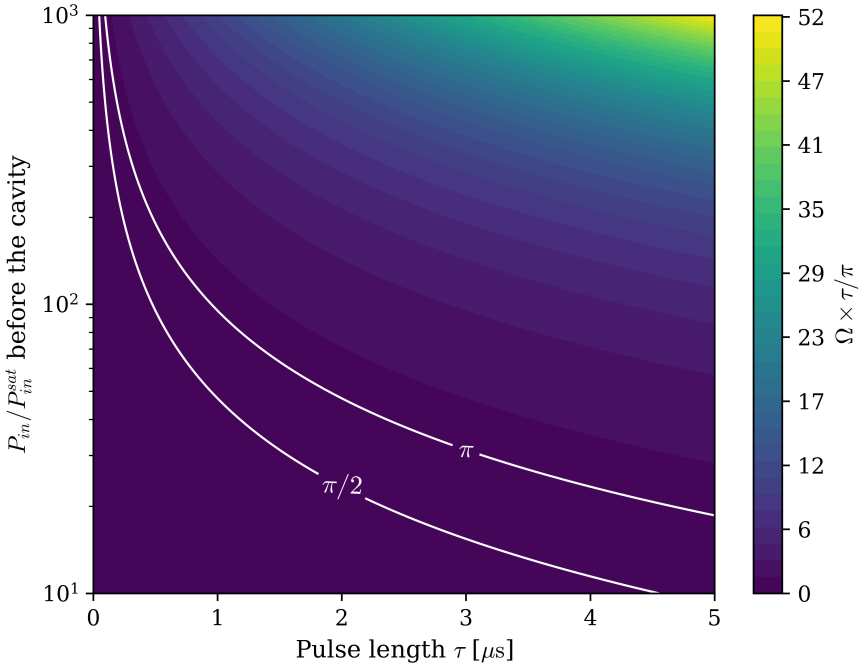


Figure 6.9: Pulse area ${}^1S_0 \rightarrow {}^3P_1$ transition for different probe powers and pulse lengths, in the saturated regime ($s_0 >> 1$). The white contour lines follow the curves of π- and $\pi/2$-pulses. The pulse shape is approximated to be a square (no time dependence of electric field amplitude).

for the effective linewidth in Eq. 6.16, results in the pulse area in the saturated regime being written as

$$\Theta_{sat} = \frac{\Gamma}{\sqrt{2}}\sqrt{\frac{I}{I_{sat}}\left(1+\frac{I}{I_{sat}}\right)}\tau = \frac{\Gamma}{\sqrt{2}}\sqrt{s_0\,(1+s_0)}\tau. \tag{6.19}$$

In Fig. 6.9 the pulse area for the ${}^1S_0 \rightarrow {}^3P_1$ transition, in the saturated regime, is plotted for different probe powers and pulse lengths. The probe powers are given as the ratio of probe power before the cavity, P_{in}, to the saturation probe power before the cavity, P_{in}^{sat}. Because the excited state lifetime of the ${}^3P_1$ state is $\tau_{\text{life}} \approx 21\,\mu$s, the pulse duration must be kept well below this timescale. If pulses on the order of τ_{life} or longer are used, the atoms will have time to spontaneously decay back to the ground state during the pulse itself, reducing the effectiveness of the excitation. For this reason, the considered pulse lengths span up to $5\,\mu$s. The white contour lines show which probe powers and pulse lengths need to be used, in order to achieve π- or $\pi/2$-pulses.

Chapter 7

Conclusion & Outlook

This thesis describes an optical setup built for trapping and probing strontium atoms inside a ring cavity. Trapping is achieved with an optical lattice at the magic wavelength of 813 nm for the ${}^1S_0 \rightarrow {}^3P_0$ clock transition in strontium. The probe setup initially targets the broader ${}^1S_0 \rightarrow {}^3P_1$ transition at 689 nm, but can be modified to target the clock transition at 698 nm by changing the optical fiber. The optical lattice is formed inside a four-mirror ring cavity, in a 'bowtie' configuration. The lattice forms through the interference of two counter-propagating 813 nm beams inside the cavity. By inducing a frequency shift between these two lattice beams, the lattice can be made to move. This allows atoms to be transported through the cavity, which will be required for achieving a continuously operating optical clock.

Both the 813 nm lattice beams and the 689 nm probe beam are coupled into an overlapping mode of the cavity. Since we want to trap and probe the atoms at the same time, this requires the cavity to simultaneously be resonant with both wavelengths. To achieve this, a frequency shifting setup has been built that allows us to shift the frequency of the lattice beams. Because the cavity is locked to one of the lattice beams, the cavity length follows this frequency shift. The frequency of the lattice light can therefore be tuned until the longitudinal cavity modes of both wavelengths overlap.

To increase the optical power available for the optical lattice, an injection lock setup was built. This setup boosts the available power from a few mW to several tens of mW, up to $\sim$100 mW, while preserving the frequency stability of the 813 nm parent laser. The short-term quality of the injection lock was verified through a homodyne beat-note measurement between the seed light and the child laser output, confirming that the child laser phase-locked to the seed laser. The long-term stability was verified by showing that the child laser was able to follow the 50 MHz/h frequency drift of the free-running parent laser.

Once all beams were coupled into the cavity, the cavity was locked to one of the lattice beams using the Pound-Drever-Hall method. An initial locking scheme produced a lock of limited quality, in which the piezo continuously ramped the cavity length across the resonance. This lock could nonetheless be maintained for several hours. To improve the lock quality, an alternative scheme was implemented. This approach resulted in a qualitatively better lock, achieving a frequency stability of 70 kHz, which is below the measured cavity linewidth of 250 kHz, indicating that the stability achieved is within the upper limit required for operation in the bad-cavity regime. The frequency stability of the cavity is currently a factor of three above the 20–25 kHz stability goal. However, further improvement should be possible since the obtained PDH error signal, theoretically allows for a lock stability of 4 kHz. Unfortunately, this 'improved' scheme did not result in a lock that was maintainable for more than 10-15 minutes. This was likely due to the piezo used for locking having sustained damage in the past, resulting in hysteresis behavior.

With the cavity locked using the second scheme, the experiment's bowtie cavity could be characterized via a ring-down measurement, from which the cavity's finesse was calculated. This resulted in a finesse of 3120 for the 813 nm light and a finesse of 5870 for the 689 nm light.

Using these measured cavity parameters, predictive calculations were made for the cavity's performance, focusing on the maximum achievable lattice trap depth and the lattice contrast at different lattice velocities. In addition, the probe powers and pulse lengths required to drive atoms on the ${}^1S_0 \rightarrow {}^3P_1$ transition were derived.

The main area for improvement in this project, lies in achieving a better stability of the cavity lock. One possible origin of this instability could lie in the piezo's transfer function, which describes the magnitude of its mechanical response as a function of modulation frequency. To measure this transfer function, a laser would need to be locked to the bowtie cavity. By generating a beat note between this locked laser and an independent reference laser, the frequency stability of the cavity-locked laser could be compared to that of the reference laser. By modulating the cavity's piezo at different frequencies, the cavity laser's frequency should exhibit increased instability whenever the modulation frequency hits a resonance or nonlinearity in the piezo's

response. This measurement could be performed for both piezos of the bowtie cavity, and from the resulting transfer functions, the frequencies that should be avoided in the PID-loop could be identified.

Since locking the cavity using the large piezo did not result in a long-term stability, one option is to implement a second PID loop that slowly steers the DC offset sent to the small piezo. This could potentially compensate for the large piezo's inability to keep the cavity on resonance with the light over time. An alternative solution is to lock the cavity using only the small piezo. This would require reducing the ramping of the in-loop error signal across resonance, which could be achieved by lowering the gain and bandwidth of the PID loop. This could be implemented, for instance, by adding more low-pass filters or using a lower-gain high-voltage amplifier. Care must be taken, however, since these changes could degrade the lock's long-term stability. In particular, a strongly reduced gain may prevent the piezo from following the laser's frequency drift, as the resulting smaller maximum piezo displacement would limit its ability to track larger frequency excursions.

To give an outlook on the future steps that could be taken in this experiment: once atoms can be transported from the red MOT to the science chamber using the dipole guide, the alignment of the dipole guide with the cavity axis could be verified by imaging the atoms. This could be done using the telescope system already implemented on the breadboard of the optical setup, together with a camera to image the atomic positions in the dipole guide via fluorescence detection. This would use 461 nm light resonant with the ${}^1S_0 \rightarrow {}^1P_1$ transition in strontium. By propagating this beam through the dipole guide, transverse to the cavity axis, the atoms can be probed and fluorescence emission will reveal their positions.

Additionally, once atoms are trapped inside the cavity using the reservoir trap, it would be possible to search for the first signals of atom-cavity coupling, for example, by detecting normal mode splitting on the ${}^1S_0 \rightarrow {}^3P_1$ transition, where the size of the frequency splitting scales linearly with the coupling strength.

Finally, the main goal going forward would of course be to determine whether atoms can be trapped inside the optical lattice, and seeing atoms being transported through the cavity with the moving optical lattice.

Acknowledgments

First, I would like to thank my supervisor prof. dr. Florian Schreck for giving me the opportunity to do my master project in one of his amazing labs, where I have learned so much over the past year. I am very grateful to have been a member of the Strontium Quantum Gases group, here at the University of Amsterdam.

I would like to thank the superradiant optical clock team for everything this year. First of all Benedikt Heizenreder, my direct supervisor. Benedikt always had a solution for the problems I came across and has been very encouraging throughout this project. I am impressed by his incredible amount of knowledge about lasers, cavities and all other aspects of cold-atom experiments and I feel grateful to have learned from him. I highly appreciate the time he was able to make, for guiding me through the project and writing this thesis, while also completing his own PhD. Thank you very much for that. Second, I thank Ananya Sitaram for her help whenever Benedikt was not around, for the feedback she provided on my presentation and for the Halloween party she hosted for the whole group.

I also would like to express my gratitude to the other teams in the group. Thank you Ivo Knottnerus, for your willingness to listen to the problems I faced and coming up with ingenious solutions. You were always able to help, as a supervisor for my bachelor project and even without being so for my master project. I have learned a lot from our physics discussions and from your astonishing amount of knowledge and experience from working in this strontium group. Also thanks to Alex Urech, whose enthusiasm about physics is very infectious. I appreciate your patience when repeatedly explaining how the red-laser system works and how to lock it. You always had time to discuss, think along with my project and helped setting up the new DDSs in our lab.

Thank you András Gácsbaranyi for teaching me how to build the EOMs that I used in this project. By opening the door between the two clock labs I could always ask you a quick question or ask for help with stuff about vacuum systems. In addition, thank you Sumit Sarkar for teaching me how to lock the IR laser to the transfer cavity.

Finally, thanks to all the other team members Digvijay, Yu Chih, Davide, Junyu and Benoit. I felt like I could ask anybody in the whole team for help at any time, which I cannot thank you enough for. The large amount of knowledge shared by all the group members provided a fruitful environment in which I could learn more about AMO physics toward the end of my master's.

Second, I want to thank the people from the Technology Center without whom this whole project would never be possible. Especially thank you to Ronald Hassing for building and cleaning of the vacuum chamber that is used in the mock system. Thank you Edwin Baaij who is the brain behind the AnaPID controllers. I appreciate your willingness to think along and adapt the controller in order to suit them for locking the cavity, I have learned a lot about PID-loops from you.

As a final note, I would like to express my gratitude and wonder for having witnessed the realization of the world's first continuous superradiant laser, made possible by the hard work of Benedikt and Ananya. Last but not least, I wish Ying Cui and Haiwei Wang great success in their PhDs. I am confident that you will bring the mHz-machine experiment to new heights in the coming years.

References

[1] Louise Wolswijk et al. *Trapping, manipulating and probing ultracold atoms: a quantum technologies tutorial*. 2025. arXiv: 2510.20790 [cond-mat.quant-gas]. URL: https://arxiv.org/abs/2510.20790.

[2] M. H. Anderson et al. "Observation of Bose-Einstein Condensation in a Dilute Atomic Vapor". In: *Science* 269.5221 (1995), pp. 198–201. DOI: 10.1126/science.269.5221.198. eprint: https://www.science.org/doi/pdf/10.1126/science.269.5221.198. URL: https://www.science.org/doi/abs/10.1126/science.269.5221.198.

[3] Simon Stellmer et al. "Bose-Einstein Condensation of Strontium". In: *Phys. Rev. Lett.* 103 (20 Nov. 2009), p. 200401. DOI: 10.1103/PhysRevLett.103.200401. URL: https://link.aps.org/doi/10.1103/PhysRevLett.103.200401.

[4] Robin Santra, Kevin V. Christ, and Chris H. Greene. "Properties of metastable alkaline-earth-metal atoms calculated using an accurate effective core potential". In: *Phys. Rev. A* 69 (4 Apr. 2004), p. 042510. DOI: 10.1103/PhysRevA.69.042510. URL: https://link.aps.org/doi/10.1103/PhysRevA.69.042510.

[5] Andrew D. Ludlow et al. "Optical atomic clocks". In: *Rev. Mod. Phys.* 87 (2 June 2015), pp. 637–701. DOI: 10.1103/RevModPhys.87.637. URL: https://link.aps.org/doi/10.1103/RevModPhys.87.637.

[6] S. L. Campbell et al. "A Fermi-degenerate three-dimensional optical lattice clock". In: *Science* 358.6359 (2017), pp. 90–94. DOI: 10.1126/science.aam5538. eprint: https://www.science.org/doi/pdf/10.1126/science.aam5538. URL: https://www.science.org/doi/abs/10.1126/science.aam5538.

[7] Tara M. Fortier, Andre N. Luiten, and Helen S. Margolis. "Optical atomic clocks: defining the future of time and frequency metrology". In: *Optica* 13.1 (Jan. 2026), pp. 143–163. DOI: 10.1364/OPTICA.575770. URL: https://opg.optica.org/optica/abstract.cfm?URI=optica-13-1-143.

[8] Audrey Quessada et al. "The Dick effect for an optical frequency standard". In: *Journal of Optics B: Quantum and Semiclassical Optics* 5.2 (Apr. 2003), S150. DOI: 10.1088/1464-4266/5/2/373. URL: https://doi.org/10.1088/1464-4266/5/2/373.

[9] Hidetoshi Katori. "Longitudinal Ramsey spectroscopy of atoms for continuous operation of optical clocks". In: *Applied Physics Express* 14.7 (July 2021), p. 072006. DOI: 10.35848/1882-0786/ac0e16. URL: https://doi.org/10.35848/1882-0786/ac0e16.

[10] Juan A. Muniz et al. "Cavity-QED measurements of the ^{87}Sr millihertz optical clock transition and determination of its natural linewidth". In: *Phys. Rev. Res.* 3 (2 May 2021), p. 023152. DOI: 10.1103/PhysRevResearch.3.023152. URL: https://link.aps.org/doi/10.1103/PhysRevResearch.3.023152.

[11] Florian Schreck. *Strontium BEC lecture notes*. Accessed: 2026-06-03. n.d. URL: https://www.strontiumbec.com/.

[12] Sana Boughdachi et al. "Quasicontinuous sub-μK strontium source without a high-finesse cavity-stabilized laser". In: *Phys. Rev. Appl.* 25 (3 Mar. 2026), p. 034053. DOI: 10.1103/3gnx-4s97. URL: https://link.aps.org/doi/10.1103/3gnx-4s97.

[13] M. Gross and S. Haroche. "Superradiance: An essay on the theory of collective spontaneous emission". In: *Physics Reports* 93.5 (1982), pp. 301–396. ISSN: 0370-1573. DOI: https://doi.org/10.1016/0370-1573(82)90102-8. URL: https://www.sciencedirect.com/science/article/pii/0370157382901028.

[14] Camila Beli Silva. "Cavity-atom interactions in a thermal strontium beam: Development of a simple apparatus for quantum metrology". PhD thesis, defended 26 June 2025. PhD thesis. Amsterdam, The Netherlands: Universiteit van Amsterdam, June 2025.

[15] Justin G. Bohnet et al. "A steady-state superradiant laser with less than one intracavity photon". In: *Nature* 484.7392 (2012), pp. 78–81. DOI: 10.1038/nature10920. URL: https://doi.org/10.1038/nature10920.

[16] Swadheen Dubey et al. "Modeling of a continuous superradiant laser on the sub-mHz $^1S_0 \rightarrow {}^3P_0$ transition in neutral strontium-88". In: *Phys. Rev. Res.* 7 (1 Mar. 2025), p. 013292. DOI: 10.1103/PhysRevResearch.7.013292. URL: https://link.aps.org/doi/10.1103/PhysRevResearch.7.013292.

[17] Sheng Zhou. "Towards a continuous active optical clock based on superradiant lasing using strontium". PhD thesis. Amsterdam, The Netherlands: University of Amsterdam, 2024. ISBN: 978-94-6473-609-0.

[18] Renhao Tao et al. *Universal gates for a metastable qubit in strontium-88*. 2025. arXiv: 2506.10714 [quant-ph]. URL: https://arxiv.org/abs/2506.10714.

[19] Sebastian Pucher, Sofus Laguna Kristensen, and Ronen M. Kroeze. *^{88}Sr Reference Data*. 2025. arXiv: 2507.10487 [physics.atom-ph]. URL: https://arxiv.org/abs/2507.10487.

[20] V. Klüsener et al. "Coherent excitation of a micro Hz scale optical magnetic quadrupole transition". In: *Physical Review Letters* 132.25 (2024). ISSN: 1079-7114. DOI: 10.1103/physrevlett.132.253201. URL: http://dx.doi.org/10.1103/PhysRevLett.132.253201.

[21] A. Kramida et al. *NIST Atomic Spectra Database (version 5.12)*. Online. Available: https://physics.nist.gov/asd. [Accessed: 6-Jul-2026]. Gaithersburg, MD, 2024. DOI: 10.18434/T4W30F. URL: https://physics.nist.gov/PhysRefData/ASD/lines_form.html.

[22] D. E. Pritchard et al. "Light Traps Using Spontaneous Forces". In: *Phys. Rev. Lett.* 57 (3 July 1986), pp. 310–313. DOI: 10.1103/PhysRevLett.57.310. URL: https://link.aps.org/doi/10.1103/PhysRevLett.57.310.

[23] Alan L. Migdall et al. "First Observation of Magnetically Trapped Neutral Atoms". In: *Phys. Rev. Lett.* 54 (24 June 1985), pp. 2596–2599. DOI: 10.1103/PhysRevLett.54.2596. URL: https://link.aps.org/doi/10.1103/PhysRevLett.54.2596.

[24] Rudolf Grimm, Matthias Weidemüller, and Yurii B. Ovchinnikov. *Optical dipole traps for neutral atoms*. 1999. arXiv: physics/9902072 [physics.atom-ph]. URL: https://arxiv.org/abs/physics/9902072.

[25] Eugene Hecht. *Optics*. 4th ed. San Francisco, CA: Addison Wesley, 2002.

[26] Amani Kiruga et al. "Portal for High-Precision Atomic Data and Computation". In: *Computer Physics Communications* 319 (2026), p. 109951. ISSN: 0010-4655. DOI: https://doi.org/10.1016/j.cpc.2025.109951. URL: https://www.sciencedirect.com/science/article/pii/S0010465525004527.

[27] Jun Ye and Theresa W. Lynn. "Applications of Optical Cavities in Modern Atomic, Molecular, and Optical Physics". In: *Advances in Atomic, Molecular, and Optical Physics*. Vol. 49. Elsevier, 2003, pp. 1–83. DOI: 10.1016/S1049-250X(03)80003-4. URL: https://doi.org/10.1016/S1049-250X(03)80003-4.

[28] Andrew MacRae. *Week 6b: Fabry Perot Interferometers*. YouTube. Uploaded February 19, 2021. Accessed: 2026-06-29. Feb. 2021. URL: https://www.youtube.com/watch?v=jZfY_13cEzw.

[29] Mark Fox. *Quantum Optics: An Introduction*. Oxford: Oxford University Press, 2006. ISBN: 9780198566724. DOI: 10.1093/oso/9780198566724.001.0001. URL: https://doi.org/10.1093/oso/9780198566724.001.0001.

[30] R. Paschotta. *Hermite–Gaussian Modes*. RP Photonics Encyclopedia. Available online at https://www.rp-photonics.com/hermite_gaussian_modes.html. 2008. DOI: 10.61835/oqg. URL: https://www.rp-photonics.com/hermite_gaussian_modes.html (visited on 06/04/2026).

[31] R. Paschotta. *Resonator Modes*. RP Photonics Encyclopedia. Available online at https://www.rp-photonics.com/resonator_modes.html. 2005. DOI: 10.61835/0qg. URL: https://www.rp-photonics.com/resonator_modes.html (visited on 06/04/2026).

[32] Norman Hodgson and Horst Weber. *Stable Resonators*. London: Springer, 1997, pp. 165–222. ISBN: 978-1-4471-3597-5. DOI: 10.1007/978-1-4471-3595-1_6. URL: https://link.springer.com/chapter/10.1007/978-1-4471-3595-1_6.

[33] A. G. Fox and Tingye Li. "Resonant modes in a maser interferometer". In: *The Bell System Technical Journal* 40.2 (1961), pp. 453–488. DOI: 10.1002/j.1538-7305.1961.tb01625.x.

[34] R. Paschotta. *Ring Resonators*. RP Photonics Encyclopedia. Available online at https://www.rp-photonics.com/ring_resonators.html. 2019. DOI: 10.61835/i1v. URL: https://www.rp-photonics.com/ring_resonators.html (visited on 06/04/2026).

[35] Yu-Ting Chen et al. "High finesse bow-tie cavity for strong atom-photon coupling in Rydberg arrays". In: *Opt. Express* 30.21 (Oct. 2022), pp. 37426–37435. DOI: 10.1364/OE.469644. URL: https://opg.optica.org/oe/abstract.cfm?URI=oe-30-21-37426.

[36] *Glossary*. Part of the reZonator Manual. reZonator Project. 2026. URL: http://rezonator.orion-project.org/help/glossary.html (visited on 06/05/2026).

[37] Markku Mikael Vainio, John Bernard, and Louis Marmet. "Cavity-enhanced optical frequency doubler based on transmission-mode Hänsch–Couillaud locking". In: *Applied Physics B* 104.4 (2011), pp. 897–908. ISSN: 0946-2171. DOI: 10.1007/s00340-011-4437-z.

[38] Hinata Takidera et al. "Adjusting optical cavity birefringence with wavelength tunable laser for axion searches". In: *Physical Review D* 112.6 (2025), p. 063048. DOI: 10.1103/5pw8-zxmc.

[39] Eric D. Black. "An introduction to Pound–Drever–Hall laser frequency stabilization". In: *American Journal of Physics* 69.1 (Jan. 2001), pp. 79–87. DOI: 10.1119/1.1286663. URL: https://doi.org/10.1119/1.1286663.

[40] Lluís de Miguel Blasco. "Towards a new parent laser for strontium experiments". Master's thesis. Amsterdam, Netherlands: University of Amsterdam, Oct. 2024.

[41] Tristam Boer. "New red laser system for strontium experiments". Internship thesis. Amsterdam, Netherlands: University of Amsterdam, June 2025.

[42] Matthew A. Norcia. "New Tools for Precision Measurement and Quantum Science with Narrow Linewidth Optical Transitions". Advisor: James K. Thompson. Ph.D. thesis. Boulder, CO: University of Colorado, 2017.

[43] Zhixin Liu and Radan Slavík. "Optical Injection Locking: From Principle to Applications". In: *Journal of Lightwave Technology* 38.1 (2020), pp. 43–59. DOI: 10.1109/JLT.2019.2945718.

[44] TOPTICA EAGLEYARD. *EYP-RWL-0808-00800-4000-BFW09-0000: 808 nm Single Mode Fabry–Perot Laser Diode*. Datasheet Revision 1.00. 2020. URL: https://www.toptica-eagleyard.com/ey-product/eyp-rwl-0808-00800-4000-bfw09-0000/ (visited on 06/10/2026).

[45] M. Fukuda et al. "Temperature and current coefficients of lasing wavelength in tunable diode laser spectroscopy". In: *Applied Physics B* 100.2 (2010), pp. 377–382. DOI: 10.1007/s00340-009-3878-0.

[46] Luuk Michels. "Building a galvo based fiber switcher for laser frequency measurements with a wavemeter". Bachelor's thesis. Amsterdam, Netherlands: University of Amsterdam, June 2023.

[47] PI (Physik Instrumente) L.P. *Basic Designs of Piezoelectric Positioning Elements: Stacks and Tubes*. PI Piezo Motion Control Tutorial, Tutorial 4-39. PI (Physik Instrumente) L.P., 440 Hartford Turnpike, Shrewsbury, MA 01545, USA. 2026. URL: https://www.pi-usa.us/en/products/piezo-flexure-nanopositioners/piezo-motion-control-tutorial/tutorial-4-39 (visited on 06/16/2026).

[48] Chetvorno. *Animated diagram showing the operation of a tuned circuit (LC circuit)*. Own work, Wikimedia Commons. July 2013. URL: https://commons.wikimedia.org/wiki/File:Tuned_circuit_animation_3.gif.

[49] Edwin Baaij. *AnaPID: Analog PID (Laser) Controller: Versatile Analog PID Controller for (Laser) Optics*. Version 1.02 and 2. Draft manual, 27 January 2025. Technology Centre. Jan. 2025.

[50] National Instruments. *The PID Controller & Theory Explained*. https://www.ni.com/en/shop/labview/pid-theory-explained.html. Updated March 7, 2025. Accessed June 19, 2026. 2006.

[51] Adam L. Shaw et al. "A cavity-array microscope for parallel single-atom interfacing". In: *Nature* 650 (2026), pp. 320–326. DOI: 10.1038/s41586-025-10035-9.

[52] Konstantin Herb. *Bloch Sphere Visualizer*. https://bloch.kherb.io/. ETH Zurich. MIT license. Accessed: 2026-06-29. 2023. URL: https://bloch.kherb.io/.

[53] Shayne Peter Bennetts. "1000 times closer to a continuous atom laser: Steady-state strontium with unity phase-space density". Promotor: prof. dr. F. E. Schreck; Co-promotor: dr. B. B. Pasquiou. Research carried out at the Van der Waals-Zeeman Institute, Institute of Physics, University of Amsterdam. PhD thesis. Amsterdam, The Netherlands: Universiteit van Amsterdam, Oct. 2019. ISBN: 978-94-028-1748-5.